ROBUST, MULTI-CONSTELLATION, MULTI-FREQUENCY PRECISE POINT POSITIONING FOR INSTANTANEOUS, CM-LEVEL POSITIONING

BENJAMIN ADU

A THESIS SUBMITTED TO THE FACULTY OF GRADUATE STUDIES

IN PARTIAL FULFILLMENT OF THE REQUIREMENTS

FOR THE DEGREE OF MASTER OF SCIENCE

GRADUATE PROGRAM IN EARTH AND SPACE SCIENCE

YORK UNIVERSITY

TORONTO, ONTARIO

March 2025

Abstract

Achieving instantaneous centimetre-level 3D accuracy for Global Navigation Satellite System (GNSS) multi-constellation, multi-frequency Precise Point Positioning (PPP) with ambiguity resolution without local augmentation poses significant challenges due to multipath, atmospheric refraction, and hardware noise. This research reduces York-PPP engine limitations by separating the BeiDou-2 and BeiDou-3 GNSS constellations clock terms in the design matrix and expanding the uncombined Decoupled Clock Model from triple to quadruple frequency measurements for BeiDou-3 constellation. Processing of geodetic measurements show overall horizontal positioning errors reduced by 77% (from 20.8 cm to 4.7 cm) and 88% (from 22.8 cm to 2.8 cm) for float and fixed solutions, respectively. Furthermore, this research investigates outliers in epoch-by-epoch PPP solutions, delving into potential causes such as signal-to-noise ratio (SNR), pseudorange multipath and noise etc. Additionally, principal component analysis with Hotelling's T-squared method is employed to detect major outlier sources. Results indicate that satellite elevation angle, signal strength, and the code-minus-carrier observable, which includes ionospheric refraction and pseudorange multipath, significantly impact positioning solution.

Acknowledgements

First and foremost, I would like to thank God for His grace from the beginning to the end of this thesis.

I would like to express my sincere appreciation to my supervisor, Professor Sunil Bisnath, for his invaluable guidance, mentorship, and continuous support throughout my research. His expertise and encouragement have been instrumental in shaping this work.

I am also grateful to Professor Jianguo Wang for serving as a member of my research committee. His insightful feedback and constructive suggestions have significantly contributed to the progress of this research.

My heartfelt thanks go to Professor Regina Lee and Professor Mojgan Jadidi for taking the time to serve on my examination committee. Their willingness to review my work and provide valuable input is deeply appreciated.

A special note of gratitude to Dr. John Aggrey, whose guidance and encouragement have been a constant source of motivation since I embarked on my graduate studies. His advice and support have played a crucial role in my academic journey.

I am also deeply thankful to my past and present GNSS lab colleagues for their unwavering support and camaraderie throughout my master's journey. I truly appreciate the discussions, collaborations, and encouragement from Nacer, Anurag, Ding, Jiahuan, Sihan, Soroush, Pragati, Sandesh, Caitlyn and others, who have made this experience enriching and memorable.

Finally, I extend my gratitude to my family, most especially to my parents, Mr. Samuel Adu and Mrs. Gladys Adu Quansah, and my uncle, Mr. Frank Quansah for their unconditional support, patience, and encouragement. Their belief in me has been a constant source of inspiration.

Table of Contents

List of Tables

List of Figures

List of Acronyms

ANTEX	ANTenna EXchange
APC	Antenna Phase Centre
AR	Ambiguity Resolution
ARP	Antenna Reference Point
$\mathbf{C/N_0}$	Carrier-to-Noise Density Ratio
CDF	Cumulative Density Function
CDMA	Code Division Multiple Access
CMC	Code Minus Carrier
CMEs	Common Mode Errors
CNES	centre national d'etudes spatiales
DCM	Decoupled Clock Model
DOP	Dilution of Precision
DOY	Day of Year
EGNOS	European Geostationary Navigation Overlay Service
FAA	Federal Aviation Administration
FCB	Fractional Cycle Bias
FDMA	Frequency Division Multiple Access

GEO	Geostationary Earth Orbit
GFZ	GeoForschungsZentrum
GMF	Global Mapping Function
GLONASS	GLObalnaya NAvigatsionnaya Sputnikovaya Sistema
GNSS	Global Navigation Satellite System
GPS	Global Positioning System
IERS	International Earth Rotation and Reference Systems Service
IGS	International GNSS Service
IGSO	Inclined Geo-Synchronous Orbit
IRC	Integer Recovery Clock
LAMBDA	Least-squares AMBiguity Decorrelation Adjustment
MCMF	Multi-Constellation Multi-Frequency
MEO	Medium Earth Orbit
MLAMBDA	Modified Least-squares AMBiguity Decorrelation Adjustment
MW	Melbourne - Wübbena
NL	Narrow Lane
NRTK	Network RTK
PC	Principal Component

PCA	Principal Component Analysis
PDOP	Position Dilution of Precision
PPP	Precise Point Positioning
PPS	Precise Positioning Service
QZSS	Quazi-Zenith Satellite System
RMS	Root Mean Square
RMSE	Root Mean Square Error
RTK	Real-Time Kinematic
SA	Selective Availability
SNR	Signal-to-Noise Ratio
SPP	Single Point Positioning
SPS	Standard Positioning Service
VBPCA	Variational Bayesian PCA
WAAS	Wide Area Augmentation System
WL	Wide Lane

1 Introduction

Global Navigation Satellite Systems (GNSSs) have redefined measurement and navigation by offering unprecedented accuracy and reliability in positioning. Today, a wide range of GNSS constellations - such as GPS, GLONASS, Galileo, and BeiDou - are providing multi-frequency signals that have enabled more robust and precise positioning (Hofmann-Wellenhof et al., 2008). One of the most promising approaches to exploit these signals is Precise Point Positioning (PPP), which allows for centimetre level accuracy from a single receiver on global scale without any necessity for local base stations (Zumberge et al., 1997). PPP makes use of precise satellite orbit and clock corrections (Kouba & Héroux, 2001), in conjunction with multi-frequency GNSS observations to reduce errors and resolve ambiguities in positioning solutions.

While PPP achieves satisfactory performance, it requires long convergence times to resolve ambiguities and attain high accuracy. This long convergence time seriously limits its suitability for applications requiring instantaneous or near-instantaneous results. Recent developments in GNSS technology, especially for multi-constellation and multi-frequency data (Montenbruck et al., 2017), have paved the way toward performance improvements that will make faster convergences and more accurate solutions possible through PPP. Laurichesse and Banville (2018) used dual-frequency GPS and four-frequency Galileo to achieve instantaneous centimetre-level PPP solution using global corrections. They concluded that the combination of multiple constellations aids in strengthening the geometry, and the use of multiple frequencies allows for improved ambiguity resolution performance. The result is limited to an hour data from one IGS. With the addition of other constellations broadcasting at multiple carrier frequencies, this thesis is focused on processing a week worth of data from selected IGS stations globally.

In an attempt to eliminate initial position solution's convergence time, (Geng et al., 2019) focused on achieving decimetre-level positioning rather than centimetre-level. Gao et al. (2021) developed the use of multi-system, multi-frequency uncombined PPP single-epoch to achieve instantaneous centimetre-level positioning, but with the inclusion of regional atmospheric corrections, which is not the focus of this thesis because the aim is to make PPP function globally without any local reference. Additionally, improvements have been made through ambiguity resolution (AR) methods, which fix the carrier-phase ambiguities to their integer values, thus improving the precision of PPP solutions (Collins et al., 2008; Ge et al., 2008; Laurichesse et al., 2009).

Despite these advancements with the focus on achieving an instantaneous centimetre-level positioning without the use of any local infrastructure, significant challenges remain. Measurement errors, particularly from multipath effects, noise, and atmospheric disturbances, introduce outliers and other problems that result in compromised reliability of PPP solutions. Thus, this thesis seeks to address these challenges by emphasizing the understanding, investigation, and detection of outlier sources within a robust multi-frequency, multi-GNSS PPP framework that will also ensure consistent, instantaneous centimeter-level positioning that is independent of local information or augmentation.

1.1 Problem Statement

Achieving instantaneous, centimetre-level accuracy for multi-constellation, multi-frequency (MCMF) Precise Point Positioning with ambiguity resolution remains a complicated challenge that depends on a set of critical factors. Measurement errors which occur, e.g., pseudorange multipath and noise undermine the precision of GNSS measurements. According to Chengyan et al. (2014), multipath occurs when signals reflect off surfaces before reaching the GNSS receiver. This phenomenon results in the direct signal being received along with reflected ones. Consequently, these reflected signals introduce errors in both pseudorange and carrier phase measurements. Pseudorange multipath can seriously affect positioning accuracy, introducing metre-level error. Iliev et al. (2020) further emphasizes this problem and recognize multipath propagation in low-cost equipment to be one of the most significant error sources in high-precision navigation applications. Their study identifies that the random nature of multipath has the potential to generate significant inconsistencies in GNSS measurements, making it difficult to achieve a reliable positioning solution.

In addition to multipath effects, other errors include atmospheric refraction, which also introduce one of the most formidable challenges to the effective error correction. Refraction from the Earth's atmosphere changes the propagation speed and direction of the GNSS signals, causing inaccuracies in positioning that may persist even after conventional methods of correction are applied. Kos et al. (2009) addressed this issue, where atmospheric effects on GNSS signals cause errors to the overall accuracy of position determination. The errors brought about by ionospheric conditions are quite variable; for example, solar activity can occasionally cause changes to atmospheric conditions that further complicate things in conducting real-time corrections. Equally problematic are tropospheric delays, wherein atmospheric conditions of temperature, relative humidity, and pressure affect signal speed, necessitating advanced modeling for proper compensation.

These errors introduce positioning outliers, further complicating methods of achieving consistent, reliable real-time centimeter-level positioning. The presence of outliers affects not only the overall precision, but also lengthens convergence time to reach the required precision. Understanding and mitigating the impact of these errors is paramount in continuing research to explore methods to improve PPP-AR.

1.2 Thesis Statement and Specific Objectives

The aim of this thesis is to achieve a robust, multi-frequency, multi-GNSS PPP-AR solution, that produces more consistent, instantaneous centimetre-level positioning without the need for local augmentation.

Specifically, this thesis aims to:

- Understand and investigate the causes of positioning outliers in a multi-constellation, multi-frequency PPP-AR epoch-by-epoch processing solution
- Develop techniques for detecting causes of positioning outliers to ensure reliable centimetre-level accuracy in real-time
- Lay the groundwork for future work focused on mitigating outliers to enhance the overall PPP solution performance

In addressing the multifaceted nature of these challenges, performance enhancements of the PPP-AR system are achieved and bring processing a step closer consistent instantaneous, centimetre-level accuracies in practical applications.

1.3 Novelty and Significance

The novelty of this thesis is focused on understanding, investigating, and detecting the causes of outliers in multi-constellation, multi-frequency PPP solutions that enable instantaneous positioning at a centimetre level accuracy without the use of local reference stations. This research will push the limits of PPP-AR performance by integrating advanced techniques to achieve a global infrastructure-independent solution.

Improving positioning performance as affected by multipath, noise, and atmospheric refraction has a far-reaching significance, offering benefits to a wide range of stakeholders whose applications benefit from precise positioning in real time. Examples include geodesy and surveying, where the reduced dependence on local infrastructure serves to make high-precision GNSS-based surveys more flexible in remote or hostile environments. Moreover, autonomous navigation applications, such as drones or autonomous vehicles, will benefit from global high-accuracy positioning without the need for local corrections. Finally, accurate and real-time GNSS solutions have the potential to provide considerable support for environmental monitoring, observing a wide range of natural hazards, climate change, and other global phenomena, without the constraints of requiring local augmentation systems.

1.4 Thesis Outline

Chapter 2 provides a comprehensive review of GNSS positioning and sources of errors. These GNSS positioning techniques include relative positioning (differential GNSS and RTK (Real-Time kinematic/ NRTK (Network RTK)) and Precise Point Positioning. This thesis primarily focuses on PPP, detailing its observation equations and common combinations the technique relies on. Additionally, causes and mitigation of measurement error sources, which include satellite orbit errors, satellite clock errors, atmospheric errors, etc., are reviewed. Ambiguity Resolution is discussed, with decoupled clock model (DCM) and Least-squares AMBiguity Decorrelation Adjustment (LAMBDA) explained. The chapter ends with an analysis of the effects of AR and multiple constellations and multiple frequencies on PPP solutions.

Chapter 3 focuses on improvements to previous work, and commences with a review of the previous work, its advancements and methodologies adopted. This overview to previous work is followed by a detailed description of the limitations and improvements made, including the separation of the BDS-2 and BDS-3 clock terms in the design matrix, and the expansion of the quadruple frequency DCM model for BDS-3. The chapter concludes with a comparison of results from the current and previous works.

Chapter 4 constitutes the most significant novelty of the thesis. It begins by addressing the outliers in a multi-constellation, multi-frequency (MCMF) PPP-AR solution. A new set of datasets are processed in an epoch-by-epoch manner to avoid filtering of the errors that potentially causes outliers as the epoch increases. The analysis of station performance in epoch-by-epoch processing is presented and later an investigation of the station-by-station variations is performed. This analysis is to assess the outliers that occurred in three stations selected based on a good, average and bad performing stations. Finally, the determination of the causes of outliers which include SNR, pseudorange multipath and noise, satellite visibility and geometry, and number of measurements and measurement redundancy are described to set the tone for results and analysis in chapter 5.

Chapter 5 starts with correlation analysis that determines how different potential error sources described in chapter 4 contribute to outliers in the PPP solution. A combined correlation analysis of the errors on the positioning performance is done to examine how interactions between the potential error source interact to cause outliers. Due to an unclear conclusion from the correlation analysis, the principal component analysis (PCA) technique with Hotelling's t-squared method is employed with the aim of identifying which data quality metrics are most significant in causing the outliers.

Finally, Chapter 6 concludes the thesis by summarizing the key contributions from the earlier chapters and suggests recommendations for future research.

2 GNSS Positioning Techniques and Sources of Errors

Global Navigation Satellite Systems (GNSSs) have become the essential foundation of modern positioning, navigation, and timing (PNT) services, providing precise location tracking across a wide range of applications. As the need for accurate and reliable positioning increases, it is essential to understand the various GNSS positioning techniques and the errors that impact their effectiveness. This chapter provides a comprehensive review of the fundamental concepts behind GNSS positioning techniques and the various sources of errors that impact their performance in diverse environments.

2.1 GNSS Concepts and PPP

Satellite navigation originated from the development of the Global Positioning System (GPS) by the United States Department of Defense in the early 1970s (Parkinson & Spilker, 1996). It was initially intended solely for military before civilians were allowed to use it to track their locations with an accuracy level of up to tens of metres. By the mid-1980s, GPS became operational with 24 satellites arranged in 6 orbital planes of 4 satellites per plane, becoming the pioneer of GNSS (Kaplan & Hegarty, 2006). Following this successful implementation, other nations initiated their own satellite navigation systems. The Russian Federation developed "GLObalnaya NAvigatsionnaya Sputnikovaya Sistema" (GLONASS) , which became fully operational in 1993 (Revnivykh et al., 2017). Similarly, the European Union launched Galileo, with its first satellite deployed in 2005, and becoming fully operational in 2016. China also developed the BeiDou

Navigation Satellite System (BDS), which started regional operations in 2000 with BDS-2 and attained global coverage with BDS-3 in 2020. These developments from other countries signify a shift away from relying solely on GPS towards a more robust and diverse GNSS. The compatibility of these systems improves accuracy and reliability, establishing the indispensability of GNSS in many applications from civilian navigation to scientific research and defense operations (Kaplan & Hegarty, 2006).

GNSSs (GPS, GLONASS, Galileo and BeiDou) operate by using network of satellites that transmit signals to receivers on the Earth. At least four GNSS signals are required to estimate the receiver position (Enge, 1994). Each satellite broadcasts the time the signal was transmitted to the receiver on earth and ephemeris to determine the satellite position. The receiver then determines the time the signal arrives at the receiver from each satellite and independently for each satellite. This estimated travel time is used to roughly estimate the distance between each satellite and the receiver called the pseudorange. With the pseudoranges measured, the principle of trilateration is applied to estimate position (latitude, longitude and altitude) and time on Earth (Misra & Enge, 2011).

GNSS positioning techniques can be broadly categorized into point positioning and relative positioning. Point positioning, such as the Standard Positioning Service (SPS) in GPS, is available globally for civilian users at no cost, typically providing metre-level accuracy (Enge, 1994; Parkinson & Spilker, 1996). Relative positioning, which includes techniques like Differential GNSS (DGNSS), Real-Time Kinematic (RTK), and Network RTK (NRTK), enhances accuracy to the sub-meter or centimeter level by using measurements from multiple receivers. Unlike GPS, which specifically offers Standard Positioning Service (SPS) and the Precise Positioning Service (PPS), the latter being restricted to military and authorized government users (Kaplan & Hegarty, 2006), GNSS as a whole supports a wider range of positioning methods. Among these positioning techniques is PPP, the focus of this thesis, which enables high-accuracy global positioning without the need for a reference station network. The choice of a GNSS positioning technique depends on accuracy requirements, application needs, and available infrastructure.

2.1.1 Relative Positioning

Relative positioning is a technique used to determine the precise location of a point with respect to another point. That is, corrections are sent from a nearby reference station to enhance user measurements, improving the accuracy of the position estimates. Relative positioning has transformed from using GPS-only to multi-GNSS and from a single-baseline technique to wide area augmentation (Bisnath, 2020). This usage of multi-constellation has increased the number of satellites available to the user and has improved overall performance. Forms of relative positioning include Differential GNSS (DGNSS), Real-Time Kinematic (RTK), and Network RTK (NRTK) all of which are discussed in the following subsections.

2.1.1.1 Differential GNSS

The concept of DGNSS was first explored in the 1980s, following the deployment of the Global Positioning System (GPS) by the U.S. Department of Defense. While GPS provided global coverage and accurate positioning, its accuracy was initially limited to approximately 10-15 metres for civilian users due to the intentional degradation of signals through Selective Availability (SA) (Parkinson & Spilker, 1996). This level of accuracy was insufficient for many civilian applications, where more precise positioning was required. To address this limitation, differential GPS (DGPS) was devised to eliminate this intentional degradation through between-receiver differencing that eliminates most spatially-correlated error sources (Kremer et al., 1990). The idea was to use a stationary reference receiver at a known location to calculate the errors in the GPS signals. These errors, which included ionospheric and tropospheric delays, satellite clock errors, and ephemeris errors, could then be transmitted to a rover receiver of unknown position, allowing it to apply corrections in real time. This differential correction significantly improved the positioning accuracy, reducing the error to within a few metres, and in some cases, even centimetres (Gao et al., 1997; Hofmann-Wellenhof et al., 2008; Misra & Enge, 2006; Parkinson & Spilker, 1996).

DGNSS can be implemented in various forms, including local area DGNSS (LADGNSS) and wide area DGNSS (WADGNSS). LADGNSS typically uses a single reference station or a small network of stations to provide corrections within a limited geographic area. The first practical implementations of LADGNSS were developed for marine navigation. These early systems used marine radio beacons to transmit differential corrections to vessels, greatly enhancing the safety and efficiency of marine operations (Leick et al., 2015). With the growing adoption of GPS in civilian sectors, DGNSS became more widespread. During this period, the U.S. Coast Guard established a network of DGNSS reference stations along the U.S. coastline, providing free differential corrections to improve the accuracy of GPS for maritime users (Hofmann-Wellenhof et al., 2008). On the other hand, WADGNSSs, such as the Wide Area Augmentation System (WAAS) in North America or the European Geostationary Navigation Overlay Service (EGNOS), use a network of reference stations spread over a wide area. These systems provide corrections for large regions and are especially useful in aviation and other applications that require reliable positioning over extensive areas (Parkinson & Spilker, 1996). In 1993, the advent of the WAAS by the Federal Aviation Administration (FAA) marked a significant advancement in DGNSS. WAAS provided differential corrections over a wide area, covering the continental United States, and was primarily aimed at improving the safety of aircraft navigation (Kaplan & Hegarty, 2006). The discontinuation of Selective Availability (SA) by the U.S. government in May 2000 greatly improved the baseline accuracy of GPS for civilian users, reducing the need for DGNSS in some applications. However, DGNSS continued to be vital for applications requiring centimeter-level accuracy (Teunissen & Montenbruck, 2017).

The accuracy of DGNSS depends on several factors, including the distance between the reference station and the rover receiver, the quality of the corrections, and the GNSS signals used. With the type of measurements used in differential positioning, DGNSS uses pseudorange measurements only on both the user and correction sides. This technique provides decimetre-level accuracy, because of the noisy nature of the pseudorange measurements. Alternatively, there is an approach which uses carrier-phase measurements to smooth the pseudorange measurements to enhance the accuracy levels. Alternatively, the pseudorange measurements are used in conjunction with the carrier-phase measurements to achieve a centimetre-level of accuracy. This approach relates to how RTK and NRTK work and is further discussed in the next subsection.

The introduction of DGNSS revolutionized GNSS-based positioning by providing a practical method of achieving high accuracy without requiring significant changes to the existing GPS infrastructure. As time went by, DGNSS techniques evolved to include network-based solutions, such as NRTK which would be detailed in the next subsection.

2.1.1.2 Real-Time Kinematic and Network RTK

RTK technology was developed in the late 1980s and early 1990s as an extension of the DGNSS concept. While DGNSS provided meter-level accuracy, there was an increasing demand for even more precise positioning for various applications such as land surveying, construction, etc. As such, RTK was designed to address this need by offering real-time, centimetre-level accuracy. The core idea behind RTK is to utilize the carrier-phase measurements of GNSS signals, rather than just the pseudorange measurements only which is used by the DGNSS technique, to determine the position of the user. Carrier-phase measurements are much more precise than pseudorange measurements, but they require resolving the so-called integer ambiguity, which is the unknown number of full wavelengths between the satellite and the receiver (Teunissen & Montenbruck, 2017). In an RTK system, a base station with a known position continuously monitors GNSS signals and calculates carrier-phase ambiguities. These ambiguities, along with the precise position of the base station, are transmitted as corrections to a rover receiver in the field. Transmitting the ambiguities of the reference receiver is essential to the rover to resolve its own ambiguities quickly and accurately. Then, rover uses this information to correct its own measurements and generates its position with centimetre-level accuracy in real time (Leick et al., 2015).

While traditional RTK provides high accuracy, it has certain limitations, especially regarding the distance between the base station and the rover receiver. The performance of RTK reduces as the distance increases because errors, such as those caused by atmospheric conditions, become less correlated as distance increases. To address these limitations, Network RTK was developed, by utilizing network of stations rather than a single base station (Jensen & Cannon, 2000; Townsend et al., 1999). These networks of base stations are connected to a central server, which processes the data and generates correction information that accounts for spatially varying errors across the network (Gao & Shen, 2002). These corrections, which include satellite orbits, clocks, hardware biases, atmospheric errors (interpolated ionospheric and tropospheric corrections), are broadcast to the user, allowing it to achieve high and better accuracy over a much larger area than in the case of a single base station (Rizos, 2002).

Both RTK and Network RTK have significantly influenced the decision of industries to require high-precision GNSS positioning. RTK is commonly used in land surveying, where centimetre-level accuracy is essential for mapping and construction projects. Network RTK on the other hand, with its capability to provide precise positioning over large areas, has applications in precision agriculture, enabling accurate guidance of farm machinery, and in autonomous systems, such as drones and self-driving cars, where reliable and accurate positioning is critical (Misra & Enge, 2006). The development of Network RTK has also facilitated the establishment of commercial RTK networks managed by government agencies, private companies, and regional organizations. These networks offer real-time correction services to users across extensive geographic areas, eliminating the need for users to set up their own base stations (Hofmann-Wellenhof et al., 2008).

2.1.2 Precise Point Positioning

Precise Point Positioning (PPP) enables users to achieve highly accurate positioning using a single receiver, without the use for a nearby reference station. The concept of PPP began to take shape in the late 1990s, following significant advancements in GNSS technology and the availability of precise satellite orbit and clock information. Before PPP, precise GNSS positioning was mainly achieved through differential techniques that required a network of ground-based reference stations. While effective, these methods have limitations, especially in remote or global-scale applications, where deploying such networks is impractical (Zumberge et al., 1997). The key breakthrough that enabled the development of PPP was the availability of precise satellite orbit and clock corrections. These corrections, generated by organizations like the International GNSS Service (IGS), accounts for various errors affecting GNSS signals, such as satellite orbit inaccuracies, satellite clock biases, and atmospheric refraction. By applying these corrections, a single GNSS receiver could achieve centimetre-level accuracy, eliminating the need for a nearby reference station (Kouba & Héroux, 2001).

There are numerous advantages of transitioning to PPP, one of which being the reduction in computation burden and bandwidth requirements to transmit corrections to user. PPP reduces the computational load on the infrastructure by depending on globally generated, less frequently updated satellite corrections and doing a majority of the processing at the user's end (i.e., GNSS receiver), contrast to RTK which frequently calculates and transmits real-time corrections in the form of satellite and atmospheric corrections and requires significant resources most especially in areas with a network of multiple reference stations. In terms of bandwidth requirements, RTK requires a continuous and high bandwidth communication link to transmit real-time corrections that are generated continuously to ensure precise and high accuracy over short distances. PPP on the other hand, reduces bandwidth requirement by using infrequent global satellite corrections which are produced in every few minutes or even longer, making transmission of data more efficient and ideal for remote areas where communication bandwidth is limited. Overall, this reduced computational and bandwidth requirements of PPP makes it highly scalable, cost-efficient and flexible; thereby supporting numerous users simultaneously while providing robust and high-precision positioning globally.

PPP is considered a single point positioning (SPP) technique as it directly uses only a single receiver in its operation. It is seen as an upgrade of the traditional SPP which allows for decimetre to centimetre-level positioning. It can achieve this accuracy through four avenues which are: i) the use of precise products such as satellite orbit, clock and bias corrections, ii) the use of carrier-phase measurements in addition to the pseudorange measurements, iii) additional error modeling to mitigate error sources and iv) use of sequential filtering techniques (such as sequential least squares or Kalman filtering), which use previous epoch information to improve the results of the current epoch. The combination of these avenues allows a PPP solution to converge within minutes or tens of minutes thereby achieving precision and high accuracy.

2.1.2.1 Observation Equations

In GNSS, the primary measurements used are the pseudorange and carrier-phase measurements. For a given satellite, s, and a receiver, r, on frequency, n, where n is a set of {1, 2, …, N}, the pseudorange and carrier-phase observation equations can be expressed as follows:

$$\begin{cases} P_{r,n}^{s} = \rho_r^s + c(dt_r - dt^s) + \gamma_n I_1^s + M_r^s . T_r + \left(b_{r,n} - b_n^s\right) + \epsilon_{P,n} \\ \Phi_{r,n}^{s} = \rho_r^s + c(dt_r - dt^s) - \gamma_n I_1^s + M_r^s . T_r + \lambda_n\left(N_n^s + B_{r,n} - B_n^s\right) + \epsilon_{\Phi,\mathrm{n}} \end{cases} \tag{2.1}$$

where $P_{r,n}^{s}$ and $\Phi_{r,n}^{s}$ are the pseudorange and carrier-phase measurements respectively expressed in metres, ρ_r^s is the geometric distance between the satellite and receiver, c is the speed of light in a vacuum, dt_r and dt^s are the receiver clock offset and satellite clock offset from GPS time, respectively, $\gamma_n = \frac{f_1^2}{f_n^2}$ is the ionospheric delay which is the ratio of frequencies that is applied to the first frequency ionospheric delay I_1^s to calculate the ionospheric delay at frequency n, M_r^s is the mapping function used to map the zenith troposphere wet delay T_r to the satellite-receiver line of sight tropospheric delay, $\lambda_n = \frac{c}{f_n}$ is the signal's wavelength corresponding to frequency f_n, N_n^s is the integer ambiguity (number of full wavelengths) on frequency f_n, $b_{r,n}$ and b_n^s are the receiver and satellite hardware code biases, respectively, $B_{r,n}$ and B_n^s are receiver and satellite hardware phase biases, respectively, and ϵ_P^n and ϵ_Φ^n are any remaining unmodelled residual mostly in the form of multipath and noise for the pseudorange and carrier-phase measurements, respectively. One thing that differentiates the carrier-phase equation from the pseudorange equation is the negative sign of the ionospheric delay term and the presence of the integer ambiguity term in the carrier phase equation.

All parameters in Equation (2.1) cannot be simultaneously estimated directly due to a rank deficiency of the system, as not all states are directly observable. Therefore, it is necessary to re-parameterize the equations by incorporating the receiver and satellite biases into other parameters to limit the number of estimated parameters.

2.1.2.2 Common combinations

To minimize errors and improve accuracy in a solution, PPP often uses linear combinations of the pseudorange and carrier-phase measurements at different frequencies. Below are the most common combinations used in GNSS.

Ionosphere-Free Combination

Traditional PPP has been using ionosphere-free combination which was formulated to eliminate the first-order ionosphere delay term, which is considered as the major source of error in GNSS measurements. This combination functions by combining observations from two different frequencies. Considering frequencies f_1 and f_2, the ionosphere-free combination is expressed as:

$$\begin{cases} P_{IF,r}^{s} = \frac{f_1^2 . P_{r,1}^{s} - f_2^2 . P_{r,2}^{s}}{f_1^2 - f_2^2} \\ \Phi_{IF,r}^{s} = \frac{f_1^2 . \Phi_{r,1}^{s} - f_2^2 . \Phi_{r,2}^{s}}{f_1^2 - f_2^2} \end{cases} \tag{2.2}$$

where $P_{IF,r}^{s}$ and $\Phi_{IF,r}^{s}$ are the ionosphere-free pseudorange and carrier-phase combinations respectively, f_1 and f_2 are the first and second frequencies of the two signals. Noting equations (2.1) and (2.2), it could be derived that the combination would effectively eliminate the ionosphere state term by cancelling out the ionosphere state term from the equation. In a classic PPP model, other parameters such as ambiguities are absorbed and helps to simplify the estimation model

(Kouba & Héroux, 2001). State terms that have a line on top on them in (2.3) denotes that they are being absorbed into other quantities. The simplified equation for an ionospheric combination in the dual frequency case is:

$$\begin{cases} P_{IF,r}^{s} = \rho_r^s + c\left(\overline{dt_r} - dt^s\right) + M_r^s.T_r + \epsilon_P^n \\ \Phi_{IF,r}^{s} = \rho_r^s + c\left(\overline{dt_r} - dt^s\right) + M_r^s.T_r + \lambda_n \overline{N_n^s} + \epsilon_\Phi^n \end{cases} \tag{2.3}$$

Geometry-free Combination

In this type of combination, the geometric part of the measurement is cancelled out leaving the ionospheric delay, phase wind up and instrumental delays which are considered the frequency-dependent effects, multipath and measurement noise. This combination helps to detect cycle-slips in the carrier-phase measurements and estimate the ionospheric total electron content (TEC). In detecting of cycle slips, Blewitt (1990) employed the geometry-free combination to detect and correct cycle slips in GPS carrier-phase data. The geometry-free combination has also been used significantly in several GNSS studies to estimate the ionospheric TEC. Mannucci et al. (1993) employed the geometry-free combination to estimate TEC from GPS data. This method became the fundamental of ionospheric studies. Ciraolo et al. (2007) and Sardón et al. (1994) used the geometry-free combination to derive the TEC from dual frequency GPS measurements. For two frequencies f_1 and f_2, the geometry-free combination can be expressed as:

$$\Phi_{GF} = \Phi_{f1} - \Phi_{f2} \tag{2.4}$$

where Φ_{GF} is the geometry-free combination, and Φ_{f1} and Φ_{f2} are the carrier-phase measurements for the first and second frequencies used.

Wide-lane, Narrow-lane and Melbourne- Wübbena Combinations

The wide-lane (WL) combination is used to form measurements with longer wavelengths. This longer wavelength is essential for cycle-slip detection and ambiguity fixing. Narrow-lane (NL) combination is used to create measurements with shorter wavelengths. The combination formed from NL has a relatively lower noise than the each of the separated measurements used. The Melbourne-Wübbena (MW) combination is used to estimate wide-lane ambiguity directly. MW combination provides two benefits. The first benefit is the wide-lane ambiguity formed has a wider wavelength than the two separated measurements used, which leads to enlarging of the ambiguity spacing. On the second benefit, the narrow-lane combination of the pseudorange measurements helps to reduce the measurement noise. MW is used to resolve ambiguities critical for high-precision positioning. For pseudorange and carrier-phase measurements on frequencies f_1 and f_2, WL, NL and MW combinations can be expressed as:

$$\begin{cases} P_{NL,r}^{s} = \frac{f_1.P_{r,1} + f_2.P_{r,2}}{f_1 + f_2} \\ \Phi_{NL,r}^{s} = \frac{f_1.\Phi_{r,1} + f_2.\Phi_{r,2}}{f_1 + f_2} \\ P_{WL,r}^{s} = \frac{f_1.P_{r,1} - f_2.P_{r,2}}{f_1 - f_2} \\ \Phi_{WL,r}^{s} = \frac{f_1.\Phi_{r,1} - f_2.\Phi_{r,2}}{f_1 - f_2} \\ \mathrm{MW}_{r}^{s} = \Phi_{WL,r}^{s} - P_{NL,r}^{s} \end{cases} \tag{2.5}$$

where $P_{NL,r}^{s}$ and $\Phi_{NL,r}^{s}$ are the NL combinations for the pseudorange and carrier-phase measurements, respectively, $P_{WL,r}^{s}$ and $\Phi_{WL,r}^{s}$ are the WL combinations for the pseudorange and carrier-phase measurements respectively, and MW_{r}^{s} is the Melbourne-Wübbena combination.

2.2 Measurement Error Sources

For PPP processing, there are several corrections that need to be accounted for. Some of these corrections are common to all positioning techniques but are treated differently for each approach. Other corrections, including satellite antenna corrections are as important other techniques, but they are crucial in PPP. Certain errors in PPP can be mathematically represented as they occur from modellable sources while others need to be empirically estimated, either manually by the user or automatically from network provider before disseminated to the users. The following provides the most important sources of error and methods to mitigate them.

2.2.1 Satellite Orbit Errors

Satellite orbit errors refer to inaccuracies in the positions of GNSS satellites. The errors originate from several factors, including gravitational forces of Earth and other celestial bodies (the Moon and Sun), solar radiation pressure, as well as imperfections in operation of satellite propulsion system. As the satellite determines its position by ground stations, small orbital errors can result in noticeable positional inaccuracies in single positioning techniques. User calculates satellite position using broadcast ephemeris in SPP. The broadcast ephemeris is usually accurate to within metres; however this satellite position calculated from the broadcast file may not provide the required level of accuracy for high-precision applications such as RTK or NRTK. In these applications, between-receiver differencing can effectively cancel common aspects of residual satellite orbit errors. If only a single receiver is used, as in PPP, no between-receiver differencing can be performed. Therefore, broadcast satellite orbits are inaccurate for good PPP results. Instead, precise satellite orbits are required. The precise orbits are much more accurate, approaching 1-2 cm in precision using a global network of stations with known positions. It is possible to obtain much higher accuracy in this estimation by simultaneously reducing the observation data of all these stations and treating the satellite orbits as unknowns. These precise satellite orbits are typically accurate to a few centimetres, which can be broadcasted in real-time as corrections along with the satellites broadcast orbits (Wabbena et al., 2005) or provided in Receiver INdependent EXchange (RINEX) format files.

2.2.2 Satellite Clock Errors

Satellite clock errors represent a significant source of inaccuracy within GNSS-based positioning. After all, these errors are manifested by defects and drifts in the onboard atomic clocks of the satellites. Even the slightest deviation will have a significant effect on the computed position as 1 nanosecond in timing error corresponds to approximately 30 cm of distance. The correction parameters are broadcast in the GNSS navigation messages and commonly used to mitigate satellite clock errors for SPP. These parameters are clock bias, drift and rate to eliminate the satellite clock errors to around a few nanoseconds. This, however, may not be enough correction for high-precision RTK or NRTK applications that require centimeter-level accuracy due to receiver differencing which cancels out these errors. In the case of PPP, satellite clock errors are generally more important because no between-receiver differences exist to cancel these errors. Consequently, precise satellite clock corrections are required. These corrections are available from the International GNSS Service (IGS), in real-time or post-processed products. The precise clock corrections from IGS can rather limit residual errors to the order of few centimetres (Dow et al., 2009).

2.2.3 Relativistic Effects

The relativistic effects in GNSS come with the basic one of Einstein's theory of relativity that has become relatively important due to speeds at which satellites are moving and have less gravitational potential as compared for a receiver on Earth. The two primary relativity effects on GNSS positioning are time dilation and the gravitational frequency shift. For time dilation, time passes at different rates for observers in different frames of reference and that this effect is also experienced by the highly relative velocity GNSS satellites thus adjusting their system clocks. This time dilation introduces some small but measurable error in the GNSS signal timing. Gravitational frequency shift, on the other hand predicts that clocks run slower in stronger gravitational fields (e.g., on Earth's surface) than they would if moved to a very low mass-depleted zone such as one located outside Earth´s atmosphere, which includes all GNSS satellites orbiting from there. This difference can also slightly vary the timing of signals sent from the satellites. In the case of SPP, these atmospheric effects are strong enough to introduce positional errors up-to metres in magnitude if not removed. To correct for these relativistic phenomena, GNSSs apply relativistic corrections to the satellite clock data broadcast to users. These corrections are computed ahead of time from the a-priori velocities and orbital elements of satellite (Ashby, 2003). In high-precision applications such as RTK, NRTK or PPP, the same relativistic corrections are applied but in a different manner. For RTK and NRTK, the GNSS base stations continuously study satellite orbits and velocities, and update the corrections as needed to improve accuracy but in the case of PPP, detailed models of satellite orbits and velocities are used to refine the corrections to ensure the signal's time is as accurate as possible. Furthermore, the applications leverage each satellite unique modeled orbit and velocity data to ensure that corrections account for individual satellite conditions.

2.2.4 Ionospheric Delays

The ionospheric delay is one of the most important error sources in positioning with GNSS. The ionosphere is a layer of the atmosphere containing charged particles that acts as a dispersive medium for GNSS signals. That means GNSS signals experience speed changes while travelling through the ionosphere. Signal delay is dependent on signal frequency and conditions affecting the number of charged particles in the ionosphere, such as solar activity or time of day. In SPP, users typically correct for ionospheric delays using a standard ionospheric model, such as the Klobuchar model – the GPS broadcast ionospheric correction model that provides ionospheric delay corrections with a typical accuracy of about 50% (Klobuchar, 1987). This degree of correction is not acceptable in applications requiring high precision, such as RTK or NRTK. The delay caused by the ionosphere becomes immensely reduced in these systems because their dual-frequency receivers can directly estimate the ionospheric delay itself by comparing the time delays of signals received on two different frequencies. While there are models to correct for the effect of the ionosphere, such as Klobuchar, they are generally not precise enough for PPP applications. Therefore, the usual strategies are either to estimate the ionospheric refraction for each satellite as part of the PPP model (Pengfei et al., 2011; Laurichesse & Privat, 2015), or to interpolate the ionosphere refraction from a dense network of nearby stations and provide the estimates to the user as corrections (Banville et al., 2014).

2.2.5 Tropospheric Delays

Tropospheric delay is considered one of the major sources of error for GNSS positioning and is caused by the slowing effect which is as a result of change in medium that takes place on GNSS signals after passing through Earth's troposphere - the lowest layer of the atmosphere. Unlike ionospheric delay, which depends on frequency, tropospheric delay affects all GNSS frequencies equally. The tropospheric delay can be decomposed into two components: a dry component, which comprises around 90% of the total zenith tropospheric delay, and a wet component, which makes up about 10% of the total zenith tropospheric delay (Hopfield, 1969). Being heavily dependent on the refractive properties of the troposphere, the main causes of the delay are dependent on the factors of temperature, pressure, and humidity. In SPP, tropospheric delay is typically compensated by employing standard models (Saastamoinen, 1973; Hopfield, 1969), which calculate the delay with respect to atmospheric condition and satellite elevation angle. Models are normally good to a few metres of accuracy, though this may still be too poor for high precision applications such as RTK or NRTK. In high-precision techniques like PPP, the wet component is difficult to predict as it depends among other factors, on the local water vapour. Therefore, the wet component needs to be estimated in the PPP model. The wet component has a typical magnitude of a few decimetres. Both components are estimated to the centimetre level.

2.2.6 Satellite and Receiver Hardware Delays

Satellite and receiver hardware delays come from some inaccuracies in the electronic components of the GNSS satellites and receivers, along with their respective differences in processing. These can potentially introduce errors in the timing and phase measurements that are so vital for precise positioning in GNSS. Satellite hardware delays are the delays caused due to processing and re-transmission of signal by onboard electronics of a satellite. Although large portions of these errors are modelled in the GNSS through pre-launch calibration, residual errors can still remain and must be corrected for high precision applications. These satellite hardware delays are usually estimated and provided to the user in the form of Timing Group Delays (TGD) corrections, Differential Code Bias (DCB) corrections, or Observable-specific Signal Biases (OSB) corrections. Conversely, receiver hardware delays are caused by the delays introduced to the GNSS signals while processing within the user's receiver. Different receivers, or even different channels of the same receiver, may add different additional delays. These can bias the calculated position solution, especially in systems using phase measurements. For SPP, these delays are typically considered negligible since these errors are within the noise for most applications. However, in the cases of RTK, NRTK, and PPP, where centimetre accuracy is required, these delays are considered significant and must be compensated.

2.2.7 Satellite and Receiver Antenna Corrections

Antenna corrections are necessary because both satellite and receiver antennas have physical and electrical characteristics that can result in errors in GNSS signal measurements. These are predominantly due to changes in the phase center of the antenna and how it interacts with incoming signals as a function of signal arrival direction. When estimated with a global network, satellite orbits tend to refer to the satellite antenna's centre of mass. The satellite antenna phase centre is the apparent point in space from which the GNSS signal is effectively emitted, meaning that users must correct for the lever arm between the satellite's centre of mass and its antenna phase centre. However, this phase centre is not fixed but varies with the angle of the incoming signal due to phase centre variations (PCV). If uncorrected, such variations will introduce biases in the positioning solution, especially in high-precision applications such as Precise Point Positioning. Akin to the satellite antennas, the phase centre of a receiver antenna is not fixed and can be variable depending on the direction of the incoming GNSS signal. Receiver locations usually refer to a point on the antenna called Antenna Reference Point (ARP), therefore requiring accounting for the level arm between the receiver Antenna Phase Centre (APC) and its ARP. In SPP, antenna-related errors are generally within the noise of acceptable levels for applications. However, in high-precision applications such as RTK, NRTK, or PPP, the lever arm values at both the satellite and receiver ends are provided through files called ANTenna EXchange (ANTEX) (Schmid et al., 2016a), which are updated on a regular basis because of new receivers and changes in satellites.

The order of magnitude of antenna corrections is a few centimetres to a few metres, though their uncertainty is only a few centimetres.

2.2.8 Carrier-Phase Wind-Up

Carrier-phase wind-up is a specific GNSS phenomenon, affecting phase measurements used for precise positioning. It depends on the relative orientation between the transmitting satellite and receiving antenna, such that the polarization of the electromagnetic wave is rotated. As signals of GNSS are circularly polarized, any relative rotation between the satellite and receiver antennas results in shifting the phase measurements; if uncorrected, the shift manifests through positioning errors. In SPP, the carrier-phase wind-up is normally not of concern since this technique is mainly based on pseudorange measurements. However, in precise applications where the carrier-phase is used to achieve centimetre accuracy in PPP, RTK, and NRTK, carrier-phase wind-up may introduce significant errors when uncorrected. Carrier-phase wind-up is corrected for by modelling this relative orientation between the satellite and the receiver antenna. These algorithms subtract the phase shift due to wind-up from the measurements (Wu et al., 1992). In this way, the remaining phase measurements correctly represent the true distance between satellite and receiver. The typical magnitudes of carrier-phase wind-up error amount to a few decimetres.

2.2.9 Solid Earth Tides

Solid Earth tides occurs when the gravitational pull from the moon and Sun induce a bulging and squeezing of the Earth's surface due to the Earth’s rotation relative to these space bodies. The effect of the solid Earth tides is vertical and horizontal periodic displacements, reaching up to several decimetres and a few centimetres, respectively. Generally, these displacements are not homogeneous; they depend on the geographical position of an observer and the Moon-Sun geometry. In SPP, the effect of solid Earth tides is usually so small that this effect can be ignored without significantly impacting accuracy. However, in high-accuracy GNSS applications such as PPP, RTK, and NRTK, even these small displacements due to solid Earth tides should be corrected to reach centimetre accuracy. Most GNSS data processing software include models of the solid Earth tides. These models, examples of which are those recommended by the International Earth Rotation and Reference Systems Service (IERS), predict the displacements due to the tides as a function of the observer's location, time of observation and lunar and solar positions (Petit & Luzum, 2010). These models provide corrections applied to the GNSS observations to remove the effects of the solid Earth tides.

2.2.10 Ocean Loading

Ocean loading refers to the deformation of the Earth’s crust resulting from an ocean tide's weight. Due to the rise and fall of the ocean tides, the variation in water mass imparts a force on the Earth's surface, further causing periodic vertical displacements alongside horizontal displacements. These deformations can affect GNSS measurements for stations located near coastlines and therefore should be considered in highly accurate applications. Ocean tides rise and fall with the gravitational pull of the Moon and Sun, and this rise and fall redistributes massive amounts of water on the surface of the Earth. In doing so, it puts varied pressure on the crust of our Earth due to the redistribution of mass, causing deformation to the crust. Ocean loading is known to induce deformation up to a few centimetres based on the location and the height of the tides. This effect is larger for coastal sites and significantly changes over short distances. The ocean loading effects in SPP are normally small, and it can be ignored with no considerable consequence on positioning accuracy. For GNSS high-precision applications, however-such as PPP, RTK, and NRTK, uncorrected ocean loading causes significant errors. This error is especially true for stations that are near coastlines and where the ocean loading effect may be greater. GNSS data processing software incorporates ocean loading models to correct displacements caused by variation in pressure due to ocean tides. For example, such models are developed with the support of IERS and other related services by using data from tide gauges and satellite altimetry to predict ocean loading effects at any specific location and time (Scherneck, 1991). The predicted displacements are applied as corrections to the GNSS observations, thereby mitigating the impact of ocean loading.

Table 2.1 summarizes the measurement error sources, their typical error magnitude encountered in GNSSS positioning and highlights the key mitigation techniques used to minimize their impact on precise positioning applications (Misra & Enge, 2011); (Teunissen & Montenbruck, 2017).

Table 2.1: Numerical summary of GNSS measurements error sources, their magnitudes and mitigation strategies

Error Source	**Magnitude Range**	**Mitigation Approach**
Satellite Orbit Errors	1 – 10 cm (PPP), up to metres (SPPP)	Precise ephemerides, real-time corrections
Satellite Clock Errors	1 – 3 ns (~ 30 cm)	Precise clock products, clock modelling
Relativistic Effects	~ 2.5 cm (orbit), ~ 2 ns (clock)	Modelled using relativistic correction equations
Ionospheric Delays	Up to tens of metres	Dual-frequency GNSS, ionospheric models

Tropospheric Delays	Up to 2.5 m (zenith)	Tropospheric models, estimation in PPP
Satellite and Receiver Hardware Delays	Few centimetres to decimetres	Calibration, bias estimation
Satellite Antenna Phase Variations	Few millimetres to centimetres	Antenna phase centre corrections
Carrier-Phase Wind-Up	Up to a few centimetres	Corrected signal polarization models
Solid Earth Tides	Up to 30 cm	Modelled with tidal correction models
Ocean Loading	Up to 5 cm	Modelled with ocean tide loading corrections

2.3 Geodetic Multi-Constellation, Multi-Frequency PPP Ambiguity Resolution Performance

The development of GNSS in recent decades has been revolutionary; besides GPS, the GLONASS, Galileo, and BeiDou, constellations have been deployed. Added to this multi-constellation environment, new frequency bands considerably strengthen the capability to offer a growing number of GNSS users around the world positioning that is more robust and accurate than ever before (Gao & Shen, 2002; Montenbruck et al., 2018a). Furthermore, these developments are not only beneficiaries for general navigation but also have profound implications in the high-precision geodetic applications. An even more remarkable improvement has been the use of multi-frequency signals emanating from each of these constellations. Multi-frequency GNSS allows for better ionospheric error estimates and reduces multipath effects, leading to robust ambiguity resolution: determination of the integer number of carrier-phase cycles between the satellite and the receiver. Ambiguity resolution is the critical step toward attaining centimetre-level accuracy required in geodetic applications, particularly in PPP (Zhang & Lachapelle, 2001; Geng et al., 2012).

Traditional PPP relies on dual-frequency GPS signals that are usually effective but at the same time translate into longer convergence times and higher susceptibility in more challenging environments. This trend has flipped with the introduction of multi-constellation, multi-frequency GNSS, whereby there is a radical increase in the number of observations available due to increased redundancy and, as such, position solutions are more reliable. This introduction has yielded faster convergence times and more accurate solutions, which in turn can be used in real-time applications, too, where ambiguity resolution needs to be fast and robust (Teunissen & Khodabandeh, 2015; Li et al., 2014).

Ambiguity resolution (AR) in this geodetic multi-constellation, multi-frequency PPP framework represents a quantum leap for GNSS technology. Taking advantage of the new capabilities, PPP will be able to provide centimetre accuracy in a significantly shorter time-a feature that would make the technique possible for a wider application range. This subsection summarizes the literature review regarding geodetic multi-constellation, multi-frequency PPP-AR performance, focusing on these elements that add to increased precision and reliability of geodetic measurements in this advanced GNSS environment.

2.3.1 Ambiguity Resolution

Ambiguity resolution is one of the most important steps in GNSS, particularly to achieve high-precision results as required in geodetic applications. It remains a challenging task to determine the proper integer number of cycles between satellite and receiver, defined as the carrier-phase ambiguity. Hence, the precise resolution of these ambiguities is crucial in achieving centimetre-level accuracy in PPP. Various approaches have been developed in recent years to handle the different methods for ambiguity resolution, all of which have different strengths and weaknesses. Overall, ambiguity resolution has been on an evolutionary track with respect to the development of GNSS. Initial methods concentrated on relative positioning with many receivers where the ambiguities could be resolved by differencing. However, with the advent of PPP, relying on only one receiver, a new challenge was posed. Since differencing would not be possible, new alternative methods had to be developed or sought after for effective ambiguity resolution.

There are three approaches of resolving the carrier-phase ambiguities of a PPP solution. They include the Fractional Cycle Bias (FCB), Integer Recovery Clock (IRC), and the Decoupled Clock Model (DCM). Ge et al. (2008) from the German Research Center for Geosciences initially developed the FCB. They estimated the hardware biases by averaging fractional parts of float ambiguities and apply as corrections to user-estimated ambiguities. Bertiger et al. (2010) from the Jet Propulsion Laboratory also developed FCB by transmitting phase biases and wide-lanes from arcs in global solution and formed phase bias and wide-lane double-differences between receiver and station. Laurichesse et al. (2009) from the Centre National d'Etudes Spatiales (CNES) came out with the IRC. With IRC, the narrow-lane FCBs are assimilated into receiver and satellite clock estimates of the network solution and the wide-lane FCB corrections and satellite-averaging process to fix wide-lane ambiguity. Collins et al. (2008) from the Natural Resource Canada developed the DCM by separating the satellite clocks for pseudorange and carrier-phase observations. This separation allows for the estimation of the receiver hardware biases.

Although all the above three approaches aim to resolve the carrier-phase ambiguities, they differ in methodologies and applications. The FCB method is proven and successful, but it involves immense infrastructure and real-time data processing. While IRC simplifies the processing at the user side by embedding corrections within clock products, it is less practical because of the complexity and dependence on accurate clock products. On the contrary, the DCM is more flexible, robust and better suited for the demands created by modern multi-constellation, multi-frequency GNSS. The DCM decouples clock errors to enable more precise ambiguity resolution, thus improving PPP performance. Shi and Gao (2013) did a comparison of the three ambiguity resolution models and concluded that they are similar in terms of positioning performances. Teunissen and Khodabandeh (2015) studied the relationship between the models and demonstrated equivalence in the ambiguity-fixed user positioning results, ultimately concluding that the models are related through transformations. Considering the advantages presented by the DCM, this thesis focuses on DCM for ambiguity resolution in multi-constellation, multi-frequency PPP. Further, this research discusses more about the technical details on DCM and its impact on accuracy and reliability within PPP solutions.

2.3.1.1 Decoupled Clock Model

The research focuses on the implementation of the Decoupled Clock Model, first introduced by Collins et al. (2008). The choice of this model is justified by the fact that it does not imply any a priori assumptions concerning receiver biases, considered as clock-like terms and thus not mitigated. Besides, it allows solving ambiguity connected with biases and estimating them as integers in a direct way. Abdelazeem et al. (2016) investigated temporal variations in receiver biases and showed that receiver biases can change by several nanoseconds over a period of a few hours. In addition, Wang et al. (2020) analyzed how both long- and short-term changes in receiver bias impact ambiguity stability and positioning accuracy by first resolving receiver biases from ambiguities and then estimating them. The authors concluded that this approach leads to more stable ambiguities and, consequently, allows for faster and more reliable PPP-AR. The model is based on the idea that pseudorange and carrier-phase measurements are not synchronized to the same degree of accuracy, as different clocks are used for these two types of measurements.

The model is based on the GPS ionosphere-free combination, and hence to perform AR, the MW combination must be used. Forming the MW combination allows the estimation of the WL and NL ambiguities and, consequently, their fixing. The DCM removes receiver biases from ambiguities through implicit differencing by the selection of a reference satellite. Implicit differencing results from the fact that receiver clocks become decoupled, and the datum of the phase measurements shifts from the receiver clock to the ambiguities of the reference satellite. Consequently, all estimated ambiguities are relative to those of the reference satellite, which implies that receiver biases are estimated rather than eliminated, unlike in the case of explicit differencing. A major advantage of the DCM approach is that it does not make any assumptions concerning the nature of the biases, since they are considered as white noise when estimated. Collins et al. (2012) further developed the basic DCM to obtain the Extended DCM, where the MW observable is split into narrow-lane pseudorange and wide-lane carrier-phase measurements. This refinement allows for the estimation of the ionospheric delays and, hence, provides the possibility of constraining the ionospheric delays. Shi and Gao (2010) analyzed the integer nature of the ambiguities and the characteristics of the code and phase clocks using the combined DCM. They concluded that the DCM could recover the integer nature of the ambiguities, and they demonstrated that the receiver phase clock is improved compared to the receiver code clock. The authors further find the biases in the receivers to be time-varying, meaning it is necessary to estimate them as white noise.

2.3.1.2 Least-squares AMBiguity Decorrelation Adjustment (LAMBDA): A Method for Ambiguity Resolution

The LAMBDA methodology probably represents the widely used approach in coping with integer ambiguities within GNSS carrier-phase measurements. Introduced by Teunissen (1995), the LAMBDA technique is designed for seeking the most probable integer values corresponding to ambiguities of the carrier-phase observations that represent the key to enabling precise positioning techniques such as PPP, RTK, and other high-precision GNSS solutions. The central challenge in GNSS ambiguity resolution is the determination of the integer number of cycles in the carrier-phase observations. These ambiguities must be fixed to integers if one intends to achieve higher accuracy in positioning. However, the process is further complicated with the noise and biases present in the measurements. The LAMBDA method copes with this challenge by transforming the float estimates of the ambiguities into integers through an efficient search algorithm.

First, the float solution of the ambiguities is obtained through conventional GNSS observation equations. This solution consists of the float ambiguities and their covariances, and the float non-ambiguity state terms which are comprised of the receiver position, clock terms etc. and their covariances. One of the most important augmentations of the LAMBDA method is that it includes a decorrelation step. Ambiguities are often plagued by a high degree of correlation, which can be deleterious to the efficiency of an integer solution search. The LAMBDA method applies a decorrelating transformation that diminishes ambiguity interdependencies and hence enables a much more compact search space and greatly enhances the effectiveness of the integer solution search. After decorrelation, the strategy searches for the most likely integer values for the ambiguities. This strategy is done in a manner where the differences between the float ambiguity estimates, and the possible integer values are minimized through a least-squares adjustment. This search step is highly efficient as the decorrelation step reduces the complexity of the search space. Following the identification of possible integer ambiguity values, the LAMBDA method employs a validation strategy in verifying whether a solution exists. This usually consists of a check to determine whether the integer solution enhances the consistency of the GNSS observations using a ratio test. If the integer solution passes the validation procedure, then the ambiguities are said to have been resolved. Once the ambiguities are fixed with their covariances, they are fused with the other float non-ambiguity state terms and their covariances to update the overall float solution to a fixed solution. The fixing procedure is repeated at every epoch to ensure all the ambiguities are fixed.

2.3.2 Effects of Ambiguity Resolution on PPP solutions

Precise point positioning has now seen extensive applications in fields that demand a centimeter to decimeter accuracy level, especially in geodesy, environmental surveillance, and navigation. However, the convergence period and final solution accuracy are highly dependent on the resolving capability of carrier-phase ambiguities. Ambiguity resolution, particularly integer ambiguity resolution, improves PPP performance by fixing the ambiguities of the carrier-phase measurements to their correct integer values, thus turning the PPP float solution into a PPP fixed solution. A lot of research has been conducted regarding ambiguity resolution and its impact on PPP; producing fundamental knowledge concerning the way in which AR improves the accuracy of solutions, convergence time, and robustness.

Ambiguity resolution directly impacts the accuracy of PPP, since the float carrier-phase ambiguities, which remain real-valued in standard PPP, are converted into integers. Several studies have shown that ambiguity resolution enhances the accuracy of PPP solutions from typical positioning errors at the decimetre-level in float PPP to the centimetre-level in fixed PPP. Ambiguity resolution in PPP was demonstrated by Kouba & Héroux (2001) to provide positioning accuracy improved by nearly an order of magnitude. Without ambiguity resolution, the horizontal errors ranged from 5 to 10 cm, with vertical errors of about 15 to 30 cm, as indicated by the authors. In cases of ambiguity resolution, these were reduced to 1-3 cm horizontally and 3-5 cm vertically. Geng et al. (2012) also reported that ambiguity resolution resulted in an improved overall accuracy of a few centimetres in PPP-AR from several decimetres in PPP-float.

Without ambiguity resolution, one of the most significant issues in PPP is long convergence time to attain a highly accurate solution. The conventional PPP-float solution takes around 30 minutes to some hours for the convergence of centimetre-level accuracy making it unsuitable for most of the time-critical applications. Zumberge et al. (1997) conducted experiments using GPS observations and found that ambiguity resolution reduced the convergence time by nearly half. The convergence time for a float PPP solution was around 40 minutes, whereas the ambiguity-fixed solution reached centimetre-level accuracy in less than 20 minutes. Li et al. (2017) in a more recent study investigated ambiguity resolution effect on real-time PPP performance based on a multi-GNSS approach consisting of GPS, GLONASS, Galileo, and BeiDou. As expected, their results reveal that multi-constellation PPP-AR can reduce convergence time to 10-15 minutes compared with the traditional single-GNSS PPP-float solutions in 30-40 minutes. This is, in fact, attributed to the enlarged number of satellites and better geometry for observations to resolve ambiguities more efficiently.

In summary, ambiguity resolution greatly enhances PPP solution performance in terms of achievable accuracy, convergence time, and reliability. The benefits brought by ambiguity resolution have been demonstrated in numerous studies, particularly when combined with multi-constellation and multi-frequency GNSS. Advanced techniques like the LAMBDA method and multi-GNSS PPP-AR have made PPP a feasible solution for high-precision applications that require both accuracy and timeliness.

2.3.3 Effects of Multiple Constellations and Multiple Frequencies on PPP Solutions

The U.S GPS was historically the first operational GNSS, which was designed to provide the essential PNT services. With higher demand for robustness and accuracy in positioning, more systems have been developed by other nations: the GLONASS from Russia, Galileo from the European Union, and BeiDou from China. The integration of these diverse constellations began to rapidly expand in the early 2000s, with critical milestones including Galileo reaching initial operational capability in 2016 and BeiDou achieving global coverage in 2020 (C. Zhu et al., 2019). With the introduction of these new constellations alongside the pioneer GPS, there is an advantage of utilizing more satellites thereby increasing the number of measurements and improving the geometry of the satellites in space for the users.

Originally, GPS transmitted signals on two frequencies L1 and L2 at 1575.42and 1227.60 MHz respectively. In recent years, a third GPS frequency on the L5 band at 1176.45 MHz has been introduced, with higher power transmissions and targeted towards safety-of-life uses. Galileo was initially designed to broadcast on four frequencies, E1, E6, E5a, and E5b, with the option of tracking E5a + E5b together as AltBOC, Alternative Binary Offset Carrier, which according to Zaminpardaz and Teunissen (2017), is a modulation that combines E5a and E5b to decrease measurement noise. The Galileo E1 and E5a frequencies match with the GPS L1 and L5, respectively, while the E5b, E5, and E6 signals correspond with 1207.140 MHz, 1191.795 MHz, and 1278.75 MHz, respectively. BeiDou has also been designed to broadcast on multiple frequencies with satellites in Medium Earth Orbit (MEO), Geostationary Earth Orbit (GEO) and Inclined Geo-Synchronous Orbit (IGSO). The BeiDou-2 generation is designed to broadcast signals on three frequencies B1-2, B2b and B3 at 1561.098 MHz, 1207.140 MHz and 1268.52 MHz, respectively. The newer BeiDou-3 generation has been designed to broadcast on five frequencies in total (B1, B2a, B2b, B2 and B3), with B1 and B2a coinciding with the GPS L1 and L5 frequencies, respectively, B2b and B3 coinciding with BeiDou-2, and B2 being at 1191.795 MHz. GLONASS also transmits on multiple frequencies. However, the structure of these signals is different from other constellations; employing a Frequency Division Multiple Access (FDMA) technique that results in each satellite broadcasting on a different frequency. The constellation is under modernization with newly launched satellites broadcasting on three Code Division Multiple Access (CDMA) frequencies; that is the same technique used by other GNSS constellations. With all the frequencies that are being broadcast from an increasingly large number of satellites at different constellations, there would be a necessity to shift the attention from the combined dual-frequency processing to an uncombined raw measurements processing to make processing scalable with simplified models that limit the number of possible combinations.

The integration of multiple constellations and frequencies contributes much to PPP solutions by improving accuracy, reducing convergence time and enhancing reliability. To elaborate, Geng et al. (2018) observed a 42% reduction of horizontal positioning errors when Galileo and BeiDou were augmented to GPS and GLONASS. Similarly, Kouba and Héroux (2001) also reported that multi-constellation PPP attained centimetre-level accuracy against the observed decimetre-level accuracy of single-constellation setups. The improvement is attributed to better satellite geometry and increased redundancy for more accurate ambiguity resolution and improved mitigation of errors. Convergence time is the period taken for PPP solutions to attain high accuracy and is critical in real-time applications. The convergence threshold may vary depending on the application needs. The use for multi-constellation PPP can noticeably reduce the convergence time. As an example, Cai and Gao (2013) concluded that adding GLONASS alongside GPS in PPP solution led to a reduction of the convergence time by as much as 40%, from about 30 minutes to approximately 18 minutes. Observations in multiple frequencies bring extra information that contributes to the increase in the success rate of ambiguity resolution. Geng et al. (2012) reported that with the multi-frequency PPP, the ambiguity fix rate increased from 85% to over 98%, which sharply reduced the incorrect fixes and improved solution integrity. Odijk et al. (2016) conducted the experiments that compared single-constellation GPS-based PPP to multi-GNSS PPP solutions. Their results showed that ambiguity resolution was significantly more reliable and efficient in the case of multiple constellations. Thus, the success rate of ambiguity resolution increased from 85% for single-GPS PPP to 98% for multi-GNSS PPP while the convergence time was reduced by nearly 60%.

Combining several GNSS constellations with the use of multiple frequency bands made Precise Point Positioning solutions much more effective. Research has continually shown that improvements in accuracy, reduction of convergence times, and a rise in general solution reliability make multi-constellation, multi-frequency PPP a trustworthy solution for the demanding applications of the modern world. As new GNSS technology proliferation continues, further improvements in receiver performance, signal processing algorithms, and correction services are expected to drive even greater enhancements in PPP performance.

3 Improvements to Existing MCMF PPP-AR Solutions

PPP has been greatly advanced over the last two decades due to developments in MCMF GNSS data and AR methods. Whereas early PPP solutions were based on undifferenced and unambiguous float solutions, recent studies aimed at integer ambiguity resolution (PPP-AR) for performance improvement and convergence time reduction. For example, Guo et al. (2021) explored the integration of Galileo and BeiDou-3 multi-frequency signals, showing that combining these constellations enhances the success rate of ambiguity resolution and reduces convergence times, moving PPP performance closer to RTK performance. Similarly, Li et al. (2020) investigated the use of Galileo's five-frequency signals for PPP-AR, concluding that utilizing combinations of these frequencies, particularly E1/E5/E6, results in faster ambiguity resolution, with convergence times reduced to approximately 16.9 minutes. This demonstrates the power of leveraging more frequency channels to improve the efficiency of PPP solutions. Xiao et al. (2019) further advanced the field by proposing a unified model for multi-frequency PPP-AR, which applies uncalibrated phase delays (UPDs) to improve ambiguity resolution. Their study, which utilized Galileo and BeiDou triple-frequency signals, showed that such an approach significantly boosts resolution efficiency and enhances positioning accuracy. These findings align with those of Qu et al.(2023), who developed a global single-epoch PPP-AR method that integrates multi-constellation and multi-frequency GNSS data. By employing a cascading wide-lane/narrow-lane ambiguity resolution strategy, they achieved centimetre-level accuracy on a global scale, without the need for external atmospheric corrections, highlighting the feasibility of real-time high-precision positioning globally.

This chapter considers some foundational research and develops advanced techniques and methodologies that will enhance the performances of Precise Point Positioning. Its major focus is on refining and extending models and algorithms that have already been developed for significant enhancement of PPP accuracy and efficiency. This chapter aims to advance the performance of PPP using the latest developments in multi-constellation, multi-frequency GNSS data to attain results comparable to RTK solutions on a global scale.

The investigation involves an expansion of the Decoupled Clock Model to include quadruple-frequency measurements and evaluates the redundancy and processing techniques used in the previous work. The enhancements address the limitations of earlier models and provide more robust and flexible solutions for precise positioning. The chapter commences by reviewing the previous advancements and methodologies, followed by a detailed description of the limitations and improvements made, and concludes with an evaluation of their impact on PPP performance.

3.1 Advancement of Decoupled Clock Model in PPP

Previous research related to the PPP technique has seen an important advance based on the extension of the DCM for multi-frequency and multi-constellation data. This extension has ensured more effective GNSS data processing. This overview stems from the previous work of Naciri (2023). The overview highlights the expansion of the DCM to a quadruple-frequency model, an intensive redundancy analysis, and the strategies used in data processing and evaluation.

3.1.1 Expansion of the Decoupled Clock Model (DCM) to a Quadruple-Frequency Uncombined Model

The extension to a quadruple frequency version of the Decoupled Clock Model is considered a significant improvement in GNSS processing. The dual-frequency uncombined DCM through matrix transformation between combined and uncombined observables by Seepersad (2018) was designed to process two frequencies but recently has been extended to four frequencies by (Naciri, 2023) with the aim of improving ambiguity resolution and positioning accuracy. Naciri and Bisnath (2021) re-formulated the dual-frequency uncombined DCM to a triple-frequency uncombined DCM. The latter was a first principles-based re-formulation, derived from fundamental PPP observation equations and set the stage for its extension to a quadruple-frequency uncombined DCM model. In general, the main notion of the DCM is based on the decoupling of the carrier-phase and pseudorange measurement clocks to mitigate mismatch in their precisions. Decoupling the clocks leads to the carrier-phase measurements losing their datum, which was set originally by the pseudorange clocks. The phase datum is recovered by setting one satellite as a reference satellite and assigning it an arbitrary ambiguity value, to which the ambiguities of other satellites will be implicitly differenced. Indeed, decoupling of the carrier-phase and pseudorange measurement clocks will permit more accurate estimation of ambiguities and biases, since the clock errors fall into two categories: pseudorange clocks and carrier-phase clocks Collins et al. (2008).

The previous work explained in detail the required mathematical derivation to be able to include a fourth frequency. This entailed an expansion of the equations to include pseudorange and carrier-phase measurements for the fourth frequency as written in eqn. (3.1), thus providing a complex but accurate model. The pseudorange and carrier-phase measurements of the fourth frequency were integrated into the existing framework first by addressing pseudorange measurements and then incorporating carrier-phase measurements.

$$\begin{cases} P_{r,4}^s = \rho_r^s + c(dt_r - dt^s) + \gamma_4 I_1^s + M_r^s.T_r + \left(b_{r,4} - b_4^s\right) + \epsilon_{P4} \\ \Phi_{r,4}^s = \rho_r^s + c(\partial t_r - dt^s) - \gamma_4 I_1^s + M_r^s.T_r + \lambda_4\left(N_4^s + B_{r,4} - B_4^s\right) + \epsilon_{\Phi 4} \end{cases} \tag{3.1}$$

In Equation (3.1), $P_{r,4}^s$ and $\Phi_{r,4}^s$ are the fourth frequency pseudorange and carrier-phase measurements, respectively. ρ_r^s is the geometric range between the receiver and the satellite, γ_4 is the ratio of the square of frequencies between f_1 and f_4 that maps the first frequency ionospheric delay I_1^s to the fourth frequency. dt_r and ∂t_r are the receiver code and phase clock errors, respectively, M_r^s is the mapping function that is used to map the zenith troposphere wet delay T_r to the satellite-receiver line of sight tropospheric delay, and N_4^s is the fourth frequency carrier-phase ambiguity. $b_{r,4}$ and b_4^s are the receiver and satellite code biases, respectively, and $B_{r,4}$ and B_4^s are the receiver and satellite phase biases, respectively.

From the derivation by Naciri (2023), for satellite s and receiver r, the complete uncombined, four frequency DCM can be written as:

$$\begin{cases} P_{r,1}^s = \rho_r^s + c\left(\overline{dt_r} - dt^s\right) + \gamma_1 \overline{I_1^s} + M_r^s.T_r - b_1^s & + \epsilon_{P1} \\ P_{r,2}^s = \rho_r^s + c\left(\overline{dt_r} - dt^s\right) + \gamma_2 \overline{I_1^s} + M_r^s.T_r - b_2^s & + \epsilon_{P2} \\ P_{r,3}^s = \rho_r^s + c\left(\overline{dt_r} - dt^s\right) + \gamma_3 \overline{I_1^s} + M_r^s.T_r - b_3^s + IFB_{r,3} & + \epsilon_{P3} \\ P_{r,4}^s = \rho_r^s + c\left(\overline{dt_r} - dt^s\right) + \gamma_4 \overline{I_1^s} + M_r^s.T_r - b_4^s + IFB_{r,4} & + \epsilon_{P4} \\ \Phi_{r,1}^s = \rho_r^s + c\left(\overline{\partial t_r} - dt^s\right) - \gamma_1 \overline{I_1^s} + M_r^s.T_r + \lambda_1\left(\overline{N_1^s} - B_1^s\right) & + \epsilon_{\Phi 1} \\ \Phi_{r,2}^s = \rho_r^s + c\left(\overline{\partial t_r} - dt^s\right) - \gamma_2 \overline{I_1^s} + M_r^s.T_r + \lambda_2\left(\overline{N_2^s} - B_2^s\right) + \delta t_{12} & + \epsilon_{\Phi 2} \\ \Phi_{r,3}^s = \rho_r^s + c\left(\overline{\partial t_r} - dt^s\right) - \gamma_3 \overline{I_1^s} + M_r^s.T_r + \lambda_3\left(\overline{N_3^s} - B_3^s\right) + \delta t_{13} & + \epsilon_{\Phi 3} \\ \Phi_{r,4}^s = \rho_r^s + c\left(\overline{\partial t_r} - dt^s\right) - \gamma_4 \overline{I_1^s} + M_r^s.T_r + \lambda_4\left(\overline{N_4^s} - B_4^s\right) + \delta t_{14} & + \epsilon_{\Phi 4} \end{cases} \tag{3.2}$$

with:

$$
\begin{cases}
c\overline{dt_r} = cdt_r + \frac{f_1^2}{f_1^2-f_2^2} b_{r,1} - \frac{f_2^2}{f_1^2-f_2^2} b_{r,2} \\
c\overline{\partial t_r} = c\partial t_r + \lambda_1\left(\delta N_1^{ref} + B_{r,1}\right) - \frac{f_2^2}{f_1^2-f_2^2}(b_{r,1} - b_{r,2}) \\
\bar{I}_1 = I_1 - \frac{f_2^2}{f_1^2-f_2^2}(b_{r,1} - b_{r,2}) \\
\delta t_{12} = \lambda_2\left(\delta N_2^{ref} + B_{r,2}\right) - \lambda_1\left(\delta N_1^{ref} + B_{r,1}\right) - (b_{r,1} - b_{r,2}) \\
\delta t_{13} = \frac{f_2^2-f_3^2}{f_1^2-f_2^2}(b_{r,1} - b_{r,2}) - \lambda_1\left(\delta N_1^{ref} + B_{r,1}\right) + \lambda_3\left(\delta N_3^{ref} + B_{r,3}\right) \\
\delta t_{14} = \frac{f_2^2-f_4^2}{f_1^2-f_2^2}(b_{r,1} - b_{r,2}) - \lambda_1\left(\delta N_1^{ref} + B_{r,1}\right) + \lambda_4\left(\delta N_4^{ref} + B_{r,4}\right) \\
IFB_{r,3} = \frac{f_3^2-f_1^2}{f_1^2-f_2^2} b_{r,1} - \frac{f_3^2-f_2^2}{f_1^2-f_2^2} b_{r,2} + b_{r,3} \\
IFB_{r,4} = \frac{f_4^2-f_1^2}{f_1^2-f_2^2} b_{r,1} - \frac{f_4^2-f_2^2}{f_1^2-f_2^2} b_{r,2} + b_{r,4} \\
\bar{N}_1^s = N_1^s - \delta N_1^{ref} \\
\bar{N}_2^s = N_2^s - \delta N_2^{ref} \\
\bar{N}_3^s = N_3^s - \delta N_3^{ref} \\
\bar{N}_4^s = N_4^s - \delta N_4^{ref}
\end{cases}
\tag{3.3}
$$

In Equation (3.2), for frequency n ∈ {1, 2, 3, 4}, $P_{r,n}^s$ and $\Phi_{r,n}^s$ are the pseudorange and carrier-phase measurements, ρ_r^s is the geometric range between the receiver and the satellite, *c* is the speed of light in a vacuum, γ_n is the ratio of frequencies between the first frequency and frequency *n*, and λ_n is the wavelength for frequency *n.* The satellite corrections from the network side are the satellite orbits in ρ_r^s, the satellite clocks dt^s, the satellite code biases b_n^s, and the satellite phase biases B_n^s. The estimated atmospheric delays are the zenith wet tropospheric delay T_r to which a mapping function M_r^s is applied to map it to the slant direction, as well as the ionospheric delay on the first frequency I_1^s, which is mapped to the delay on frequency *n* through the factor γ_n. The receiver biases and clocks are at the core of the DCM. For these state terms:

- $\overline{dt_r}$ and $\overline{\partial t_r}$ are the decoupled pseudorange and carrier-phase receiver clocks, respectively. The estimation of two receiver clocks is due to the decoupling of clocks which, consequently, leads to losing the datum for carrier-phase measurements. The datum in those measurements is recovered through selecting a reference satellite, not estimating its ambiguities, and setting them to arbitrary integer values instead. Consequently, the datum on each frequency's carrier-phase measurements is set by the reference satellite's ambiguity on that frequency. Therefore, $\overline{N_n^s}$ is the integer single-differenced ambiguity for satellite relative to the reference satellite. The differencing is done implicitly when choosing one satellite as reference, as there is no need to manually difference measurements or ambiguities,

- δt_{12}, δt_{13}, and δt_{14} are the second, third and fourth frequency's receiver phase biases respectively. The three state terms are all receiver-related and they contain combinations of receiver biases and of the reference satellite's ambiguities. These three state terms are direct consequences of the DCM and of the implicit differencing, as they show up when arranging the reference satellite's measurement equations. Each of the three state terms is specific to the carrier-phase measurements on a specific frequency,
- $IFB_{r,3}$ and $IFB_{r,4}$ are inter-frequency pseudorange biases. These biases are common to any multi-frequency model and arise from the fact that other state terms cannot absorb all the code biases on all frequencies. Indeed, the first and second frequencies' receiver code biases are absorbed by the pseudorange receiver clock and the ionospheric delays, but the third and fourth frequencies' receiver code biases must be estimated as additional state terms, as they would otherwise show up in the post-fit residuals.

The new extension included Galileo's fourth frequency. This integration exploited extra Galileo data to enhance the robustness of the model and came along with careful handling of biases and ambiguities of the new frequency in such a way that additional data had a positive contribution to ambiguity resolution. The expanded DCM allows for the simultaneous processing of dual-, triple-, and quadruple-frequency measurements. The simultaneous processing allows consistency among frequencies and constellations, where the capability of such simultaneous processing furthers the model's capability for better resolution of ambiguities and becomes more comprehensive for a variety of PPP applications. This new quadruple-frequency model thus marks a major change from the old, existing dual- and triple-frequency models. It leverages new data provided by newly available GNSS signals for more accurate positioning solutions and increased insight into ambiguities.

3.1.2 Solution Redundancy Analysis

In PPP, the management of redundancy is of most importance to have maximize degrees of freedom for effective positioning. Previous work pursued a detailed redundancy analysis to assess the impact of adding multiple frequencies and constellations on the performance of the model.

- **Constellation-Dependent States:** The analysis performed showed that the usual state vector in PPP models includes states of receivers, which are dependent on the constellations in use. Each constellation has its own set of unique clock and bias parameters that may make the model even more complex. Previous work overcame this problem by estimating clock and bias parameters for each constellation separately, thus accounting for the time scale differences and biases of various constellations.
- **Reference Satellite Selection:** To effectively handle redundancy, the model must select one reference satellite for each of the constellations. This selection became imperative because receiver biases are constellation-dependent, and ambiguities of a reference satellite are set to arbitrary values to ensure consistency. The model ensured that setting one reference satellite for each constellation meant the additional receiver-related state terms were compensated for by the ambiguities of the reference satellites so that the model's freedoms are not prejudiced. The given analysis treated the generation-related issues with

respect to clock and time delay biases among different generations of BeiDou satellites. To accomplish this analysis, the BeiDou-2 and BeiDou-3 constellations were handled differently within the modelling. This approach allowed one to estimate generation-specific biases or to deploy separate reference satellites for each generation so that the accuracy and reliability of the model can be kept without any deterioration.

- **Redundancy and Degrees of Freedom:** It was shown that, despite the addition of multiple frequencies and constellations, the extended DCM has a similar degree of redundancy and degrees of freedom as the conventional PPP models. This conclusion was achieved by ensuring that ambiguities of the reference satellite were not estimated but instead used to compensate for the extra receiver-related state variables.

The redundancy analysis thus verifies that the improved DCM achieved a crucial balance between accuracy and complexity, providing a robust framework that deals with multiple frequencies and constellations without compromising model performance.

3.1.3 Processing Strategies

The previous work used a global set of the 27 IGS stations shown in Figure 3.1 with the criteria of each station supporting three GPS frequencies, two GLONASS frequencies, four Galileo frequencies and the ability to track newer BeiDou satellites. Table 3.1 shows the frequencies of each constellation used for the processing. The processing was done for over a week period from DOY 305 to 311, 2021, with observation data collected at 30-second interval and divided into three-hour datasets. 1448 three-hour datasets were processed in total to ensure the volume of data was high enough to draw meaningful conclusions regarding the expanded DCM accuracy and reliability. The York-PPP engine was used to process the data. York-PPP engine is a specialized software package PPP developed at York University in C/C++ programming languages. It is designed for high-precision GNSS data processing, supporting both geodetic-grade and low-cost GNSS datasets. The software supports multi-constellation, multi-frequency GNSS data processing and incorporates advanced methodologies, such as the Decoupled Clock Model (DCM), which provides improved ambiguity resolution. York-PPP engine supports efficient processing of large datasets, making it suitable for scientific research, geodesy, and low-cost hardware applications. Both combined (i.e. ionosphere-free combination) and uncombined PPP solutions are provided, enabling the ability to try new algorithms and investigate GNSS performance in varying situations.

Processing was performed in kinematic mode without assuming the static conditions of the stations to ensure the expanded DCM is evaluated on realistic grounds. Processing was done in the uncombined PPP approach as raw undifferenced pseudorange and carrier-phase measurements are processed separately. This approach estimates ionospheric delays explicitly, allowing for improved ambiguity resolution in the multi-frequency GNSS scenario.

Table 3.1: Selected frequencies for each constellation used for the processing

Constellations	**Selected frequencies**
GPS	L1 (1575.42 MHz), L2 (1227.60 MHz) and L5 (1176.45 MHz)
GLONASS	G1 (1602 + $\frac{9}{16}$k MHz) and G2 (1246 + $\frac{7}{16}$k MHz)
Galileo	E1 (1575.42 MHz), E5b (1207.140 MHz), E5a (1176.45 MHz) and E6 (1278.75 MHz)
BeiDou-2	B1-2 (1561.098 MHz), B2b (1207.140 MHz) and B3 (1268.52 MHz)
BeiDou-3	B1C (1575.42 MHz), B2a (1176.45 MHz) and B2b (1207.140 MHz)

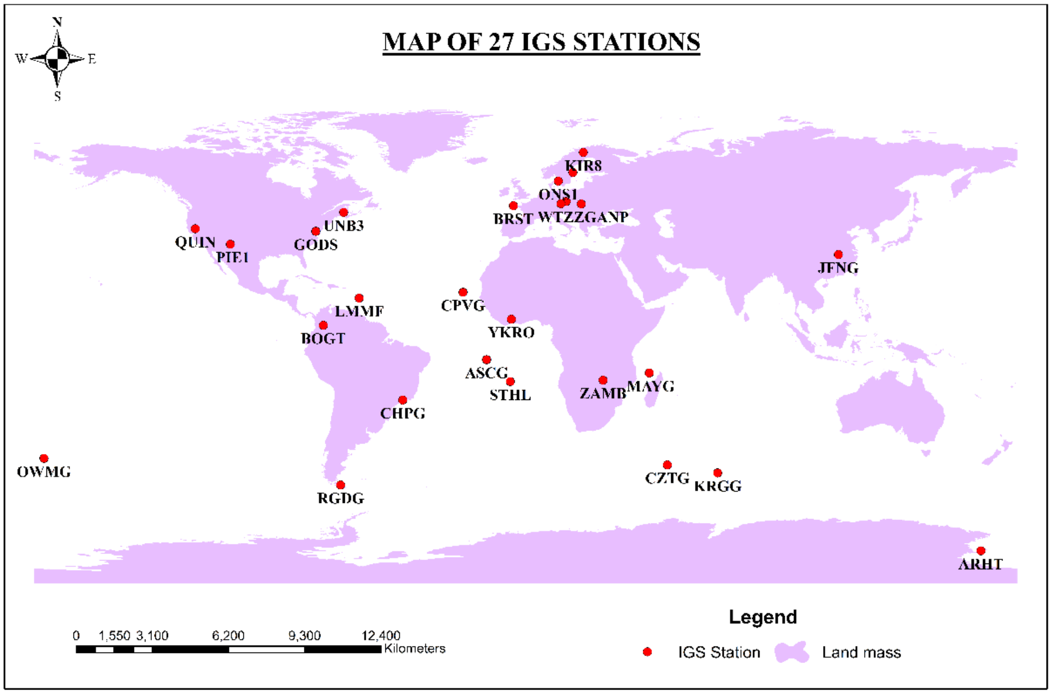

Figure 3.1: Map of IGS stations used for the processing

The previous work used satellite products comprised of precise satellite orbits and clocks generated by GeoForschungsZentrum (GFZ) (Deng et al., 2017), and a bias file containing both code and phase biases provided by CNES (Laurichesse & Blot, 2016) and are compatible with GFZ products to generate a PPP-AR solution. The IGS14 ANTEX file was used for the satellite and receiver antenna corrections (Schmid et al., 2016b). Previous work weighted the measurements with some specific strategies, considering different qualities of the GNSS signals. Different frequency pseudorange and carrier-phase measurements from the same satellite were weighted equally, but the weighting of the BeiDou measurements was set to half of the other constellations due to BeiDou-3 being a relatively new constellation at that time and to avoid any unwanted behaviour because of the quality of either the products or the signals. The Modified

Least-squares AMBiguity Decorrelation Adjustment (MLAMBDA) method by Chang et al. (2005) was used for ambiguity resolution. By means of this method, the uncombined float ambiguities and covariances of each frequency were used as inputs to the function and converted into fixed ambiguities. Then these fixed ambiguities were used in updating the state terms, with their validation based on a ratio test. Ambiguities were fixed for GPS, Galileo and Beidou because they use the Code Division Multiple Access (CDMA), while the ambiguities for GLONASS were not fixed because it uses the Frequency Division Multiple Access (FDMA). Table 3.2 lists the estimation parameters and strategies which were employed in determining the various states in the expanded DCM.

Table 3.2: Processing strategy of estimated parameters

Parameters	**Strategy**
Receiver coordinates	Estimated with process noise equivalent to 100 km/h
Receiver reference coordinates	IGS SINEX positions
$\overline{dt_r}$ and $\overline{\partial t_r}$	Estimated as white noise processes
δt_{12}, δt_{13}, δt_{14}, $IFB_{r,3}$ and $IFB_{r,4}$	Estimated as white noise processes
Tropospheric delay	Dry: GMF model and mapping function (Kouba, 2009) Wet: estimated as a random walk process with process noise of 0.05 mm/$\sqrt{h}$
Ionospheric delays	Estimated as white noise processes
Ambiguities	Estimated as constants on each continuous arc
Elevation angle cut-off	7°
Weighting strategy	Elevation dependent weighting: $\sigma = \frac{\sigma_{90}}{a+b\sin el}$ with σ_{90} equal to 0.1 m and 0.001 m for the pseudorange and carrier-phase measurements, respectively, and *el* being the elevation angle. *a* and *b* are determined based on a residual and measurement quality analysis and set to 0.15 and 0.85, respectively

3.2 Limitations in BeiDou-3 Handling and Enhancements in the York-PPP Engine

In the existing York-PPP engine which processes MCMF PPP-AR data, some limitations are identified most especially for handling of BDS-3 clock information. Given these limitations, some modifications have been done in improving BeiDou-3 to increase the performance of the solution. Key improvements made are represented in the addition to a fourth frequency processing, thereby making BDS-3 the second constellation with a quadruple frequency uncombined DCM in the York-PPP engine (Galileo being the first). This improvement not only aligns BDS-3 with the rest of the global constellations but allows much more flexibility in ambiguity resolution and reduces convergence times.

3.2.1 Handling Errors in BeiDou-3 Clock Information within the York-PPP Engine

One important limitation that has been noticed in the York-PPP engine is that the BDS-3 clock information is handled incorrectly in the design matrix. Although there is a correct separation of measurements between BDS-3 and BDS-2 into different columns, reflecting their different characteristics, the clock information from BDS-3 is not handled in a separate manner; instead, the BDS-3 clock data have been integrated into the same column as that of BDS-2 clock data as shown in Equation 3.6.

From Equation 2.1 and ignoring the satellite clock term, ionospheric delay term, tropospheric delay term, satellite and receiver code and phase biases, and ambiguity term, for simplicity, the equation becomes:

$$\begin{cases} P_{r,n}^{s} = \rho_r^s + cdt_r + \epsilon_{P,n} \\ \Phi_{r,n}^{s} = \rho_r^s + cdt_r + \epsilon_{\Phi,\mathrm{n}} \end{cases} \tag{3.4}$$

where:

$P_{r,n}^{s}$ and $\Phi_{r,n}^{s}$ are the pseudorange and carrier-phase measurements, respectively, ρ_{r}^{s} is the geometric range from the satellite, s, to the receiver on Earth, r, c is the speed of light in a vacuum, dt_r is the clock term of the receiver and, $\epsilon_{P,n}$ and $\epsilon_{\Phi,\mathrm{n}}$ are the pseudorange and carrier-phase noises, respectively.

From Equation 3.4, the design matrix including the clock terms for BeiDou-2 and BeiDou-3 and ignoring that of GPS, GLONASS and Galileo, can be written as:

$$\mathrm{A} = \begin{bmatrix} \frac{\partial \rho_1}{\partial x} & \frac{\partial \rho_1}{\partial y} & \frac{\partial \rho_1}{\partial z} & c_{BDS-2} & c_{BDS-3} \\ \frac{\partial \rho_2}{\partial x} & \frac{\partial \rho_2}{\partial y} & \frac{\partial \rho_2}{\partial z} & c_{BDS-2} & c_{BDS-3} \\ \vdots & \vdots & \vdots & \vdots & \vdots \\ \frac{\partial \rho_n}{\partial x} & \frac{\partial \rho_n}{\partial y} & \frac{\partial \rho_n}{\partial z} & c_{BDS-2} & c_{BDS-3} \end{bmatrix} \tag{3.5}$$

Previously, the design matrix was formed as:

$$\mathrm{A} = \begin{bmatrix} \frac{\partial \rho_1}{\partial x} & \frac{\partial \rho_1}{\partial y} & \frac{\partial \rho_1}{\partial z} & c_{BDS-2/3} \\ \frac{\partial \rho_2}{\partial x} & \frac{\partial \rho_2}{\partial y} & \frac{\partial \rho_2}{\partial z} & c_{BDS-2/3} \\ \vdots & \vdots & \vdots & \vdots \\ \frac{\partial \rho_n}{\partial x} & \frac{\partial \rho_n}{\partial y} & \frac{\partial \rho_n}{\partial z} & c_{BDS-2/3} \end{bmatrix} \tag{3.6}$$

Merging BDS-3 and BDS-2 poses a significant problem in calculating clock biases and ambiguity resolution since the two operate under different systems with distinct clock properties. BDS-2, being the regional constellation system where the main service area is the Asia-Pacific region, has different clock biases and timing characteristics compared to BDS-3, which is the global constellation system just like GPS, GLONASS and Galileo. Having the clock information of the two systems combined into one column can make the software unable to model accurately the two different time behaviors. This mismodelling results in incorrect calculation of the BDS-3 receiver clock that will directly impact on the precision of the PPP solution, especially when BDS-3 is used as a primary contributor to the solution. In most precise positioning, especially within a multi-constellation multi-frequency PPP framework, each constellation should have its own column for clock information in the design matrix. For example, in the case of BeiDou, BDS-3 being a global constellation, must have a column for the clock information like other global constellations such as GPS, GLONASS and Galileo. Since the BDS-3 clock data are combined with the BDS-2 data in an incorrect manner, the software incorrectly assesses the true contribution given by BDS-3, which significantly degrades ambiguity resolution and the PPP solution.

Another limitation is derived from the weighting strategy adopted for processing BeiDou measurements. For the improper handling of the BDS-3 clock information in the previous work, all the BeiDou measurements, including BDS-2 and BDS-3, were given half weighting with respect to the measurements contributed from other global constellations, such as GPS and Galileo. This lower weight was pursued to mitigate the impact brought by the clock-related issues described above. This weighting approach undervalues the contribution of BDS-3 as a global system and hence diminishes its role within the overall PPP solution. Because BDS-3 is a global constellation, it deserves full weight in the PPP processing chain, just like GPS and Galileo. In contrast, it should be applied only to constellations like GLONASS, for which carrier-phase ambiguities are not resolved within the current software. GLONASS uses FDMA instead of CDMA used by GPS, Galileo, and BeiDou, which introduces additional difficulties for resolving the carrier-phase ambiguities. For that reason, GLONASS is less useful for high-precision positioning; therefore, the weight for the GLONASS measurements is half the weight of the other constellations. By adapting the weighting strategy to reduce the contribution of GLONASS and take that of BDS-3 at full value, the global accuracy of the PPP solution improves.

3.2.2 Impact of Handling Errors of BeiDou-3 Clock Information on Position Dilution of Precision (PDOP) and Ambiguity Resolution

The incorrect handling of BDS-3 clock information has a great impact on the position dilution of precision (PDOP) calculation for BDS-3-only solutions. PDOP is a parameter used to describe the satellite geometry quality, which once more influences the overall accuracy of the positioning solution. Ideally, as a global constellation, BDS-3 should provide favourable PDOP values, especially when used in combination with other global systems. However, because the BDS-3 clock information has been combined with BDS-2, the software does not correctly compute the PDOP of the BDS-3-only solution. This incorrect computation of PDOP inflates the value of PDOP for BDS-3 or deteriorates its value, hence poor geometry. This improper calculation would imply a deteriorated PPP solution in the regions where the main satellite coverage is provided by BDS-3, for instance, in global scenarios outside the Asia-Pacific region. For this reason, these poor PDOP values are difficult to process with precision from a software point of view, especially if there is a significant reliance on BDS-3 signals. As such, proper BDS-3 clock data separation will contribute to improving satellite geometry calculation accuracy and subsequently, the accuracy of the PPP solution. Figure 3.2 shows the BDS-3 only processing of station KIR8 in Kiruna - Esrange, Sweden on 19 DOY, 2024. The 24-hour data was processed in the sequential least squares processing mode in the York-PPP engine. At the bottom of Figure 3.2 is the number of satellites tracked and the PDOP values. The PDOP values for all epochs of the data are zero, showing the improper calculation of this parameter in the software. It is stemmed from the assignment of the BDS-3 clock data into the index of BDS-2. In the design matrix, which plays a vital role in the calculation of the DOP values, the index of BDS-3 clock data are populated with zeros thereby resulting in the zero PDOP values throughout the 24 hours. The software needs to be tuned to handle the clocks from BDS-3 differently than those from BDS-2 as seen in Equation 3.5, to get accurate PDOP calculations with a correct contribution of BDS-3 in the overall satellite geometry. This is expected to greatly improve the performance of BDS-3 standalone solutions due to better positioning accuracy and smaller convergence time.

The same can be said about the ambiguity resolution process, which is vital for high-precision positioning in PPP. In this respect, each constellation has its specific set of carrier-phase ambiguities from their respective satellites, which should be resolved to enable accurate positioning. Incorrect calculation of clock estimates after merging the BDS-3 and BDS-2 clock data results in software difficulties in resolving those ambiguities correctly. On top of Figure 3.2 is the float and fixed horizontal solution. The results show how fluctuated both the float solution (carrier-phase ambiguities are not resolved) and the fixed solution (carrier-phase ambiguities are resolved to integers) are. The float solution led to improper fixing of the carrier-phase ambiguities in the ambiguity resolution stage of the processing. This poor solution is caused by the incorrect BDS-3 clock estimates from the float solution, thereby not helping in correctly resolving the carrier-phase ambiguities. Correct ambiguity resolution is of utmost importance in multi-constellation, multi-frequency PPP aiming to provide more precise positioning after eliminating errors in the carrier-phase measurements. If ambiguities are not correctly resolved, they considerably degrade the positioning solution, resulting in increased convergence times. Proper separation of BDS-3 clock data from BDS-2 is highly necessary to ensure the software resolves the carrier-phase ambiguities for both systems correctly, hence increasing accuracy and reliability in the PPP solution.

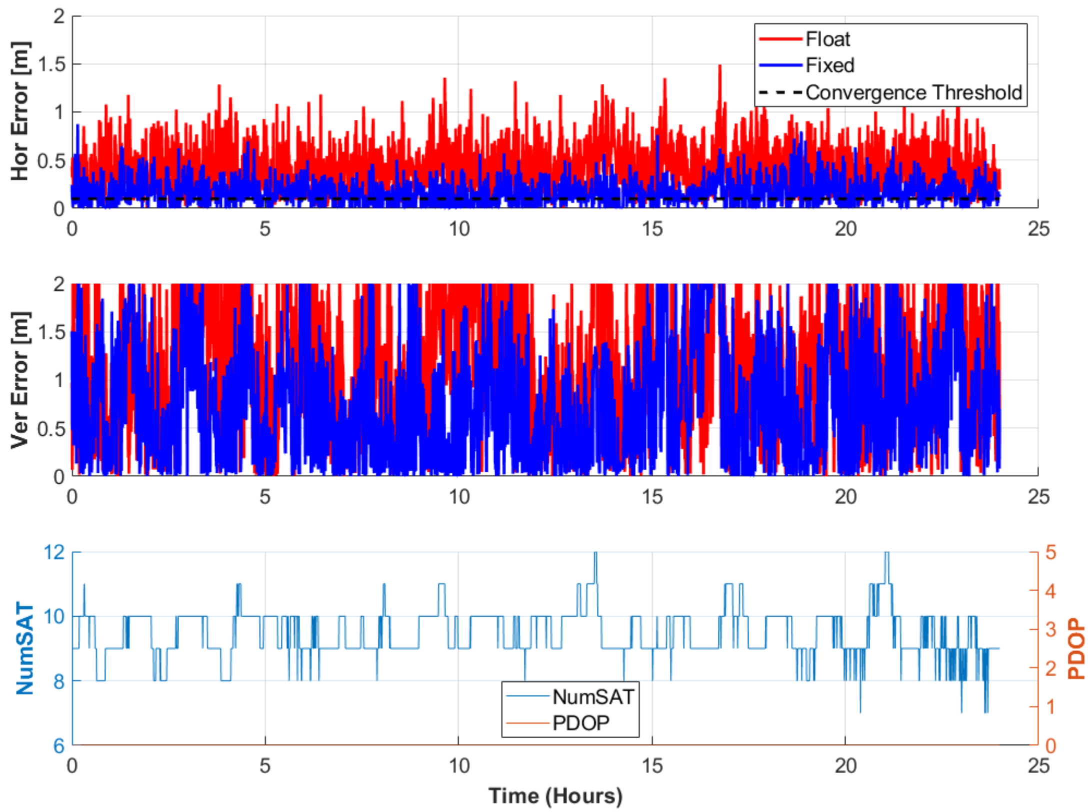

Figure 3.2: BDS-3-only processing of station KIR8 on DOY 019, 2024 before improvements. Top: Float and fixed solution for horizontal solution; Middle: Float and fixed solution for vertical solution; Bottom: Number of satellites tracked and Position Dilution of Precision.

3.3 Impact of BeiDou-3 Enhancements in the York-PPP Engine

The modifications carried out on the York-PPP engine have enhanced its capability to handle BeiDou-3 data, especially with the separation of clock information between BDS-2 and BDS-3, and incorporation of a fourth frequency for processing BDS-3. A 24-hour dataset from station KIR8 in Kiruna - Esrange, Sweden on 19 DOY, 2024 was used to evaluate the performance of the system before and after these changes, leading to striking improvements in both the float and fixed solutions. Indeed, prior to these improvements, the software was unable to correctly handle the

BDS-3 clock information and thus PPP float and fixed solutions never converged. This limitation has now been overcome with the improvements, and the results of the dataset analysis now consistently achieve faster and more reliable convergence.

With the introduction of the improvements, both float and fixed solutions of the horizontal and vertical positioning started to successfully converge in Figure 3.3. A convergence threshold of 10 cm was set to determine the convergence times of the float and fixed solutions of the horizontal positioning. In the 24-hour dataset, the convergence of the float solution was attained in 199.5 minutes (which is approximately three and a half hours), while that of the fixed solution, which requires resolving carrier-phase ambiguities, was attained in 9.0 minutes. In the hours between 3 and 5, there is a bump in the float solution, and without the jump the float solution would have converged within a few tens of minutes. This noticeable bump is attributed to a reduction in the number of satellites tracked at the initial epoch of the bump. Fewer satellites lead to high PDOP and degrades the solution quality and increases positioning errors. These changes also significantly improved the overall positioning accuracy as shown in Table 3.3. The use of the 67^{th}, 95^{th} and 100^{th} percentile metrics in evaluating the performance is to respectively represent typical accuracy (rms – equivalent), integrity-bound for safety and worst-case errors, ensuring a comprehensive assessment of positioning reliability and robustness. Both horizontal and vertical errors reduced by approximately 90% for both float and fixed solutions at the 100 percentiles. This magnitude of improvement is very important for users in regions of good BDS-3 coverage, since the constellation can now be relied on to achieve high-precision positioning. This enhancement is in sharp contrast with the pre-improvement stage in which the solutions failed to converge at all. These improvements also positively impacted the PDOP values for BDS-3-only solutions, which previously degraded to zeros through the epochs been processed. From Figure 3.3, the 24-hour datasets recorded an average PDOP value of 2, which is comparable to those from other constellations. Therefore, separation of BDS-2 and BDS-3 clocks enabled the software to treat the two constellations independently and calculate the clock estimates well, which were continuously improving the general satellite geometry of BDS-3-only solutions. In conclusion, the unmodeled errors in the positioning solution were reduced, enabling convergence and increased accuracy.

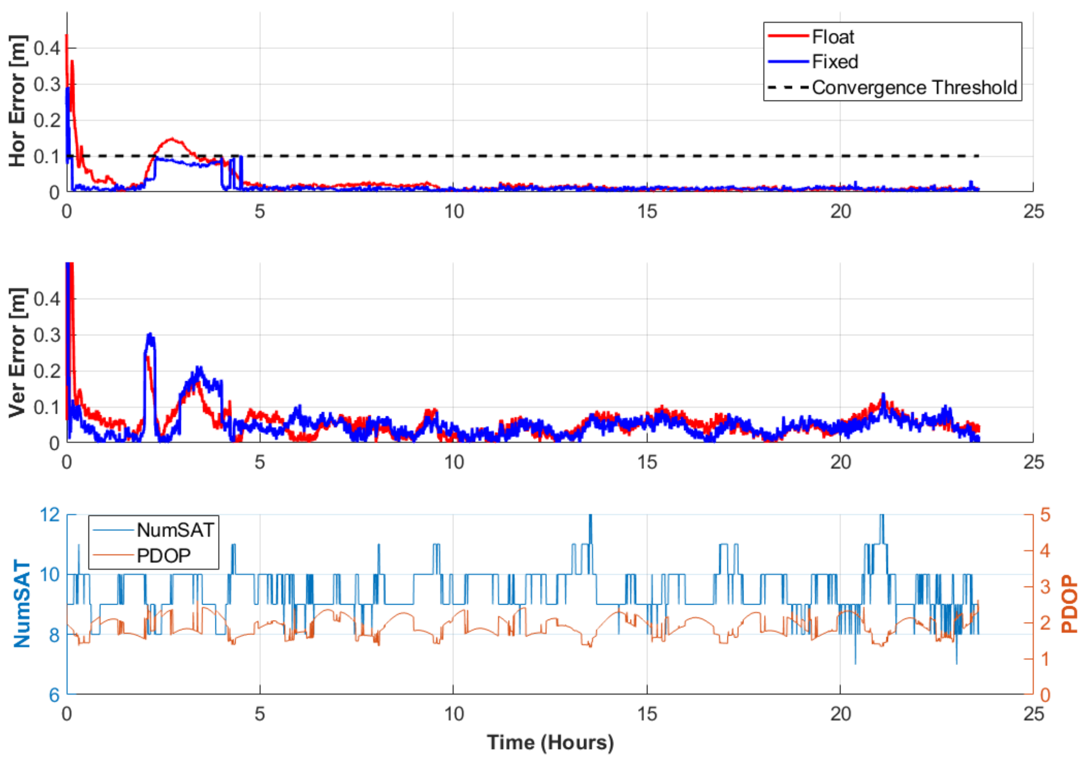

Figure 3.3: BDS-3-only processing of station KIR8 on DOY 019, 2024 after improvements. Top: Float and fixed horizontal solution; Middle: Float and fixed vertical solution; Bottom: Number of satellites tracked and PDOP.

Besides the clock separation, the introduction of the fourth frequency for BDS-3 processing also played an important role in improving performances. Previously, BDS-3 was processed with three frequencies, exactly as BDS-2. However, the addition of the fourth frequency at 1268.52

MHz brought BDS-3 processing in line with the modern multi-frequency capabilities of Galileo, which also processes four frequencies in the uncombined DCM. The additional frequency introduced increases redundancy in the measurements that would help in resolving ambiguity resolution quickly and provided better accuracy.

Table 3.3: Statistics of BDS-3-only horizontal and vertical positioning accuracy at 67th, 95th and 100th percentiles before and after improvements

	Percentiles (%)	**Horizontal Positioning (cm)**		**Vertical Positioning (cm)**	
		Float	**Fixed**	**Float**	**Fixed**
Before Improvements	**67**	32.2	12.6	89.3	50.7
	95	44.9	19.8	141.5	89.0
	100	48.9	22.5	159.7	104.0
After Improvements	**67**	1.0	0.7	3.2	2.7
	95	2.7	1.7	4.9	4.1
	100	4.6	2.8	7.4	7.3

Figure 3.4 shows the horizontal accuracies of BDS-3-only processing of station KIR8 on 19 DOY, 2024 on dual-triple frequency and all frequencies. The all-frequencies is the processing of dual, triple and quadruple frequencies together in the York-PPP engine. The addition of the quadruple frequency had a tremendous impact on both the float and fixed solutions, as horizontal errors are reduced in epochs where the dual-triple struggled. Note that a good float solution plays a pivotal role in obtaining a good, fixed solution. From Figure 3.4, the dual-triple frequency processing yielded a poor float solution, thereby resulting in a poor fixed solution with their

percentile rms shown in Table 3.4. The overall positioning accuracy saw a reduction of the horizontal errors by 77% and 88% for float and fixed solutions, respectively, with the inclusion of the fourth frequency and its measurements serving as redundant measurements.

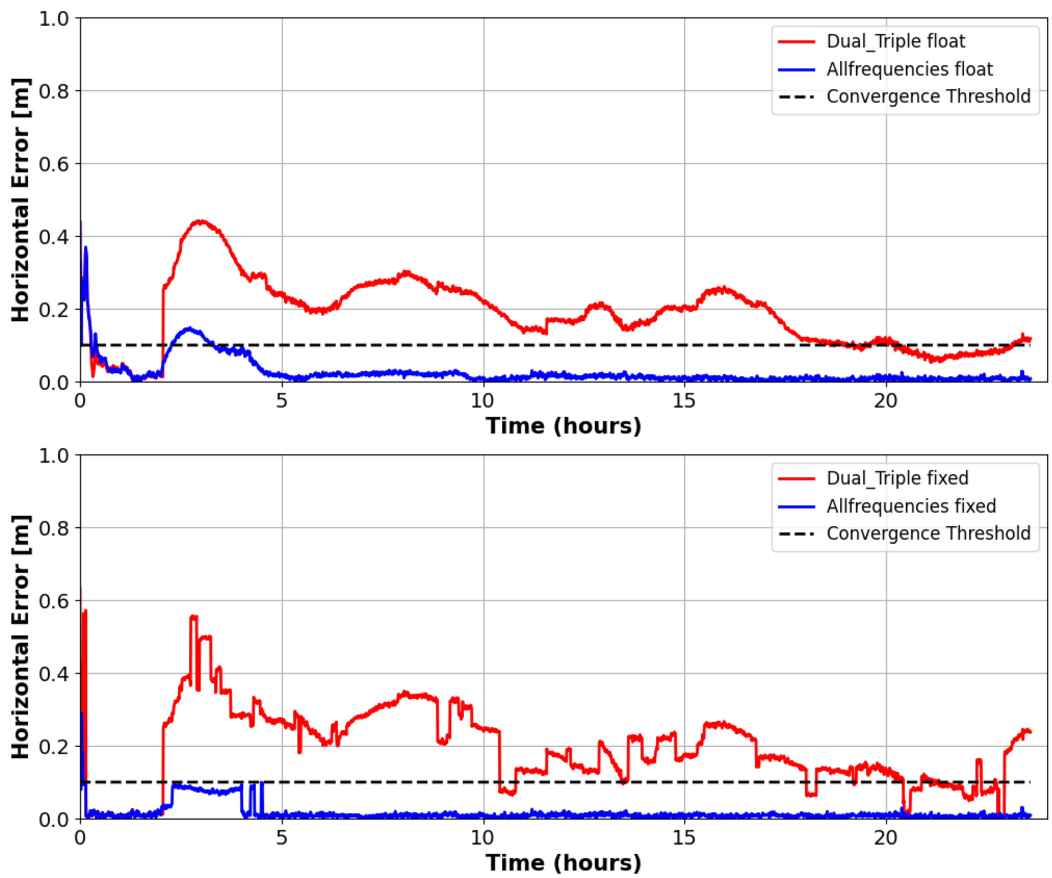

Figure 3.4: BDS-3-only processing of station KIR8 on DOY 019, 2024 on dual-triple frequency and all frequencies (dual, triple and quadruple mixed). Top: Float solution; Bottom: Fixed solution for horizontal solution.

Table 3.4: Statistics of BDS-3-only horizontal positioning accuracy at 67th, 95th and 100th percentiles for dual-triple and all frequencies processing for data processed in Figure 3.4

Percentiles	**Dual-Triple Frequency**		**All Frequencies**	
(%)	**Float (cm)**	**Fixed (cm)**	**Float (cm)**	**Fixed (cm)**
67	14.6	15.0	1.0	0.7
95	19.1	20.2	2.7	1.8
100	20.8	22.0	4.7	2.8

Moreover, the ambiguity resolution success rate significantly improved after the modifications. Separation of clock information and addition of the fourth frequency enabled the system to resolve ambiguities correctly even in the most difficult conditions when obstruction of signals or poor satellite geometry would have previously caused problems in ambiguity resolution. Figure 3.5 depicts the ambiguity success rate of BDS-3-only processing of station KIR8 before and after the improvements. There is an average success rate of 58% for the pre-improvement stage and almost a 100% average success rate for the improvement stage. This enhancement reflects an improvement in the general performance of the York-PPP engine, where the success rate of ambiguity resolution increased to over 95% in most cases. This mean success rate is a large increase compared to pre-improvement rates, which were generally low due to mixed clock information and limited frequency options.

The migration of BDS-3 from three to four frequencies within PPP processing represents a significant contribution toward multi-constellation PPP-AR with improved integration and performance, regarding the interaction with other constellations like GPS, Galileo, and GLONASS. Thus, adding this fourth frequency to the BDS-3, the multi-constellation PPP solution sees an increase in the total number of observations. Every additional frequency from BDS-3 adds greater independence of observations, hence increasing redundancy when combinations of data from the different constellations are considered. The processing of multiple constellations together, such as GPS, Galileo, BeiDou, and GLONASS, provides the system with increased robustness for dealing with signal disruptions or satellite outages because of additional frequencies from BDS-3. For instance, when there is a temporary unavailability of, or weak signals from, GPS satellites, BDS-3 provides quadruple-frequency observations that give the extra measurements necessary to maintain the robustness and continuity of the PPP solution.

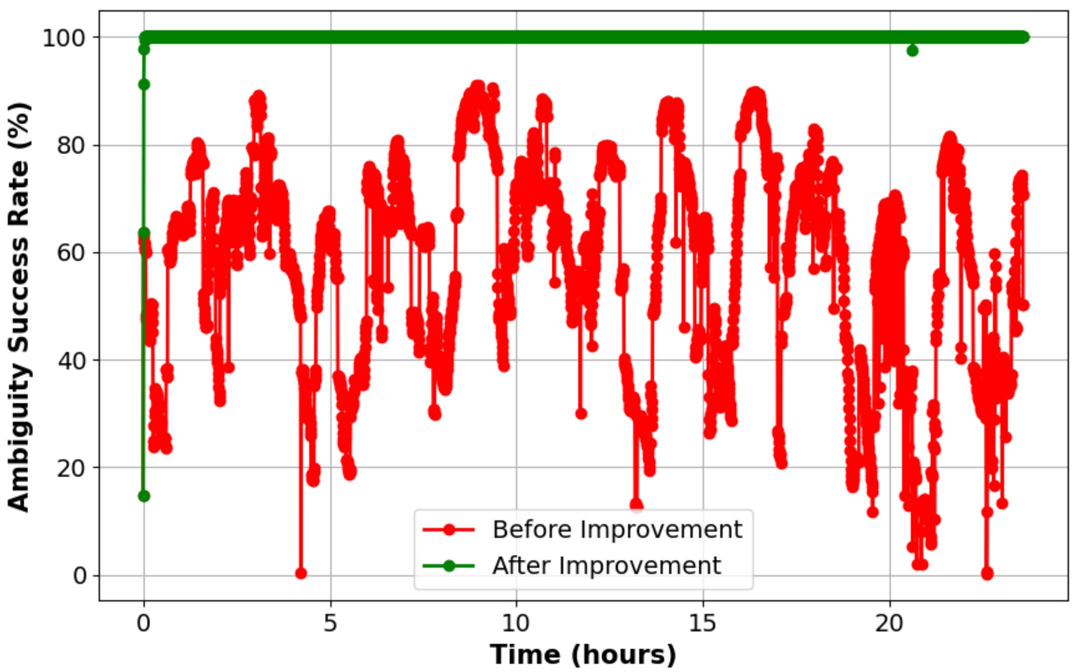

Figure 3.5: Ambiguity success rate of BDS-3-only processing of station KIR8 on DOY 019, 2024 before and after improvements.

In multi-constellation PPP, PDOP values are widely used to evaluate the satellite geometry impact on positioning accuracy. Figure 3.6 shows the multi-constellation, multi-frequency PPP-AR processing of station KIR8 on DOY 019, 2024. The multi-constellation consists of processing from GPS, GLONASS, Galileo and BeiDou, and the multi-frequency involves processing three frequencies from GPS, two from GLONASS, four from Galileo, and four from BDS-3. From Figure 3.8, there is an average PDOP of approximately 1 across the 24-hour data. This PDOP value is notable with the combination of measurements from all constellations and their available frequencies. This improvement is well worth it, especially in challenging environments, given that satellite visibility may be poor or limited, for example, in urban canyons. Which, when this is the case, would mean that even while the signals of other constellations, such as GPS and Galileo, are weak or obstructed, the system can still provide accurate positioning using the extra measurements from BDS-3 serving as redundant measurements.

One of the key performance drivers for MCMF PPP is reducing convergence times. Expanding BDS-3 to four frequencies means access to a larger pool of data for the York-PPP engine, hence faster convergence for both float and fixed solutions. Besides, BDS-3 contributes the additional frequency when combined with GPS, Galileo, and GLONASS for more measurements that can contribute to faster ambiguity resolution and hence stabilize the positioning solution sooner. From Figure 3.6, the float solution converges at 4.5 minutes, whiles the fixed solution converges instantaneously. These convergence times indeed is an enhancement, especially in global applications where the extended frequency coverage from BDS-3 would play a significant role in maintaining fast convergence across diverse regions and environments.

Recent research has demonstrated the benefits of using BDS-3 signals in the PPP-AR context, resulting in improvements in convergence time and positional accuracy. Yang et al. (2024) showed that using all four civil frequencies of BDS-3 enabled rapid ambiguity resolution with 2.2 cm and 8.9 cm horizontal and vertical accuracy, respectively. The results of BDS-3-only solution of this thesis with horizontal and vertical accuracy of 2.8 cm and 7.8 cm, respectively, confirm their observations, showing comparable accuracy with small differences based on satellite visibility. Li et al. (2022) showed that the inclusion of BDS-3 in a multi-GNSS PPP-RTK system resulted in better fixing rates and accuracy, with a success rate of 93.7% for ambiguity resolution. Likewise, this research shows a BDS-3-only ambiguity success rate of more than 95% and indicates that the integration of BDS-3 with GPS, GLONASS and Galileo significantly improves convergence, especially under conditions of poor visibility. Li et al. (2019) showed triple-frequency PPP to be more accurate and faster-converging than dual-frequency, which similar results were replicated, though this research findings used triple and quadruple frequencies. The results in Figure 3.4 and Table 3.4 attest to the fact that, increasing frequency indeed improves accuracy and convergence speed.

Precise measurement from multiple frequencies is heavily relied upon in PPP ambiguity resolution. Therefore, with four frequencies contributed by BDS-3, ambiguity resolution benefits from an increased data pool, making the resolution of integer ambiguities more attainable and faster. In the case of a multi-constellation setting, the contributions provided by each constellation enhance the system. This assertion is because the introduction of the fourth frequency into BDS-3 will finally allow it to contribute to ambiguity resolution in a more assured manner when working in combination with other constellations.

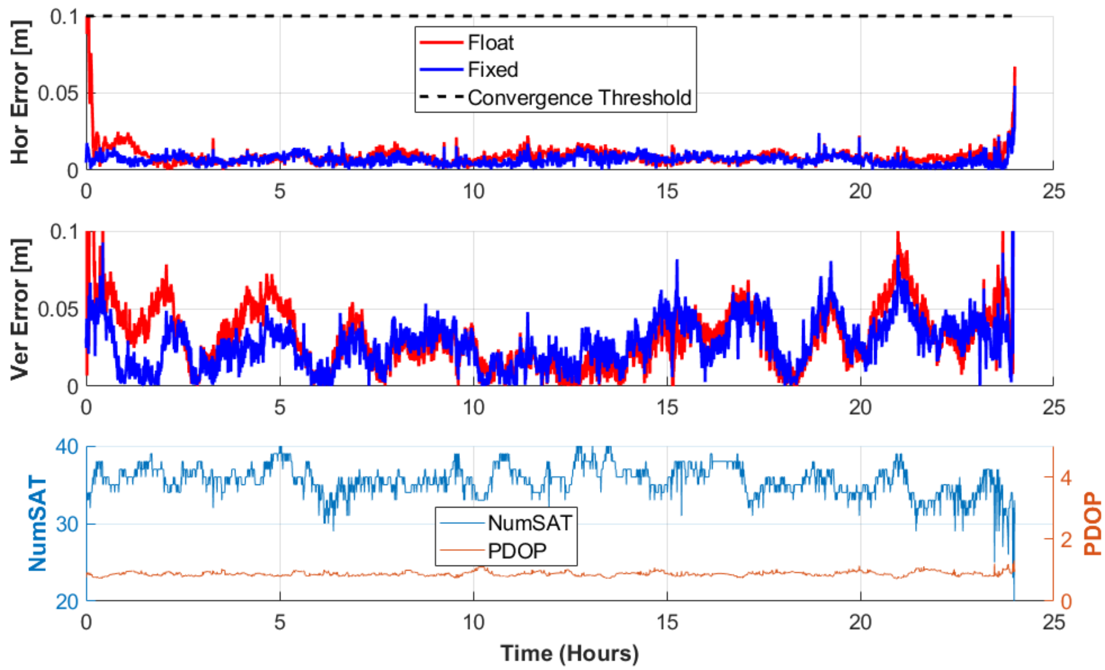

Figure 3.6: Multi-frequency multi-constellation (GREC) PPP-AR processing of station KIR8 on DOY 019, 2024. Top: Float and fixed horizontal positioning solution; Middle: Float and fixed vertical positioning solution; Bottom: Number of satellites and PDOP.

3.4 Overall York PPP Performance Improvements

This subsection provides a detailed comparison between the results of this current study and the previous work by Naciri (2023), to investigate improvements brought about by the inclusion of quadruple-frequency signals from the BeiDou-3 constellation and explicit separation of clock terms between BDS-2 and BDS-3 satellites. In total, 1448 global datasets were reprocessed using identical approaches to those used in the previous study. This many datasets enable direct evaluation of the impacts that these upgrades bring about in the general PPP performance. Improvements in convergence time, positioning accuracy, and ambiguity resolution are considered, since such aspects represent the key purposes to increase precision for global applications.

3.4.1 Comparison of Horizontal, Vertical, and Convergence Time Statistics for Fixed Solutions

Figure 3.7 shows the time series of the average horizontal and vertical errors of the current results at all-frequency (dual, triple and quadruple mixed) processing from all 1448 datasets. Processing was done for multiple constellations with three-frequencies for GPS and BDS-2, two-frequency for GLONASS and four-frequencies for Galileo and BDS-3. The time series depicting current results are of great help in understanding what improvements the incorporation of additional frequency of BDS-3 and separation of BDS-2 and BDS-3 clock terms have brought into the performance of PPP solution. Among the remarkable improvements is the reduction of the initial position error. It can be seen from the time series that initial horizontal errors are much smaller with the addition of the quadruple-frequency solution. These smaller initial errors are extremely important for positioning applications that rely on fast positioning accuracies, as they allow more rapid transitions from float to fixed solutions. Besides the initial error reduction, there is a big improvement in convergence time-the time series presents instantaneous convergence, as opposed to previous results that would show gradual convergence. For the first few hundred epochs of this time series, the horizontal position solution rapidly stabilizes to its final value, thus showing the advantage multiple frequencies can have in more quickly fixing ambiguities with greater accuracy. This instance means a quadruple-frequency model allows the solution to resolve ambiguities faster and more successfully for a more reliable and more precise fixed solution in a shorter time frame. Besides, it reflects the robustness of the current model by considering the stability of the solution over time in a time series. According to the Figure 3.7, position errors, especially horizontal errors, remain small during the whole processing, thus additional frequency incorporated presents more advantages.

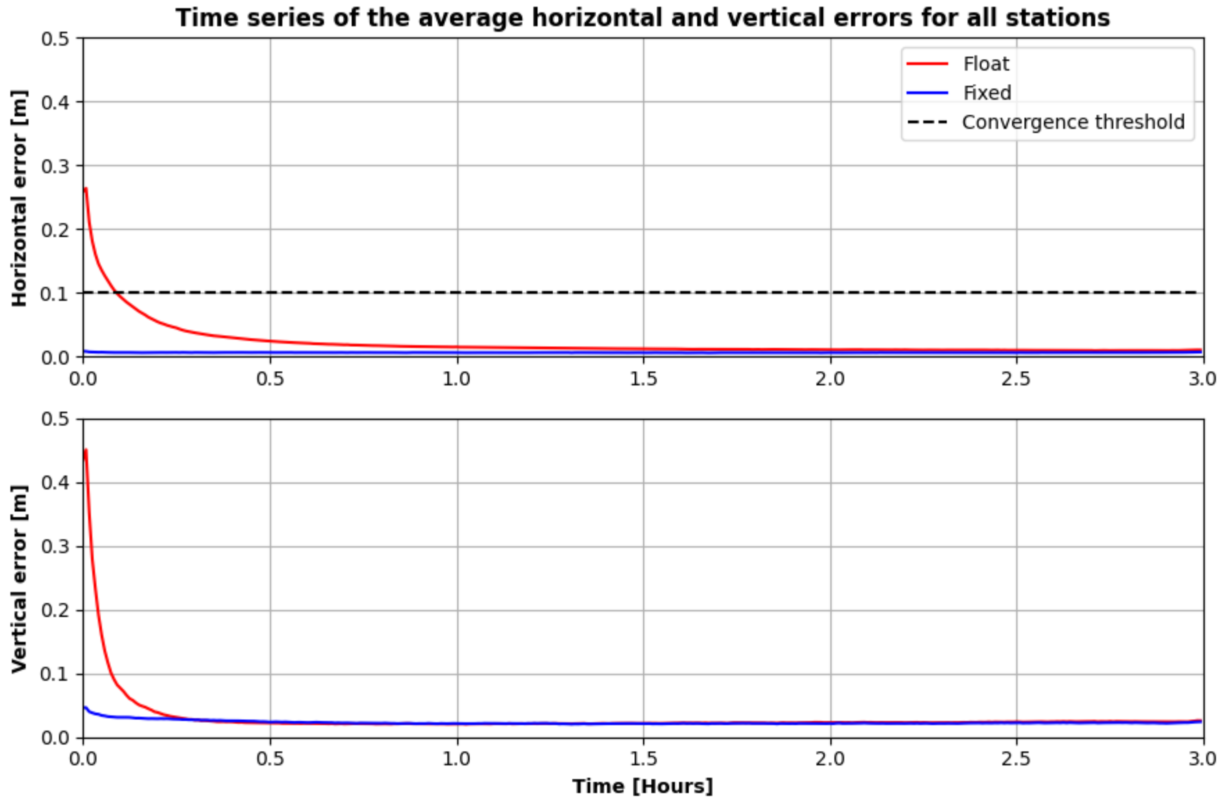

Figure 3.7: Time series of the average horizontal and vertical errors of the current results at all-frequency (dual, triple and quadruple mixed) processing for all constellations.

Figure 3.8 compares the fixed solution statistics of the current and previous work (Naciri, 2023). The current solution shows a slight improvement in horizontal rms error, particularly at the 95th percentile, reducing from 1.2 cm to 1.1 cm. At the 100th and 67th percentiles, the horizontal rms errors remain at 2.0 cm and 0.7 cm, respectively. These improvements reflect the benefits of resolving carrier-phase ambiguities using extra frequencies, mainly from BDS-3. The vertical rms errors remain nearly unchanged, with a slight reduction from 5.6 cm to 5.4 cm at the 100th percentile, while the 95th and 67th percentiles remain at 4.0 cm and 2.2 cm. This limited improvement is likely due to satellite geometry and atmospheric effects. The most significant advancement is in convergence time. The current solution achieves instantaneous convergence at all percentiles, compared to up to 1 minute at 100th percentile in the previous work. This massive reduction, enabled by BDS-3's quadruple-frequency signals, enhances real-time GNSS applications by providing faster and more reliable positioning.

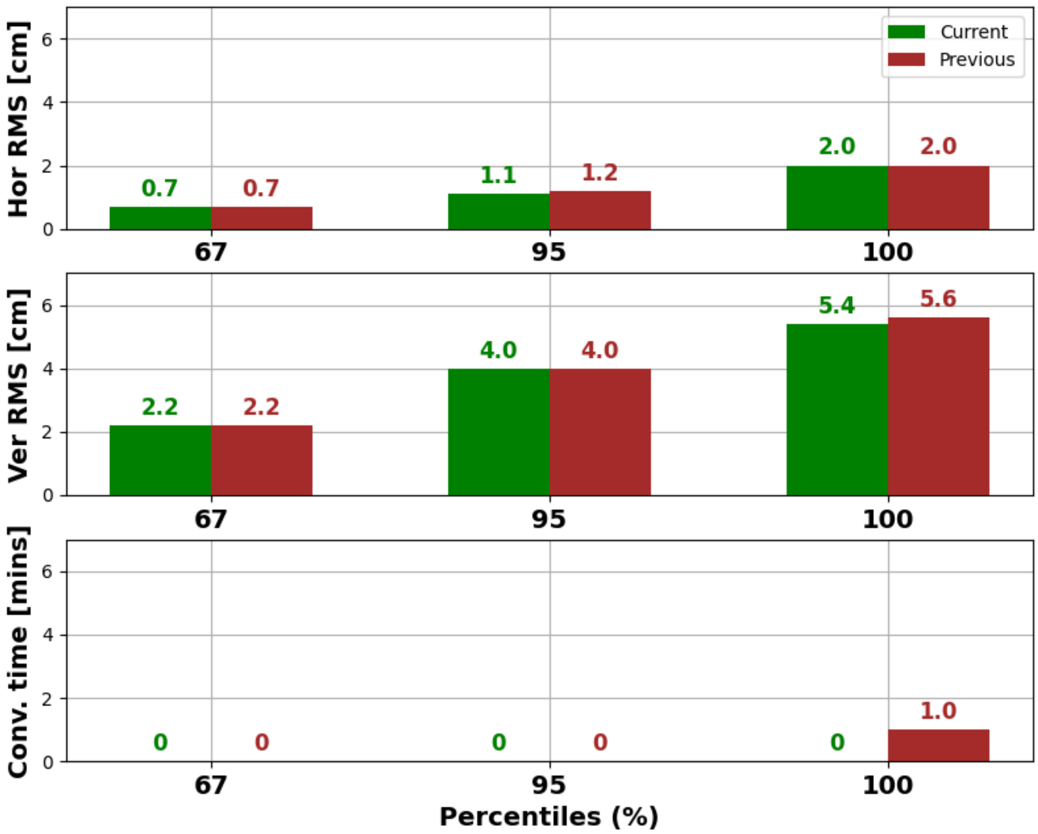

Figure 3.8: Statistics of the average fixed solutions from the current and previous solutions at 67th, 95th and 100th percentiles. Top: Horizontal rms; Middle: Vertical rms; Bottom: Convergence time to 10 cm horizontal error.

3.4.2 Comparison of Convergence Times for Individual Stations

Figure 3.9 shows on top the 95th percentile average convergence times to 10 cm per station and on the bottom, it shows the 67th percentile average convergence times to 2.5 cm per station.

While fixed solutions for all-frequency processing remain the focus of this study, results are much better in comparison with previous results. In addition, based on previous work, the fixing of ambiguities on dual and triple frequencies has resulted in significant reductions in convergence time. The value added from the quadruple-frequency capabilities of the BDS-3 system in this analysis is presented to further advance positioning performance. Station CZTG was omitted from the current study as BDS-3 measurements were not present in the dataset and would distort the statistics of the analysis.

With the top of Figure 3.9 which is the convergence times to 10 cm per station, an impressive percentage of the stations realizes convergence instantaneously. The current work depicts that 81% of the stations converge instantaneously, which is an improvement of 18% over the previous work where it was reported that 63% of the stations had attained instantaneous convergence. This improvement attests to the efficiency of the quadruple-frequency approach in BDS-3, and the separation of the clock terms for BDS-2 and BDS-3 thereby improving the reliability and efficiency of the positioning solutions. Indeed, the convergence times have been reduced at most of the stations. For example, the convergence time in the earlier work was 2.0 minutes for BOGT; it is now 1 minute. Similarly, for LMMF, it has come down from 3.0 to 1.5 minutes. Such reductions are important in that they reflect the capability of the technology to serve applications that need speed and accuracy. The consistency in convergence times across various stations give further credence to the work. For example, the ASCG station solutions are greatly improved from 1 minute to 0 minutes, hence offering improved reliability to provide instantaneous solutions. This consistency will go a long way towards extending the use of GNSS in dynamical applications where rapid positioning accuracy is crucial.

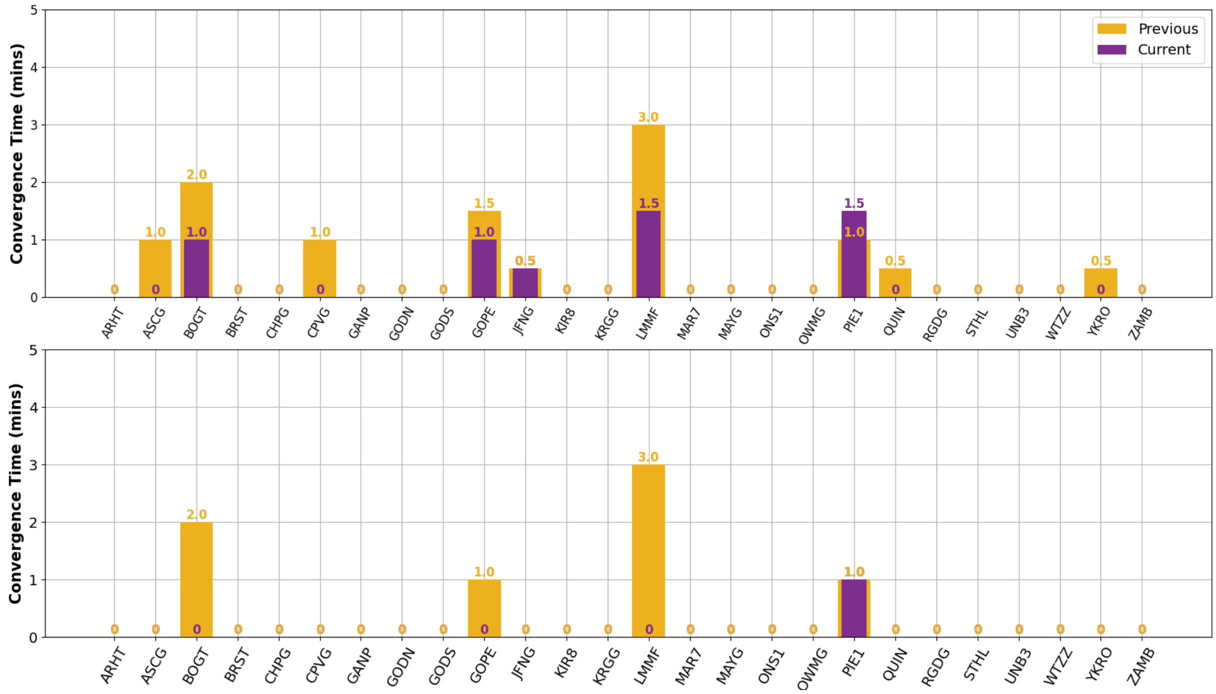

Figure 3.9: Top: 95th percentile average horizontal convergence times to 10 cm per station; Bottom: 67th percentile average horizontal convergence times to 2.5 cm per station.

The bottom of Figure 3.9 shows the convergence times to 2.5 cm per station, a more stringent threshold, as used in the previous work. The results explore the 67th percentile performance as representative of the rate at which the stations can converge to near-instantaneous positioning as part of efforts to satisfy (N)RTK-like requirements described by Bisnath et al. (2013). For the rate of instantaneous convergence to the threshold, it increased from 89% in the previous study to 96% of the stations in this current study. That is, only station PIE1, did not converge instantaneously. This enhancement represents a 7% improvement, which means that nearly all stations reach the intended accuracy without delay. The better performance is attributed to quadruple-frequency of the BDS-3 processing, better ambiguity resolution, and better separation of clock terms in the current solution.

3.4.3 Epoch-by-Epoch Solution Performance

In other to further compare the MCMF PPP-AR performance to RTK performance, the previous work processed all datasets using an epoch-by-epoch filter, where each epoch is treated independently without making use of any past information. PPP classically relies on sequential estimation filtering. This estimation carries the information acquired in previous epochs to enhance estimates of the parameters in successive epochs. This approach is effective for ambiguity resolution but is based on continuous satellite visibility and previous data, which may be problematic since cycle slips or interruptions in the signals could introduce errors. However, the results of previous studies showed that with MCMF PPP-AR, convergence to centimetre accuracy can be achieved near-instantaneously.

Figure 3.10 reflects the difference in the percentage epochs of stations that achieved horizontal error below the 2.5 cm threshold at the 100th percentile for this work and the previous study. A strict criterion for assessing performance across all epochs has given further insight into the robustness and reliability of the multi-constellation, multi-frequency PPP-AR model. Of the selected 26 stations, as station CZTG has been omitted, 21 showed improved performance at an epoch-by-epoch level. While ARHT maintained the same performance, with no difference within the current and previous work, four stations showed a decline in performance. Thus, the average of all stations in the percentage of epochs where the horizontal error was below 2.5 cm has increased from 62%, within the previous work, to 72% in the current study, which marks an overall improvement of 10%.

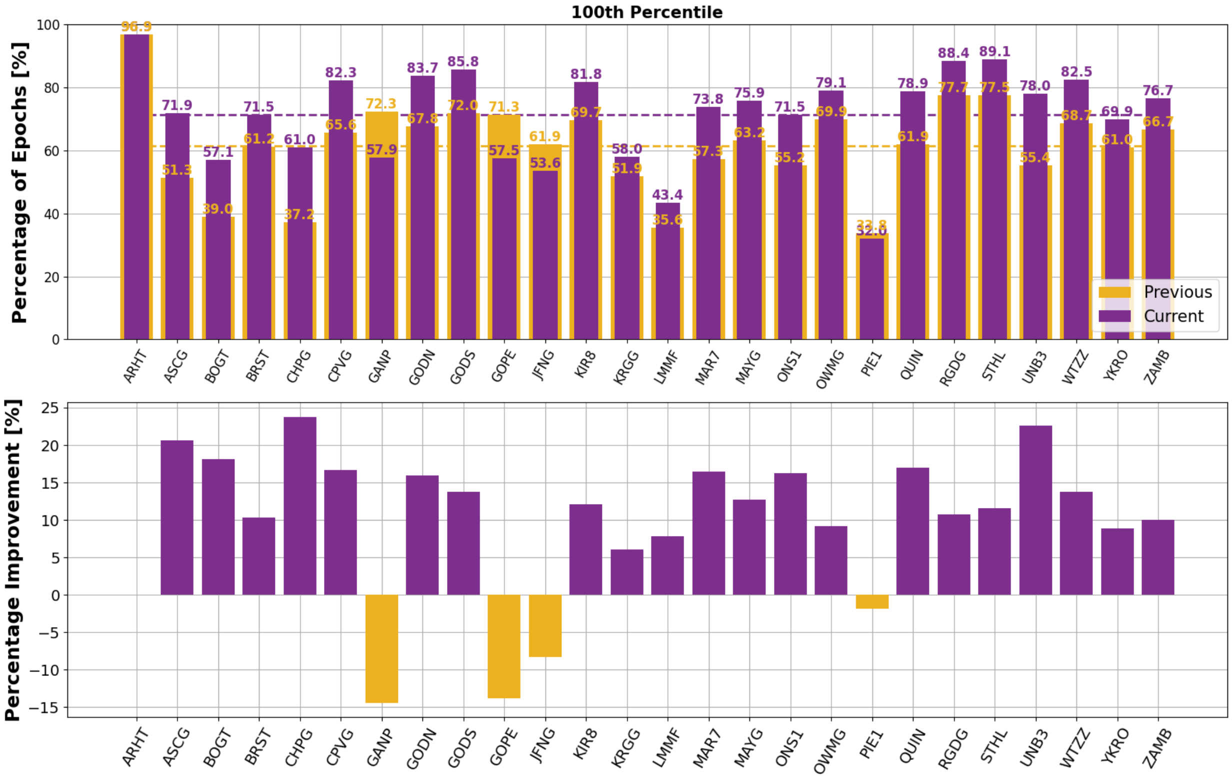

Figure 3.10: Top: Percentage of epochs with horizontal errors below 2.5 cm per station in the epoch-by-epoch solutions at 100th percentile over one week; Bottom: Difference in percentage between current and previous work.

Substantial benefits can be seen for the stations like ASCG, CHPG, and UNB3 with improvements in 20.6%, 23.8%, and 22.6% respectively, hence reflecting new capabilities of the current MCMF PPP-AR system. For GANP and GOPE, there was a decline in the performance, with values of 14.4% and 13.8%, respectively. This declination might be due to station-specific factors, which include difficult satellite geometry, poor signal quality, or multipath interference that is perhaps not mitigated in the present model for such stations. Station JFNG also indicate some degradation of performance with 8.3% degradations, respectively. This negative trend may point to problems with either specific satellite constellations or environmental conditions that, at these stations, have impacted this model in terms of yielding consistent sub-centimetre accuracies.

It can also be due to the improper separation of the BDS-2 and BDS-3 clock terms in the previous work. This clock handling error could have helped the percentage in the previous work to increase abruptly though the assignment of the clock terms for BDS-3 in the design matrix was wrong. While there is slight degradation of performance at some of the stations, most of the stations still indicate very positive improvements with respect to demonstrating this model's potential for RTK-like positioning accuracy without relying on local augmentation systems.

Figure 3.11 depicts the comparison between the current study and the previous work for epoch-by-epoch performance at the 67^{th} percentile. In the previous work, the single epoch PPP achieved sub-2.5-centimetre horizontal accuracy at the 67^{th} percentile with over 81.4% of the epochs from all stations; it was impressive for a PPP solution. Many of the stations showed strong single epoch performances in that analysis, as more than 80% of epochs were exceeding the threshold for many of them. The instantaneous accuracy of this performance showed the more and more evident potentiality for multi-constellation, multi-frequency PPP to attain precision close to RTK. In the present work, for most of the stations under study, improvements are recorded. Indeed, the improvement in performance is recorded for 21 out of 27 considered stations compared with the previous work's significant gain. For instance, ASCG improved by 19.4%, going from 73.8% to 93.2%, BOGT followed suit with a 20.1% increase to 77.4%, CHPG saw the most significant rise by around 30.5%, amounting to 86.0% altogether and UNB3 also showed a fair increase of 17.5% to 95.9%. These results indicate that changes in the design matrix by separating the BDS clocks terms and additional frequency from BDS-3 have brought significant improvements in performance. The present work attained an average of 88.4% of epochs below the threshold of 2.5 cm for all the stations. This rise in percentage is a significant improvement from the earlier average of 80.4%. Among the reduced performing stations is GANP which saw a decrease of 11.8%.

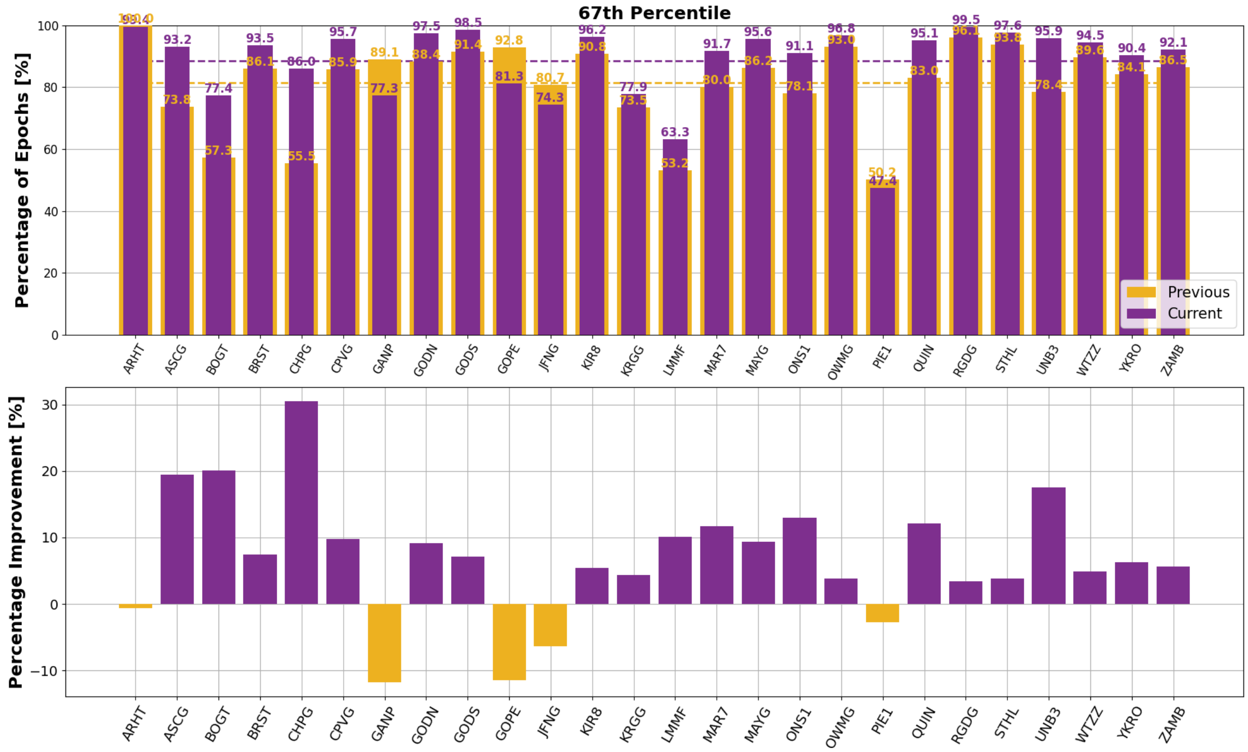

Figure 3.11: Top: Percentage of epochs with horizontal errors below 2.5 cm per station in the epoch-by-epoch solutions at 67th percentile over one week; Bottom: Difference in percentage between current and previous work.

While the performance at the 67th percentile in this study does indicate that an implementation of a MCMF PPP model does indeed improve positioning accuracy overall, performance at the 100th percentile does reveal a few stations systematically performing better than others. This disparity in performance points to questions that are fundamental to the investigation that will be based on the following chapter of this thesis:

1. What is required to increase the average number of epochs within the 2.5 cm accuracy from 80% to higher percentages?

2. Why is it that the position performance of some stations is worse than others?

4 Position Outliers in Multi-Constellation, Multi-Frequency PPP

The position outliers are critical to assess geodetic Multi-Constellation Multi-Frequency (MCMF) Precise Point Positioning with ambiguity resolution performance. These outliers in the positioning represent measurements that deviate significantly from their expected values, potentially distorting high-precision GNSS solutions. MCMF PPP-AR uses signals from all GNSS constellations, and all available frequencies to increase solution availability and robustness. However, while these many measurements from all constellation and their available frequencies introduce the possibility of achieving even higher accuracy, they introduce additional sources of error leading to outliers (Karaim et al., 2018). Outliers in PPP solutions arise mainly from several factors such as signal degradation due to atmospheric effects, multipath, and cycle slips (Qu et al., 2024; Xu et al., 2023). This challenge is even more complex since the various constellations and frequencies at which the receivers operate will have different signal strengths and thus be susceptible to these types of errors in different ways (Li et al., 2022). It is easy to realize that these outliers have an important effect on instantaneous ambiguity resolution and hence prevent reaching centimetre-level accuracy in single-epoch positioning. It was recently shown that ambiguity resolution across multiple frequencies allows mitigation of some of these effects, but significant errors can still occur due to unresolved outliers (Zhao et al., 2023; Naciri & Bisnath, 2020). So far advanced statistical methods which include Mahalanobis distance statistics, have been successful in outlier identification and mitigation within the datasets obtained from GNSS (Magyar et al., 2022; Giménez et al., 2012). By this approach, the observations that are considerably far away from the expected are identified; thus, increasing the precision of the PPP solution (Magyar et al., 2022). It is required that the method of outlier detection is robust enough, such that erroneous measurements are recognized and treated accordingly without compromising the integrity of the solution in general. Therefore, knowing the root causes of the outliers is vital in improving the performance of PPP-AR. Among these are factors such as satellite geometry represented by PDOP, the number of measurements, and signal redundancy which contribute to the outliers (Naciri & Bisnath, 2020). With the study of such factors, future models will attempt to minimize the presence of outliers in enhancing the reliability and accuracy of the single-epoch PPP solutions. Furthermore, the addressing of the outliers may allow the RTK-like performance to be attained in PPP-AR. With the continuous evolution of multi-constellation, multi-frequency systems, similar advancements should be implemented in techniques for handling outliers to ensure that the additional complexity brought about by new signals and constellations from these emerging systems translates into improved positioning accuracies. In this chapter, an analysis of outliers regarding epoch-by-epoch MCMF PPP-AR performance is focused to find patterns, understand causes, and discuss the implications on positioning accuracy.

4.1 Geodetic MCMF PPP-AR Epoch-by-Epoch Outliers

In the quest to detect outliers in a geodetic MCMF PPP-AR epoch-by-epoch solution, datasets from 29 IGS stations, shown in Figure 4.1, which broadcast on up to four frequencies for the constellations of interest, are amassed over periods of three hours over one-week were processed with the current York-PPP engine. The reason behind the 29 selected IGS stations as compared to the 27 stations in Figure 3.1 in the previous work is due to the unavailability of some stations' data on the IGS site at the time of processing, as well as the inclusion of additional stations in the current study. The main aim of this research is to check for the presence of outliers, which distort positioning accuracy in single-epoch solutions. Where most analysis tools would use historical data to obtain even smoother solutions, this work focused on considering each epoch as an independent observation. Therefore, any errors within one epoch would not be averaged out by previous or following measurements.

1648 datasets were processed in total from DOY 015 to 021, 2024. Satellite products which are comprised of precise satellite orbits and clocks generated by GeoForschungsZentrum (GFZ) (Deng et al., 2017) were used, along with a bias file containing both code and phase biases provided by CNES (Laurichesse & Blot, 2016). The latter are compatible with the GFZ products used to generate the PPP-AR solution. The IGS20 ANTEX file was used for the satellite and receiver antenna corrections (Schmid et al., 2016b). Different frequency pseudorange and carrier-phase measurements from the same satellite were weighted equally, but the weighting of the GLONASS measurements was set to half of that of the other constellations due to the unfixed carrier-phase ambiguities of GLONASS caused by its use of Frequency Division Multiple Access (FDMA). The Modified Least-squares AMBiguity Decorrelation Adjustment (MLAMBDA) method was used for ambiguity resolution. By means of this method, the uncombined float ambiguities and covariances of each frequency were used as inputs to the function and converted into fixed ambiguities. Then these fixed ambiguities are used in updating the state terms, with their validation based on a ratio test. Ambiguities were fixed for GPS, Galileo and Beidou because they use the Code Division Multiple Access (CDMA) whilst the ambiguities for GLONASS were not fixed because it uses the Frequency Division Multiple Access (FDMA) as stated earlier. Table 4.1 lists the estimation parameters and strategies that were employed in determining the various states in the DCM model.

Table 4.1: Processing strategy of estimated parameters

Parameters	**Strategy**
Receiver coordinates	Estimated with process noise equivalent to 100 km/h
Receiver reference coordinates	IGS SINEX positions
$\overline{dt_r}$ and $\overline{\partial t_r}$	Estimated as white noise processes
δt_{12}, δt_{13}, δt_{14}, $IFB_{r,3}$ and $IFB_{r,4}$	Estimated as white noise processes
Tropospheric delay	Dry: GMF model and mapping function (Kouba, 2009) Wet: estimated as a random walk process with process noise of 0.05 mm/$\sqrt{h}$
Ionospheric delays	Estimated as white noise processes
Ambiguities	Estimated as constants on each continuous arc
Elevation angle cut-off	7°
Weighting strategy	Elevation dependent weighting: $\sigma = \frac{\sigma_{90}}{a+b\sin el}$ with σ_{90} equal to 0.1 m and 0.001 m for the pseudorange and carrier-phase measurements, respectively, and *el* being the elevation angle. *a* and *b* are determined based on a residual and measurement quality analysis and set to 0.15 and 0.85, respectively.

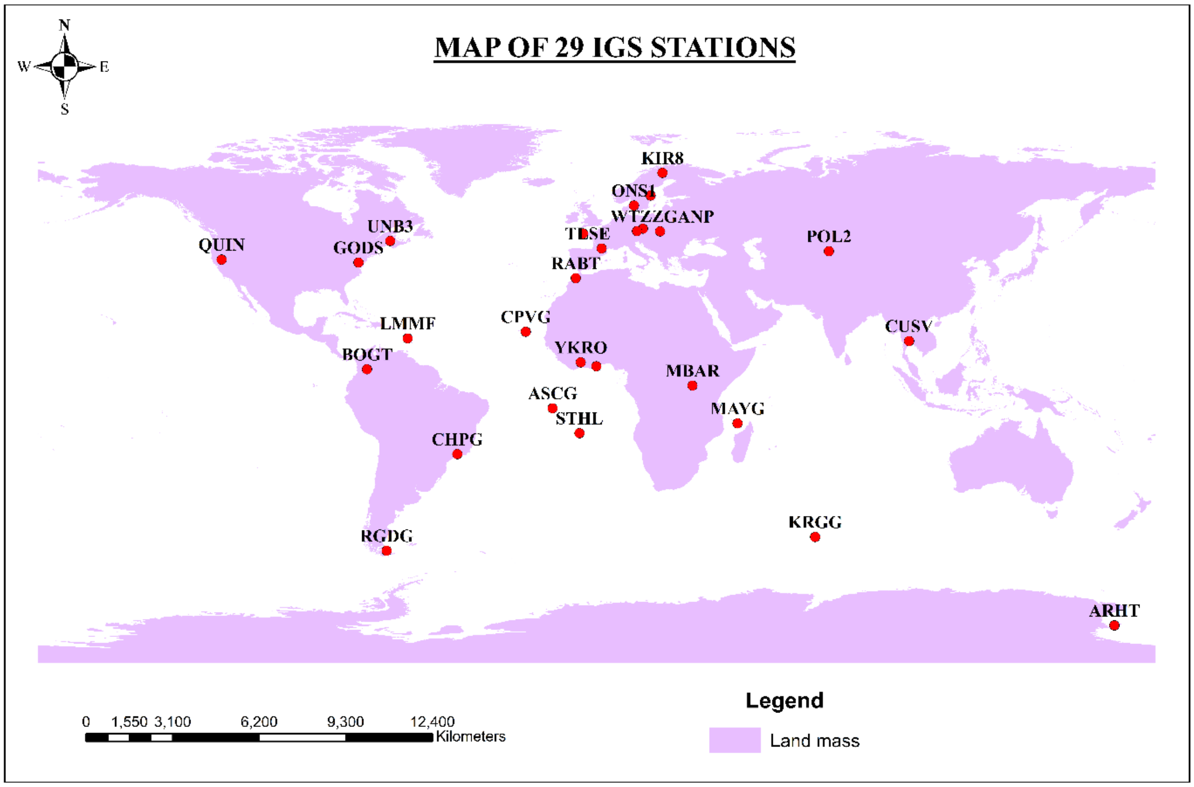

Figure 4.1: Map of IGS stations used for the processing

Table 4.2 shows the frequencies of each constellation used for the processing and Figure 4.2 depicts the percentage of epochs with horizontal errors below 2.5 cm per station in an epoch-by-epoch solutions at the 67th, 95th and 100th percentiles. Each bar represents the percentage of a station's epochs below 2.5 cm horizontal error over one week. The 2.5 cm threshold is chosen to assess whether the percentage of epochs at each station is sufficient to achieve RTK-like performance, as 2.5 cm is used as a benchmark for RTK-level accuracy. On average, across the 29 IGS stations analyzed, the 100th percentile records an average percentage of epochs with horizontal errors below 2.5 cm at 87%, which means that if all the epochs are taken into consideration, a vast majority satisfy the horizontal accuracy criterion. The average percentage of epochs increases slightly in the 95th percentile, to 89%, reflecting removal of 5% outlier epochs. By removing these most extreme errors, more stations meet or exceed that level of accuracy, which reflects the effect of removing outliers on improving station performance. This average percentage increases substantially to 96% in the 67th percentile, meaning that when 33% of the largest errors are removed, almost all the stations are represented by strong performance. This level corresponds closely with a one-sigma threshold, which encompasses data within one standard deviation of the mean.

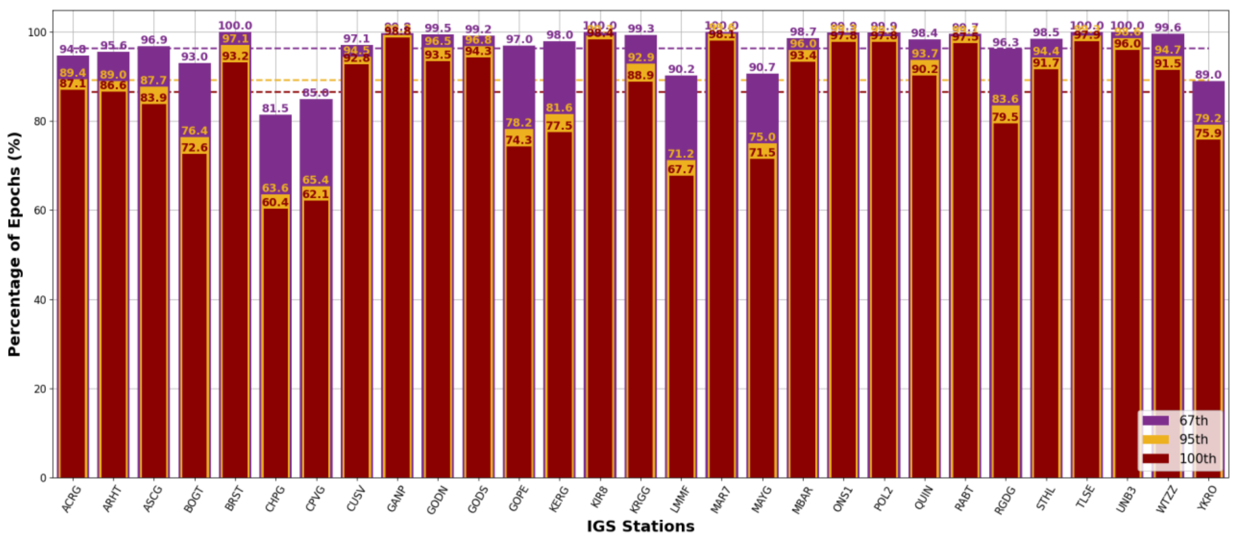

Figure 4.2: Percentage of epochs with horizontal errors below 2.5 cm per station in an epoch-by-epoch solution at the 67th, 95th and 100th percentiles.

Table 4.2: Selected frequencies for each constellation used for the processing

Constellations	Selected frequencies
GPS	L1 (1575.42 MHz), L2 (1227.60 MHz) and L5 (1176.45 MHz)
GLONASS	G1 (1602 + $\frac{9}{16}$k MHz) and G2 (1246 + $\frac{7}{16}$k MHz)
Galileo	E1 (1575.42 MHz), E5b (1207.140 MHz), E5a (1176.45 MHz) and E6 (1278.75 MHz)
BeiDou-2	B1-2 (1561.098 MHz), B2b (1207.140 MHz) and B3 (1268.52 MHz)
BeiDou-3	B1C (1575.42 MHz), B2a (1176.45 MHz), B2b (1207.140 MHz) and B3 (1268.52 MHz)

4.1.1 Analysis of Station Performance in Geodetic MCMF PPP-AR Epoch-by-Epoch Solution

To evaluate the impact of outliers in MCMF PPP-AR solutions, an analysis of 29 IGS stations was conducted based on horizontal accuracy at three percentile levels: 100th (all epochs), 95th (2-sigma), and 67th (1-sigma). Table 4.3 summarizes the station performance across these percentiles.

4.1.1.1 Overall Station Performance

From Table 4.3, high-performing stations such as GANP, KIR8, TLSE, and BRST exhibit consistently strong results, with over 93% of epochs achieving the 2.5 cm accuracy threshold even at the 100th percentile. These stations show minimal impact from outliers, as seen in their small performance improvements across percentiles. Conversely, CHPG, CPVG, LMMF, and MAYG record significantly lower percentages, particularly at the 100th percentile, suggesting higher positioning errors and outlier effects. For instance, CHPG achieves only 60.4% at the 100th percentile, improving to 81.5% at the 67th percentile, indicating the presence of large deviations in its solution.

Table 4.3: Percentage of epochs below 2.5 cm for selected stations based on high-performing to low-performing across 67th, 95th and 100th percentiles

Station	**Percentile (%)**			**Improvement**
	67	**95**	**100**	**(100% → 67%)**
GANP	99.8	99.34	98.8	+1.0
KIR8	100	99.3	98.4	+1.6
TLSE	100	99.3	97.9	+2.1
BRST	100	97.1	93.2	+6.8
BOGT	93.0	76.4	72.6	+20.4
MAYG	90.7	75.0	71.5	+19.2
LMMF	90.2	71.2	67.7	+22.5
CPVG	85.0	65.4	62.1	+22.9
CHPG	81.5	63.6	60.4	+21.1

4.1.1.2 Impact of Removing Outliers

The effect of outlier removal is evident in the percentage increases from the 100th to 67th percentile. BOGT and CPVG, for example, show substantial improvements of 20.4% and 22.9%, respectively. Such large variations suggest that outlier contamination is a major factor affecting their positioning accuracy. In contrast, the minimal changes in GANP, KIR8, and TLSE indicate that their solutions are already robust, with fewer large deviations affecting their performance. BRST, although performing well, shows a moderate improvement of 6.8%, suggesting some sensitivity to outliers.

4.1.1.3 Robustness Across Percentiles

Robust stations such as GANP, TLSE, and KIR8 demonstrate minimal variation across percentiles, confirming their high-quality solutions with limited sensitivity to outliers. On the other hand, stations like CHPG, CPVG, and LMMF, which improve by over 20%, indicate a higher degree of error variability, highlighting the importance of outlier detection and mitigation in improving PPP-AR accuracy.

4.1.2 Investigation of Station-By-Station Variations

To achieve robust of the multi-frequency multi-constellation of epoch-by-epoch results as shown in Figure 4.2, there is a need to investigate and understand what the cause(s) of these station-by-station variations are. To do so, three stations have been selected for further investigation. The selection is based on the percentage of horizontal errors below 2.5 cm. Station KIR8 as a good performing station, station ASCG as an average performing station and station CHPG as a bad performing station.

Figure 4.3 presents the time series of float and fixed solutions for KIR8, ASCG and CHPG on DOY 015 in 2024. On top is KIR8 (good station), ASCG (average station) and CHPG (bad station). For the good performing station, the fixed solution performs very well, with 99.1% of epochs achieving horizontal errors below 2.5 cm. This high percentage indicates very effective ambiguity resolution at this station, leading to minimal discrepancies throughout the fixed solution. The average performing station shows a fixed solution that varies significantly more over time compared to good performing station. Whereas 82.7% of its epochs have horizontal errors below 2.5 cm, it has periodic divergence, an indication of problems in ambiguity resolution that prevent the fixed solution from stabilizing sometimes. Finally, the bad performing station has significant challenges in its fixed solution: only 61.5% of epochs achieve horizontal errors below 2.5 cm. It is mainly because the station cannot consistently resolve carrier-phase ambiguities.

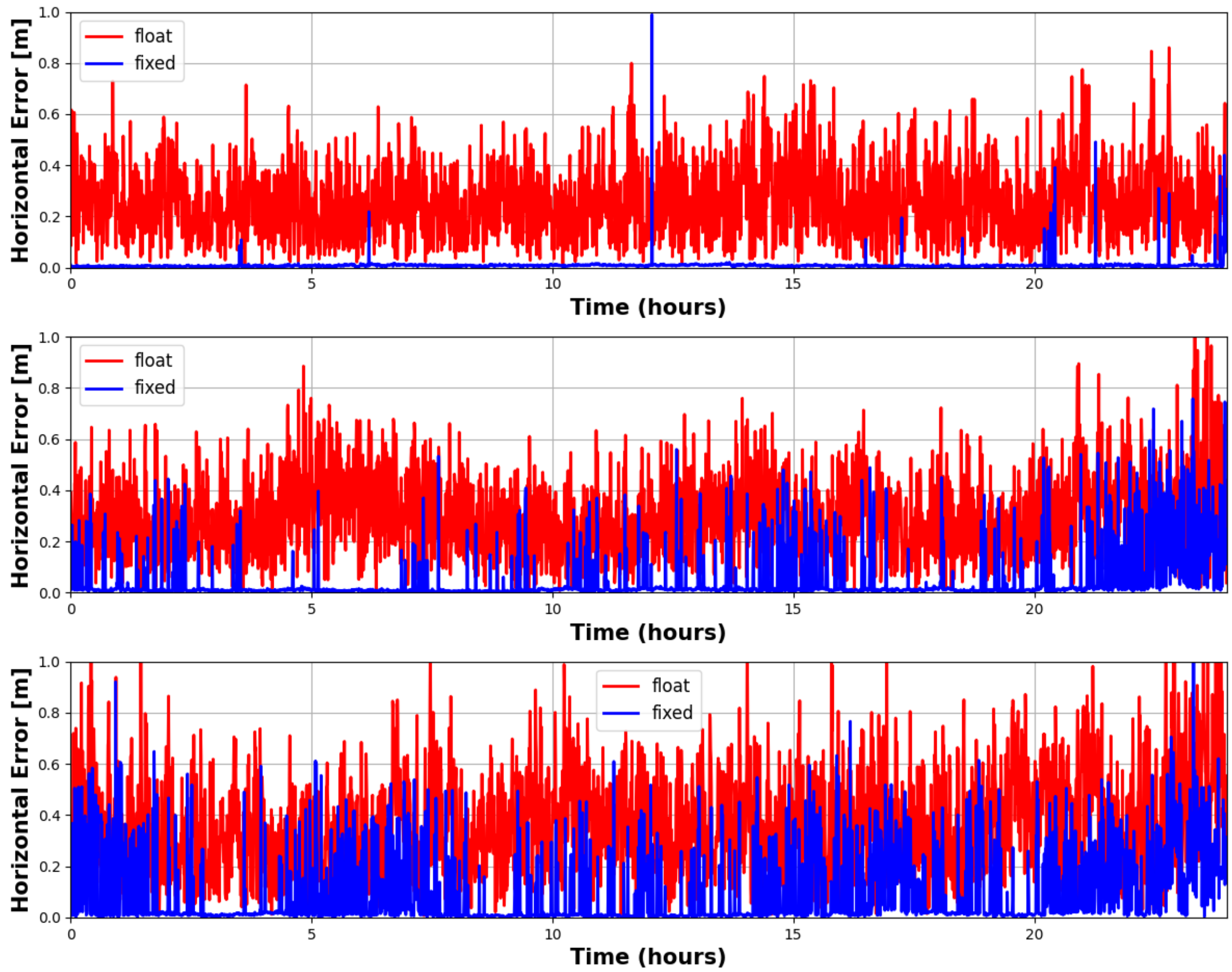

Figure 4.3: Time series of float and fixed solutions for KIR8, ASCG and CHPG on DOY 015 in 2024. Top: KIR8 (good station); Middle: ASCG (average station); Bottom: CHPG (bad station).

Figure 4.4 contains the histogram and cumulative density function (CDF) plots of horizontal errors for KIR8, ASCG and CHPG on DOY 015 in 2024. The RTK-like threshold of 2.5 cm is shown as a red dashed line to aid in distinguishing the horizontal errors below the threshold. The importance of the histogram and the CDF is to identify the frequency and impact of the outliers at various stations.

The histogram of the good station has a narrow spread and symmetric shape with most of the values concentrated in the lower horizontal error ranges. There are very few outliers, indicating consistency in performance for most epochs. It is seen that the CDF plot for the good station increases steeply and reaches a value close to 1 at a much smaller rms value, reflecting that almost all horizontal errors are less than 2.5 cm since 99.1% of the epochs are below this threshold. This indicates an excellent error control as the tail of the CDF ends at a relatively low value of error. From the above pattern, it is deduced that the fixed solution at good station is highly reliable, and the outliers would not affect the final positioning results. The histogram of average station is wider than the good station, with larger outliers but still shows a relatively symmetric distribution around the central values. While the CDF plot for the average station is increasing in a steady but more gradual manner compared to the good station, it reflects that 82.7% of epochs fall below 2.5 cm. The CDF does have some fluctuations, which indicates that there might be some epochs with larger errors. Also, the tail of the CDF plot is somewhat extended, and thus the outliers also affect this station's overall performance. The wider distribution and less steep CDF indicate that ambiguity resolution is sometimes hindered by either environmental factors or poor satellite geometry, as multipath effects, atmospheric delays, and weak satellite geometry introduce errors that make it difficult to resolve ambiguities reliably and preventing the station from staying within a high level of accuracy. The histogram for bad station shows a highly skewed distribution, with a significant proportion of the data falling into larger error categories. The bad station has the largest numbers of outliers reflecting its poor performance, where only 61.5% of epochs achieved horizontal errors below 2.5 cm. The CDF plot rises much more gradually with noticeable fluctuations. Additionally, its tail is much longer, reflecting the persistence of large errors. Outliers are dominant in the station's results, seriously affecting the ability of the station to maintain accurate positioning. As can be seen from the skewed histogram and extended tail of the CDF, ambiguity resolution for the bad station faces severe challenges which could potentially be because of either multipath interference, poor satellite geometry, or other causes, leading to a degraded fixed solution. Other statistics such as 67th and 95th percentiles also help to detect outliers in Figure 4.4. As Figure 4.4 moves from the good station to the bad station, the 67th and 95th percentile points continually shift to the right. This indicates a pattern confirming that the highest concentration of outlier's impact the bad station the most and affect its overall performance more when compared to the good and average stations.

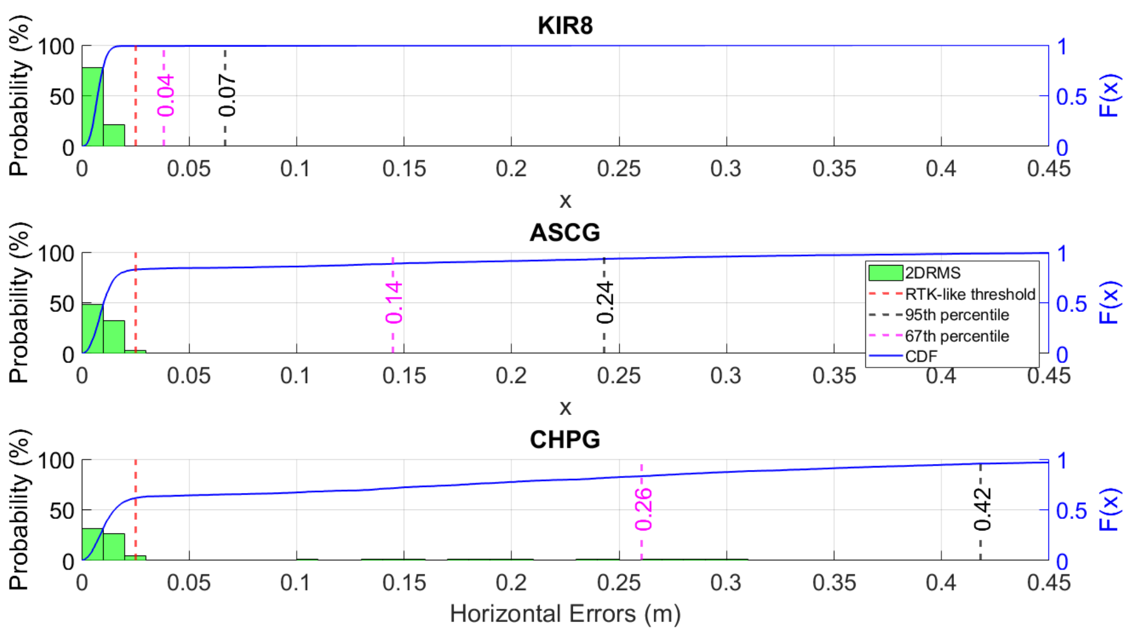

Figure 4.4: Histogram and CDF plots of fixed horizontal errors for KIR8, ASCG and CHPG on DOY 015 in 2024. Top: KIR8 (good station); Middle: ASCG (average station); Bottom: CHPG (bad station).

4.2 Causes of Position Outliers

This section focuses on identification of the contributing factors resulting in the occurrence of outliers within Geodetic MCMF PPP-AR epoch-by-epoch solutions. Referring to the station analysis presented in the previous section, it can be observed that the position outliers can significantly impact the accuracy of positioning solutions. Outliers occur when some condition cause individual measurement errors or anomalies that deviate significantly from the expected or true values of the positioning solution. Such conditions change based on several factors. Among them are the signal environment of the station, satellite geometry, and quality of measurement. Understanding the root causes is important for the development of robustness and reliability in these solutions for precise applications, including geodetic positioning. In this section, main contributing factors of the outliers, including signal strength, pseudorange multipath and noise, satellite visibility and geometry, and the number of measurements and measurement redundancy, are discussed. All of them are critical in defining the positioning solution and are closely analyzed for their effect on the solution. These factors can be identified and mitigated to reduce such outliers with a view to increasing the general performance of the geodetic MCMF PPP-AR solution at various stations.

4.2.1 Signal Strength

Signal strength is a critical factor in terms of the accuracy and reliability of GNSS measurement, particularly in PPP. In an epoch-by-epoch PPP solution, the weak signal strength increases the possibility of outliers that can deteriorate positioning accuracy by a substantial amount. The signal strength, normally quantified by the signal-to-noise ratio (SNR), often reflects the quality of the satellite signal that is being received. It is important to note that high values of SNR correspond to strong signals, while the low SNR values generally refer to weaker, noisier signals, which are more susceptible to external environmental interference, multipath effects, and other sources of error. Signal strength is one of the most important factors directly affecting the quality of both pseudorange and carrier-phase measurements, the two core components of PPP solutions.

Various studies have pointed out the impact of signal strength on GNSS performance. Parkinson and Spilker (1996) highlights that with high SNR, the precision in both pseudorange and carrier-phase measurement is improved, hence a reduced chance of outliers. Similarly, Misra and Enge (2011) indicate that weak signals imply increased noise in the GNSS measurements, a condition that negatively impacts the resolution of carrier-phase ambiguities. These weak signals result in larger positioning errors, which manifest as outliers in the PPP solution. They further note that degradation in signal strength due to an urban environment or multipath effects can produce errors well more than the typical thresholds employed in GNSS. van Diggelen (2009) insists that strong signal strength is needed to ensure good positioning and that weak signals are easily subject to multipath interference, generating errors that the PPP solution may not fully correct and thus results in outliers. In addition, research such as that by Wanninger and Wallstab-Freitag (2007) shows that weak signals, especially those from satellites with low elevation angles, increase ionospheric and tropospheric errors, further reducing positioning accuracy.

4.2.2 Pseudorange Multipath and Pseudorange Noise

PPP, especially real-time and epoch-by-epoch solutions, is highly affected by pseudorange multipath and noise, often causing outliers that degrade position accuracy. Multipath occurs when the signals, before reaching the receiver, reflects off the surrounding objects, e.g., buildings, trees, or ground. The reflected rays add additional delay to the pseudorange measurement thus creating inaccuracies in the positioning solution. In PPP, multipath more strongly affects the pseudorange-measurements than the carrier-phase measurements. Given that PPP is based on very precise signal measurements, multipath errors in pseudorange can result in significant deviations, especially when satellite visibility is poor, as in urban canyons. Gao and Chen (2004) pointed out pseudorange multipath may introduce biases up to several metres, which is a critical factor in introducing outliers into GNSS positioning solutions, when ambiguity resolution is involved in PPP. Furthermore, the multipath errors are highly dependent on the site and change with the geometry of the surrounding environment, satellite elevation angles, and quality of the receiver antenna (Misra & Enge, 2011). This variability makes their complete avoidance difficult by conventional algorithms; hence, outliers persist in epoch-by-epoch processing.

Hofmann-Wellenhof et al. (2008) and Leick et al. (2015) estimated the pseudorange multipath observable as a linear combination of the pseudorange and carrier-phase measurements as demonstrated in equations (4.1) and (4.2). Conventionally, the multipath and noise of the carrier-phase measurements are relatively smaller than the pseudorange measurements, so they are neglected. The pseudorange multipath observables on two frequencies f_i and f_j can be estimated as:

$$mp_i = P_i - \left(1 + \frac{2}{\alpha-1}\right) L_i + \left(\frac{2}{\alpha-1}\right) L_j \tag{4.1}$$

$$mp_j = P_j - \left(\frac{2\alpha}{\alpha-1}\right) L_i + \left(\frac{2\alpha}{\alpha-1} - 1\right) L_j \tag{4.2}$$

Where, mp_i is the pseudorange multipath observable on the f_i frequency, mp_j is the pseudorange multipath observable on the f_j frequency, P_i and L_i are the pseudorange and carrier-phase measurements in metres on the f_i frequency respectively, P_j and L_j are the pseudorange and carrier-phase measurements on the f_j frequency respectively, and $\alpha = (\frac{f_i}{f_j})^2$. When during a period, T_m, the multipath and noise have a zero mean, the hardware delays are constant, and no cycle-slips occur, the multipath and noise can be rewritten from equations 4.1 and 4.2 as

$$MP_i = mp_i - mp_{iT_m} \tag{4.3}$$

$$MP_j = mp_j - mp_{jT_m} \tag{4.4}$$

Where, mp_{iT_m} and mp_{jT_m} are the average of mp_i and mp_j respectively, over the period T_m, and MP_i and MP_j are the final pseudorange multipath observables on the f_i and f_j frequencies respectively.

Pseudorange noise is caused by several factors including the limitation of receiver hardware, atmospheric conditions-ionospheric delay and tropospheric delay-and interference of a signal. Unlike multipath, which has more systematic trends, pseudorange noise is more stochastic in nature; hence, its value can change unpredictably from one epoch to another. For the centimetre accuracy PPP solution, the effect of pseudorange noise randomly drives deviations from the fixed solution. The noise may have certain epochs fail in ambiguity resolution and thus introduce large position errors that can be the potential outliers for the PPP solution. van Bree and Tiberius (2012) indicated that pseudorange noise might be exacerbated by factors such as poor SNR, which takes place under conditions of weak satellite signals-for example, under dense foliage or obstructed urban areas.

Various mitigation strategies have been put forward towards the minimization of pseudorange multipath and noise. These include, advanced signal processing techniques, improved antenna designs, and making use of combined GNSS constellations in order to increase the redundancy of measurements. Gao and Chen (2004) stated that the multipath estimation delay lock loops, which, while effective in error reduction, still face challenges in harsh environments with dominant reflections. The signal designs of GNSS modernization, for example, Galileo-and modernized GPS signals (L5) increase robustness to multipath interference. However, even with these signals, outliers caused by noise and multipath will not be fully avoided (Montenbruck et al., 2018b). Despite these advances, pseudorange multipath and pseudorange noise remain substantial sources of outliers in epoch-by-epoch PPP processing. The irregularity and unpredictability of these errors indicate the need for more robust outlier detection and mitigation techniques in future PPP algorithms if precise positioning is to be maintained.

4.2.3 Satellite Visibility and Geometry

In PPP, satellite visibility and geometry play a critical role in determining the accuracy and reliability of the positioning solution, particularly in epoch-by-epoch analysis. Poor satellite visibility and unfavorable satellite geometry are the major factors that originate outliers and lead to poor performance in PPP solutions.

Satellite visibility refers to the number and quality of satellites observed by a GNSS receiver. Limited visibility due to obstructive elements such as buildings, trees, and mountains, among others, indicates fewer satellite signals available and increases DOP, which also introduce outliers in the positioning solution. When there are fewer satellites available, the geometry becomes weaker and the positioning error increases, particularly in urban areas or forest conditions where the occurrence of multipath and obstruction is more likely. Bisnath and Gao (2009) emphasized that enough visible satellites, well spread in the sky, ensure a robust solution with reduced outliers. Poor visibility conditions significantly deteriorate the PPP solution due to substantial difficulties of the receiver to maintain consistent signal lock and to resolve ambiguities with good accuracy.

Satellite geometry is the spatial distribution of satellites relative to the receiver. The position dilution of precision (PDOP) is a measure which characterizes the effect of satellite geometry on the precision of the PPP solution. A low value of PDOP implies good satellite geometry, that is, the satellites are well distributed in the sky and normally translates to more precise position fixes. On the other hand, high PDOP values, which are usually caused by satellites clustered in one part of the sky or at low elevation angles, result in positioning that is less precise and increases the frequency of outliers in epoch-by-epoch solutions. Teunissen and Montenbruck (2017) indicated in their research that bad satellite geometry can seriously impair ambiguity resolution, which is very critical to the fixed solution in PPP. Poor positioning of satellites reduces the resolving capability of the carrier-phase ambiguity and leads to outliers of the position estimates. For instance, poor positioning could refer to satellites that are near or on the horizon, which might usually provide weaker signals, increased multipath, and longer signal propagation through the atmosphere, all contributing to reduced accuracy and more outliers.

According to Rizos et al. (2012), introduction of more GNSS constellations increases the redundancy and diversity of satellite signals, a fact that together reduces the impact of poor geometries on positioning errors. By making use of multiple GNSS systems, receivers can keep stronger geometries even under challenging conditions in ways that help reduce the occurrence of outliers in epoch-by-epoch PPP solutions.

4.2.4 Number of Measurements and Measurement Redundancy

The availability of measurements is a basic aspect of any PPP solution. The number of visible satellites contributes to the quality of position estimation, since any additional satellite provides independent measurements that might help in resolving ambiguities and correcting errors. The small number of measurements, normally due to problems in satellite visibility or blockages of their signals, reduces information available for the positioning algorithm, thereby increasing risks of outliers within the solution. With fewer measurements, the PPP solution is more prone to random noise, signal degradation, and multipath effects, which may result in less precise position estimates with possible outliers. As Bisnath and Gao (2009) stated, increasing the number of measurements will enhance the reliability of the solution due to the added redundancy that helps in filtering out erroneous data and achieves stability in positioning accuracy.

Measurement redundancy occurs when more observations than the minimum required to determine a position are available. In fact, such redundancy constitutes an important feature of PPP since it will allow the system to detect and filter out wrong data, including outliers caused either by multipath or poor satellite geometry. Lack of redundancy increases the possibility that flawed data will affect the final solution when each individual measurement is compromised. Rizos et al. (2012) emphasized that multi-constellation GNSS increases redundancy in measurements for better rejection or down-weighting of the erroneous signals. Because the PPP algorithm makes use of to multiple satellite constellations, it can support the accuracy and stability of the position better than would occur with only one constellation in situations where some of the signals are subject to multipath or noise.

For epoch-by-epoch PPP solutions, where each position estimate is computed independently, the number of measurements and redundancy becomes even more critical. Unlike sequential processing, where estimates over time can be smoothed, it requires that any one position be calculated based on available data at that instant. In situations with insufficient measurements or redundancy, the errors introduced by random noise, multipath, or poor satellite geometry are more likely to manifest as outliers in the solution. Odijk et al. (2016) highlights that increased measurement redundancy will especially benefit real-time PPP applications due to its stabilizing effect on solutions and ability to help to reduce the impact of momentary measurement problems. Without sufficient measurements, each epoch is then subject to random errors and overall significant variations in position accuracy from one instant to another.

5 Correlation Analysis and Principal Component Analysis of Data Quality Indicators in PPP Solutions

This chapter critically examines the impact of various factors contributing to measurement quality on the accuracy and reliability of PPP solutions, with a focus on identifying the underlying causes of outliers. In PPP, discrepancies from nominal positioning outcomes occur due to several error sources, e.g., signal strength variations, pseudorange multipath, poor satellite geometry, and insufficient measurement redundancy. It is important to understand these impacts for enhancing positioning performance, especially for real-time processing applications.

To provide a systematic analysis, this chapter begins by introducing commonly used measurement quality metrics by GNSS receiver manufacturers. The metrics include the carrier-to-noise density ratio (C/N_0), signal strength indicators, and multipath observables, which are important variables for quantifying the reliability of measurements (Teunissen & Montenbruck, 2017). These metrics are implemented by manufacturers to exclude signals with low quality and enhance overall positioning accuracy (Misra & Enge, 2011). Moreover, developers normally use these metrics in a form of weighting strategies to mitigate the impact of low-quality observations on positioning solutions. These strategies often rely on a combination of elevation-angle-dependent models, stochastic weighting based on measurement noise characteristics, and adaptive filtering techniques (Kouba & Héroux, 2001). Proper weighting is essential as it determines the influence of each observation on the final position estimate, and various algorithms have been developed to optimize this process based on real-time signal conditions (Zumberge et al., 1997). Building upon this foundation, the chapter presents a detailed data correlation analysis to investigate the relationships between different potential sources of measurement errors and their influence on both float and fixed PPP solutions. Key factors examined include variations in signal strength, pseudorange multipath effects, and measurement noise. Identifying the relationships among these factors provides valuable insights into the patterns of data degradation and performance deterioration in PPP solutions. In addition to correlation analysis, PCA is employed to reduce dataset dimensionality, enabling the extraction of key data quality indicators that significantly contribute to position outliers. By transforming the dataset into a set of uncorrelated principal components, PCA facilitates a more interpretable representation of the dominant error sources affecting PPP performance. This approach aids in distinguishing the most influential metrics and provides a systematic way to assess their impact on positioning accuracy.

The results from both correlation and principal component analyses collectively offer a comprehensive understanding of how different error sources interact and contribute to positioning anomalies in PPP. By identifying the primary contributors to measurement degradation, this chapter provides practical recommendations for mitigating the frequency and magnitude of outliers. These findings serve as a foundation for refining data weighting strategies and enhancing PPP solution robustness, particularly in real-time applications where minimizing positioning errors is critical.

5.1 Correlation Analysis of Data Quality Indicators

This section examines the correlation between various factors contributing to outliers in PPP solutions. The analysis considers signal strength, pseudorange multipath, noise, satellite visibility, geometry, and measurement redundancy to identify key influences on both float and fixed PPP accuracy. By understanding these relationships, this analysis provides insights into why certain stations perform better than others and how to enhance the reliability and precision of PPP applications.

5.1.1 Signal Strength

From Table 5.1, KIR8 shows high SNR values in both frequencies, with the maximum of 52.5 dBHz and 56.6 dBHz in the first and second frequencies respectively. The average value is also comparably high, which suggest strong, more reliable signals for both frequencies. The SNR values in ASCG are a bit lower than KIR8. The difference between the minimum and maximum SNR is larger, which indicates variability in its signal strength that might provide less reliable results in positioning. The SNR values in CHPG are low, especially in the second frequency, reaching a minimum of only 10.9 dbHz and an average of 42.7 dbHz. The lower the quality of a signal, with larger differences between maximum and minimum values, the higher the chances of outliers due to weak signals and more noise.

Table 5.1: Statistics of SNR values on first and second frequencies for all constellations for KIR8, ASCG and CHPG on DOY 015, 2024

Stations	**SNR1 (dBHz)**			**SNR2 (dBHz)**		
	Min	**Max**	**Average**	**Min**	**Max**	**Average**
KIR8 (Good)	29.2	52.5	46.3	13.9	56.6	43.7
ASCG (Average)	25.5	55.6	44.6	10.9	57.1	42.2
CHPG (Bad)	24.8	56.3	45.3	10.9	57.1	42.7

Table 5.2 illustrates the frequency and percentage of SNR values below 35 dBHz threshold on first and second frequencies for KIR8, ASCG and CHPG on DOY 015, 2024. KIR8 shows fewer occurrences of samples falling below the 35 dBHz threshold. The lower frequency of poor signal occurrences correlates with its better PPP performance in the fixed solution especially. In contrast, CHPG shows a higher frequency of samples below the threshold, especially at the first frequency. This higher frequency results in poor signal quality and directly affects its ability to achieve optimal float and fixed PPP solutions. Figure 5.1 which shows the time series of SNR on top and positional accuracy on the bottom for the stations KIR8, ASCG, and CHPG (for GPS satellites on DOY 015, 2024), revealing important characteristics about the performance of the GNSS signals under different conditions. The figure shows that the SNR values are more dispersed when the satellite is at a lower elevation. This scenario is expected, since the lower elevation satellites are more prone to signal attenuation and multipath due to interference by the Earth's surface or buildings and other reflective objects. At low elevations, the signal must travel through a longer path in the Earth's atmosphere and is therefore more prone to interference, noise, and other degradations, which decrease the SNR. The trend of signal degradation at lower elevations is more pronounced in CHPG. Meanwhile, KIR8, as the best performing station, is probably able to maintain a better SNR even at lower elevations due to maybe its antenna design and placement of the receiver, which gives way to higher positional accuracy and more stable PPP solutions.

This correlation between the low-elevation satellite signals and degraded SNR explains part of the difficulty faced by CHPG, with more issues related to a higher frequency of poor SNR values. In fact, the positional accuracy (float and fixed solutions) across the lower half of the figure 5.1 indicates increased error at times of lower SNR and hence also support this conclusion that signal strength, at low elevation, is one of the key factors in the overall performance of PPP at each station.

Table 5.2: Number and percentage of SNR values below 35 dBHz threshold on first and second frequencies for all constellations for KIR8, ASCG and CHPG on DOY 015, 2024

Stations		**SNR1**		**SNR2**	
	Total Samples	**Frequency**	**Percentage (%)**	**Frequency**	**Percentage (%)**
KIR8 (Good)	101719	397	0.39	12319	12.11
ASCG (Average)	86357	2298	2.66	15016	17.39
CHPG (Bad)	80054	2873	3.59	11703	14.62

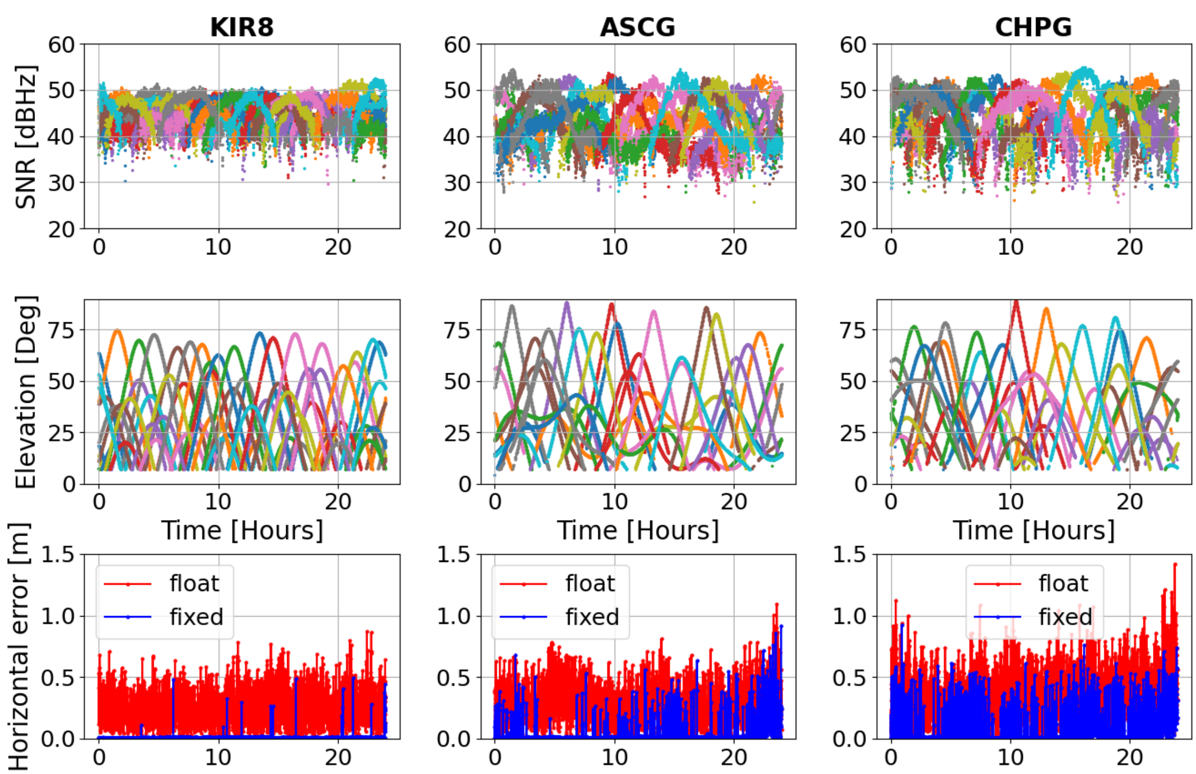

Figure 5.1: Time series of Top: Signal-to-Noise-Ratio; Middle: Elevation; Bottom: Positional accuracy for KIR8, ASCG and CHPG for GPS satellites on DOY 015, 2024

5.1.2 Pseudorange Multipath and Pseudorange Noise

Pseudorange multipath and pseudorange noise are two critical factors affecting the accuracy of PPP solutions. As explained previously, multipath is due to the reflections of the signal from objects surrounding the receiver to distort the true path of the signal and, hence, give rise to erroneous measurements. Pseudorange noise comprises the random errors due to receiver electronics and disturbances in the atmosphere that all contribute to worsening the standard positioning errors when observing satellite signals at low elevation angles. Figures 5.3 and 5.4 show the detailed pseudorange multipath and pseudorange noise errors of GPS satellites for KIR8, ASCG, and CHPG using the first and second frequencies, respectively. The pseudorange multipath observables were generated from equations 4.1 to 4.4. These figures illustrate how satellite elevation, pseudorange multipath, and horizontal positioning accuracy are interconnected with each other, especially for the float and fixed solution differences.

Figure 5.2 shows the pseudorange multipath variation as a function of both azimuth and elevation of GPS satellites for stations KIR8, ASCG, and CHPG. The top row corresponds to multipath for the first frequency while the bottom row corresponds to the second frequency. Overall, the stations have higher multipath values mostly below the elevation angle of 30°, where signals are prone to reflection and interference, whereas the effect of multipath is considerably reduced at higher elevations due to diminished reflection effects. The azimuthal distribution shows environmental differences among the stations. KIR8 has very little multipath, indicating an open environment with few reflectors. On the other hand, ASCG has heavy multipath clustering at low elevations for a range of azimuths, which indicates substantial obstructions or reflectors in its environment. CHPG has an intermediate pattern with moderate multipath occurrences and less clustering than ASCG, indicating a partially obstructed environment.

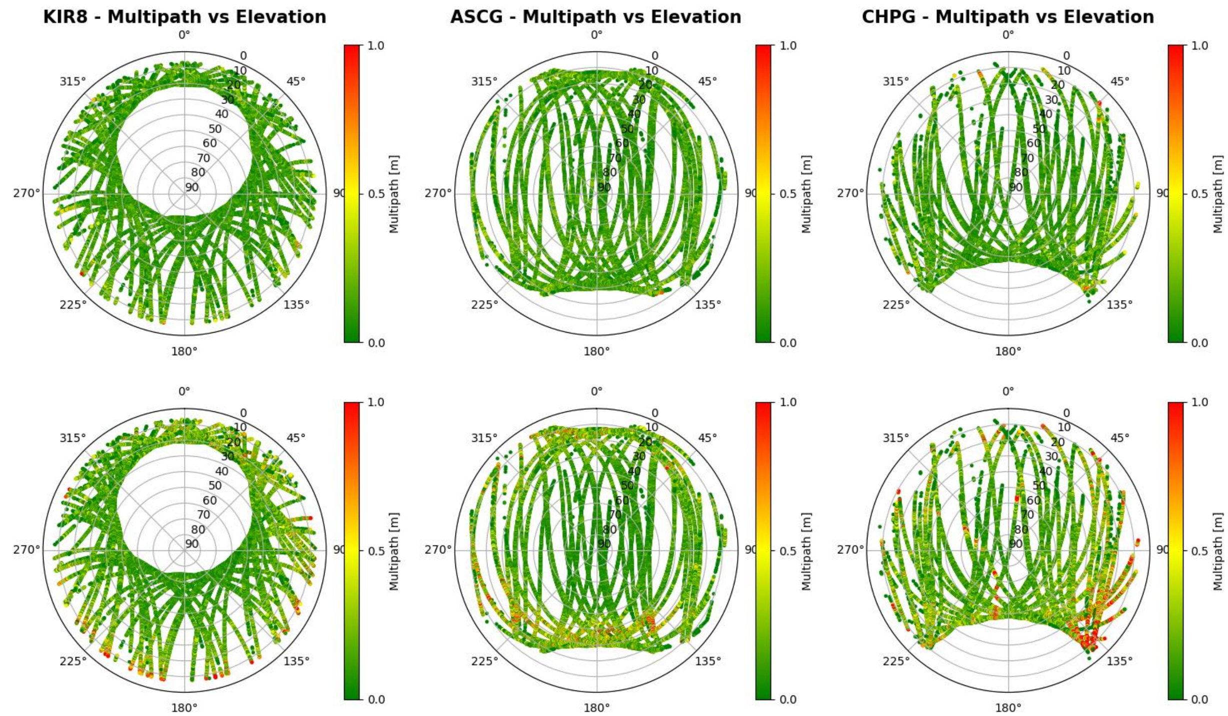

Figure 5.2: Polar plots showing the distribution of pseudorange multipath as a function of azimuth and elevation of GPS satellites for KIR8, ASCG and CHPG on Top: First frequency; Bottom: Second frequency.

A comparison of frequencies reveals that the second frequency has consistently higher multipath values compared to first frequency at all stations, mostly at lower elevations. This account is because the second frequency has a lower frequency and thus is more subject to reflection and diffraction. ASCG shows the most dramatic multipath on both frequencies, while KIR8 remains the least affected, with CHPG showing moderate impacts. The results highlight the influence of station environments and signal frequencies on multipath phenomena. Unobstructed environments, like KIR8, experience little interference; on the other hand, obstructed ones, as represented by ASCG, significantly amplify multipath effects, especially for lower-frequency signals. This analysis underlines the critical role of site selection and frequency considerations in alleviating multipath issues within GNSS applications.

The bottom row in both Figure 5.3 illustrates the horizontal errors for the float and fixed solutions. The float solution is very sensitive to code multipath errors, with values often spiking up to and beyond 1 metre, especially at low elevations, when the amount of multipath may be high. However, the fixed solution successfully corrects these errors, maintaining positional accuracy well within 0.2 metres during most of the observation period at KIR8. That solution reflects the capability of ambiguity resolution to maintain high precision even when conditions are potentially challenging, for instance, with multipath from low-elevation satellites. This increases the need of multipath mitigation to enhance the float solution's reliability, making it more conducive to ambiguity resolution.

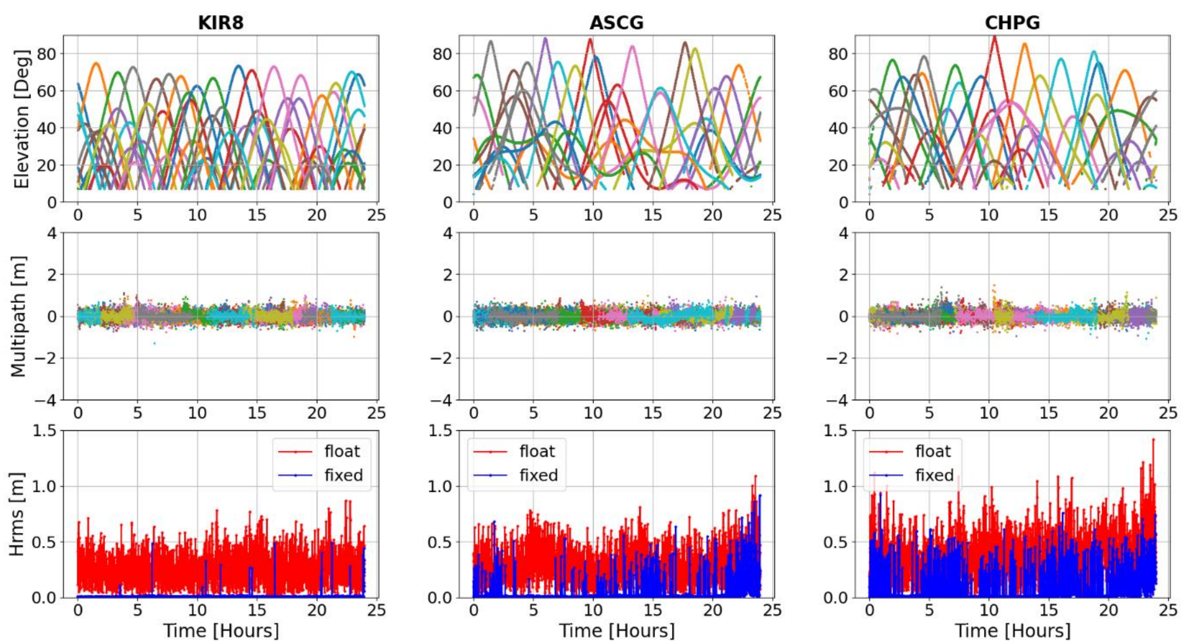

Figure 5.3: Top: Time series of elevation; Middle: Pseudorange multipath; Bottom: Horizontal positional accuracy on the first frequency of GPS satellites for KIR8, ASCG and CHPG on DOY 015, 2024.

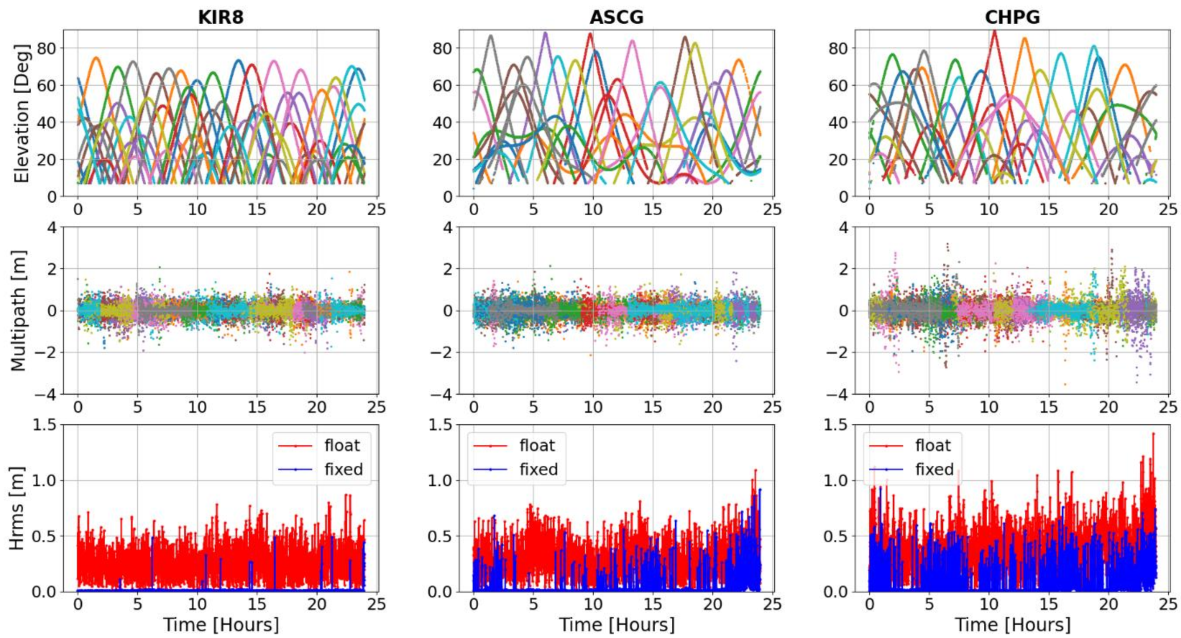

Figure 5.4: Top: Time series of elevation; Middle: Pseudorange multipath; Bottom: Horizontal positional accuracy on the second frequency of GPS satellites for KIR8, ASCG and CHPG on DOY 015, 2024

5.1.3 Satellite Visibility and Geometry

Satellite visibility is the number of GNSS satellites that are in the line of sight of a receiver at a given time. The more satellites a receiver can see, the better the potential for accurate positioning. Satellite geometry on the other hand is the spatial arrangement of the satellites relative to the receiving antenna. The quality of the satellite geometry is often quantified using Dilution of Precision (DOP). Table 5.3 presents the average number of tracked satellites and PDOP values for stations KIR8, ASCG, and CHPG over a 24-hour period on DOY 015, 2024. The data shows that KIR8 tracked the highest number of satellites with the lowest PDOP, indicating superior satellite geometry and measurement redundancy. ASCG and CHPG followed with slightly lower satellite counts and higher PDOP values.

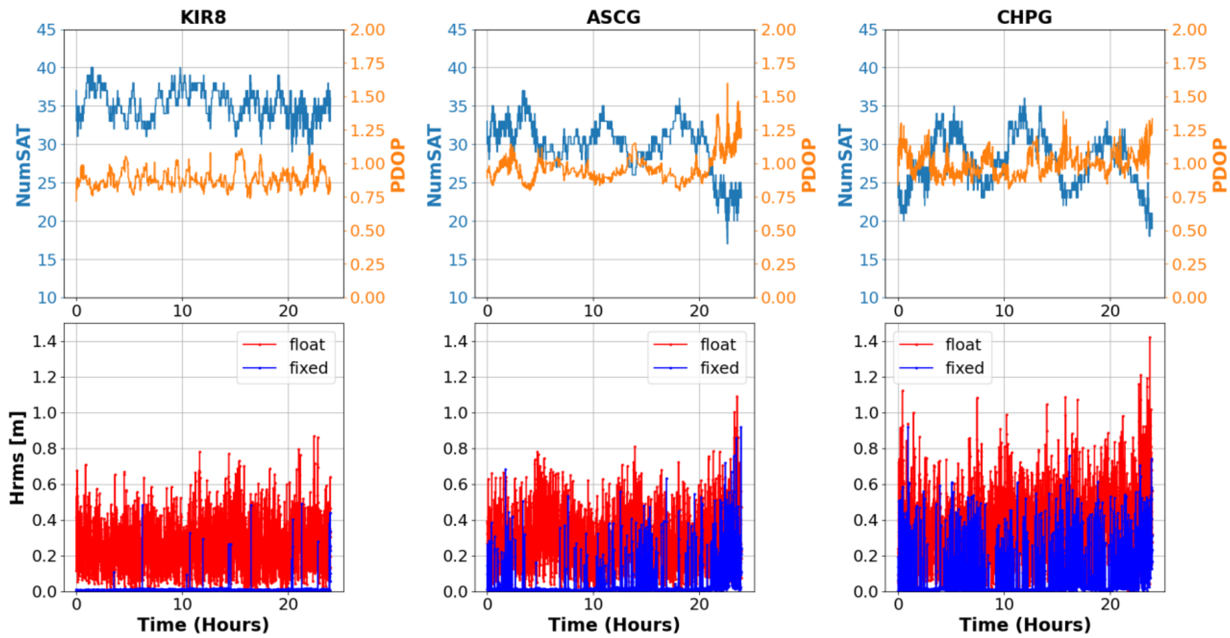

Figure 5.5: Top: Time series of number of satellites and PDOP; Bottom: Horizontal positioning accuracy for stations KIR8, ASCG and CHPG for DOY 015, 2024.

Table 5.3: Average satellite visibility and PDOP for stations KIR8, ASCG and CHPG for DOY 015, 2024

Station	Average Satellites Tracked	Average PDOP
KIR8	35	0.88
ASCG	30	0.96
CHPG	28	1.00

The mean number of tracked satellites is significantly different among the three stations, mainly due to the geographic locations and the GNSS orbital geometry. The high-latitude station, KIR8 (67.87° N), has the largest number of tracked satellites as depicted in Table 5.3, owing to the overlapping coverage of the constellations such as GLONASS and Galileo that work well for polar regions where fewer satellites are overhead. ASCG (-7.92° S) near the equator has the best view of the relatively fewer satellites compared to station KIR8 benefiting from dense global coverage, but constrained by local obstructions and atmospheric conditions. CHPG (-22.68° S), in the mid-latitudes, has a view of the fewest satellites (28), most likely because of the decreased visibility of regional constellations and fewer satellites directly overhead than for stations closer to the Equator. These differences are due to the latitude, the geometry of the constellation, and local obstructions.

The benefits of a multi-constellation approach, typically realized through increased redundancy and better satellite geometry to improve positioning accuracy, are reflected in the number of satellites tracked across these stations. Higher numbers of satellites at KIR8 contribute to a low PDOP and, besides that, a more favourable configuration of the satellites for precise positioning. According to Seeber (2003), a PDOP below 1.0 represents an excellent value, reflecting very low dilution effects on positional accuracy. The superior satellite visibility and geometry of KIR8 directly translate into its positioning performance; hence, for most epochs, it has a very low horizontal rms error of below 0.2 m. This result tends to imply that the error sources, particularly those due to multipath and atmospheric disturbances, were very well minimized by the operational conditions in this station. Although ASCG which is not as strong as KIR8, its performance reaches a mean of 0.96 for PDOP, while the rms errors become slightly higher to show implications of satellite visibility on accuracy. CHPG's average of 28 tracked satellites and PDOP of 1.00 indicates a more restricted satellite environment. This agrees with the observed higher horizontal rms errors that appear to imply suboptimal satellite geometry contributing to higher positional errors. van Diggelen (2009) pointed out that stations with fewer satellite observations along with higher PDOP are most likely to be affected by higher positioning errors due to degraded geometrical strength.

5.1.4 Measurement Redundancy and Number of Measurements

Measurement redundancy in GNSS refers to the availability of multiple satellite signals, which can be leveraged to improve positioning accuracy and reliability. As shown in Figure 5.5, KIR8 benefits from high measurement redundancy, with an average of 35 tracked satellites contributing to its positioning accuracy. The high count of the number of satellites allows for multiple observations, hence better mitigation of errors for more reliable solutions. Increased redundancy in measurements can reduce the effects of noise and multipath significantly, allowing better positional accuracy (Misra & Enge, 2011). Groves (2013) reported that additional measurements available will, in turn, enable advanced filtering techniques, such as Kalman filtering, to derive more accurate positioning outputs. The relationship between measurement redundancy, the number of tracked satellites, and positioning accuracy is evident among the stations PPP results from. KIR8 illustrates the case where a great number of satellites in view translate into superior performance of positioning, while the moderate number in ASCG has remained at a level enabling reasonable accuracy. On the other hand, the relatively low satellite visibility in CHPG underlines the possible setback brought about by inadequate measurement redundancy.

5.2 Influence of Multiple Error Sources on Positioning Performance

This section examines how variations in signal-to-noise ratio (SNR), satellite elevation, and multipath affect positioning accuracy at stations KIR8, ASCG, and CHPG. The analysis focuses on epoch-by-epoch processing, ensuring that each positioning solution is evaluated without influence from prior measurements.

Figures 5.6, 5.7, and 5.8 illustrate that at any given epoch, some satellites exhibit high elevation, strong SNR, and minimal multipath, while others display the opposite characteristics.

These variations lead to fluctuations in positioning accuracy, as weaker signals and poor geometry degrade the solution. Understanding these interactions is crucial for refining error mitigation strategies, optimizing satellite selection, and improving overall PPP performance.

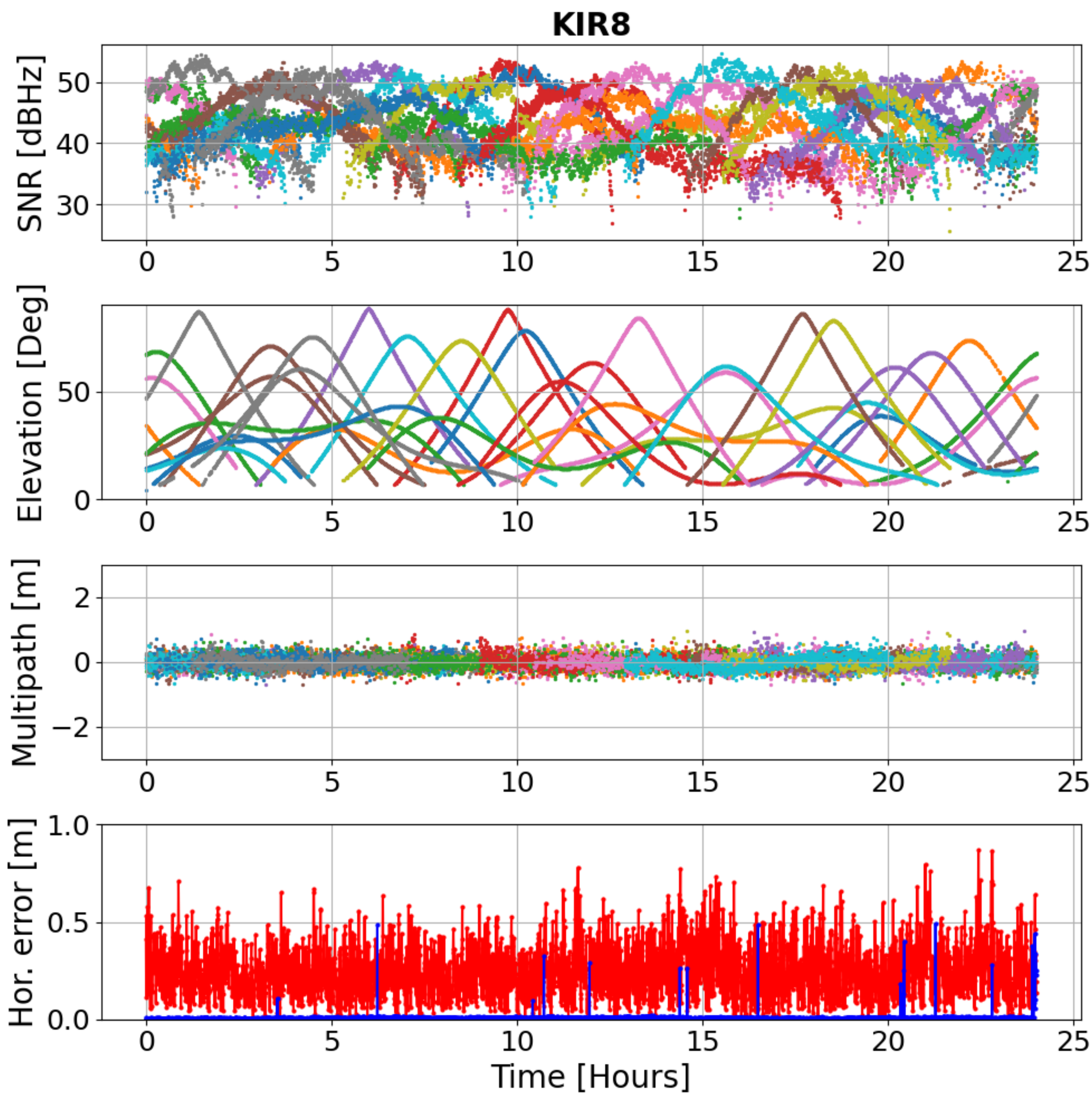

Figure 5.6: Top: Time series of SNR; Middle 1: Elevation; Middle 2: Pseudorange multipath; Bottom: Horizontal positional accuracy on first frequency for GPS satellites for KIR8 on DOY 015, 2024.

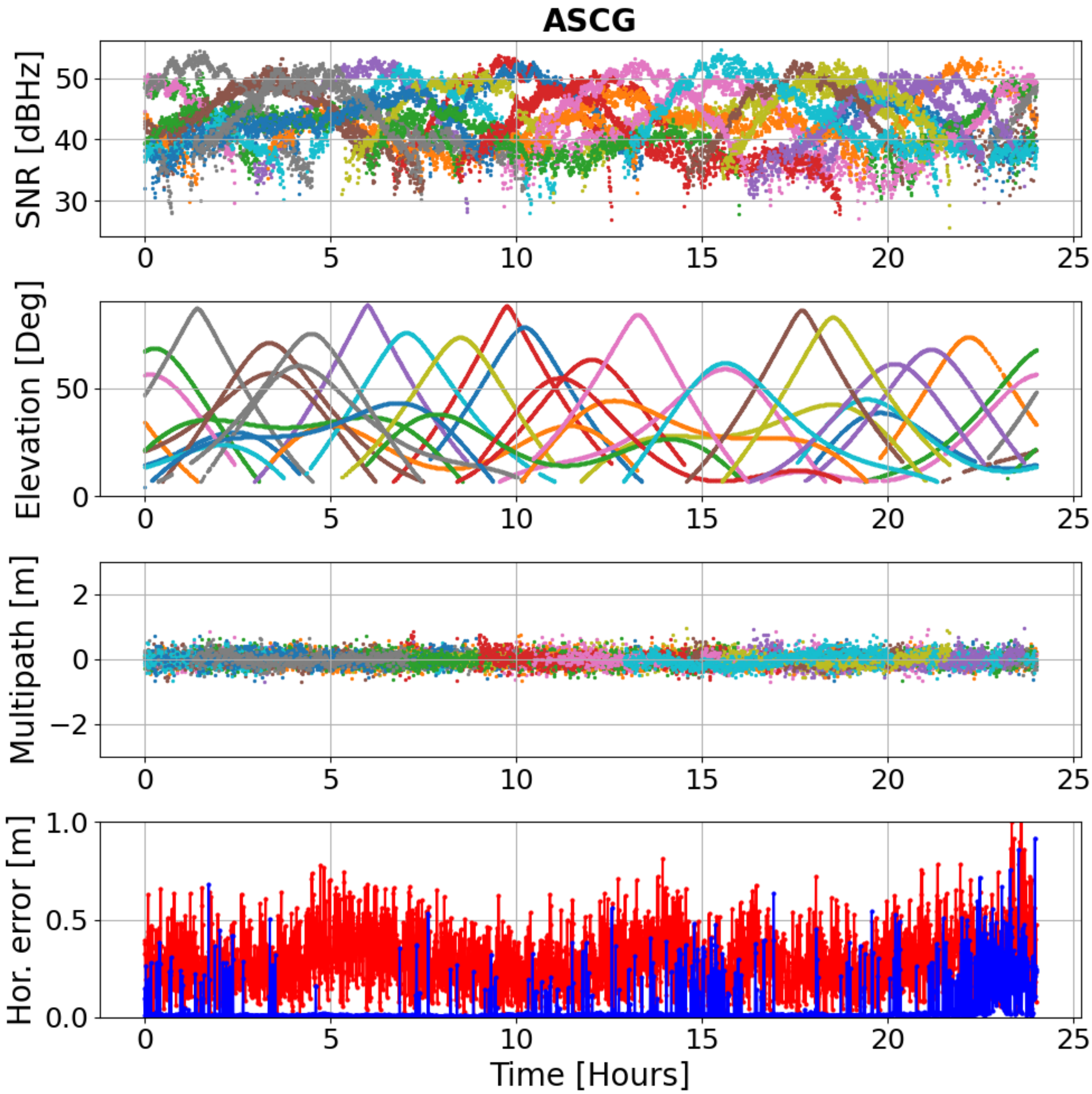

Figure 5.7: Top: Time series of SNR; Middle 1: Elevation; Middle 2: Pseudorange multipath; Bottom: Horizontal positional accuracy on first frequency for GPS satellites for ASCG on DOY 015, 2024.

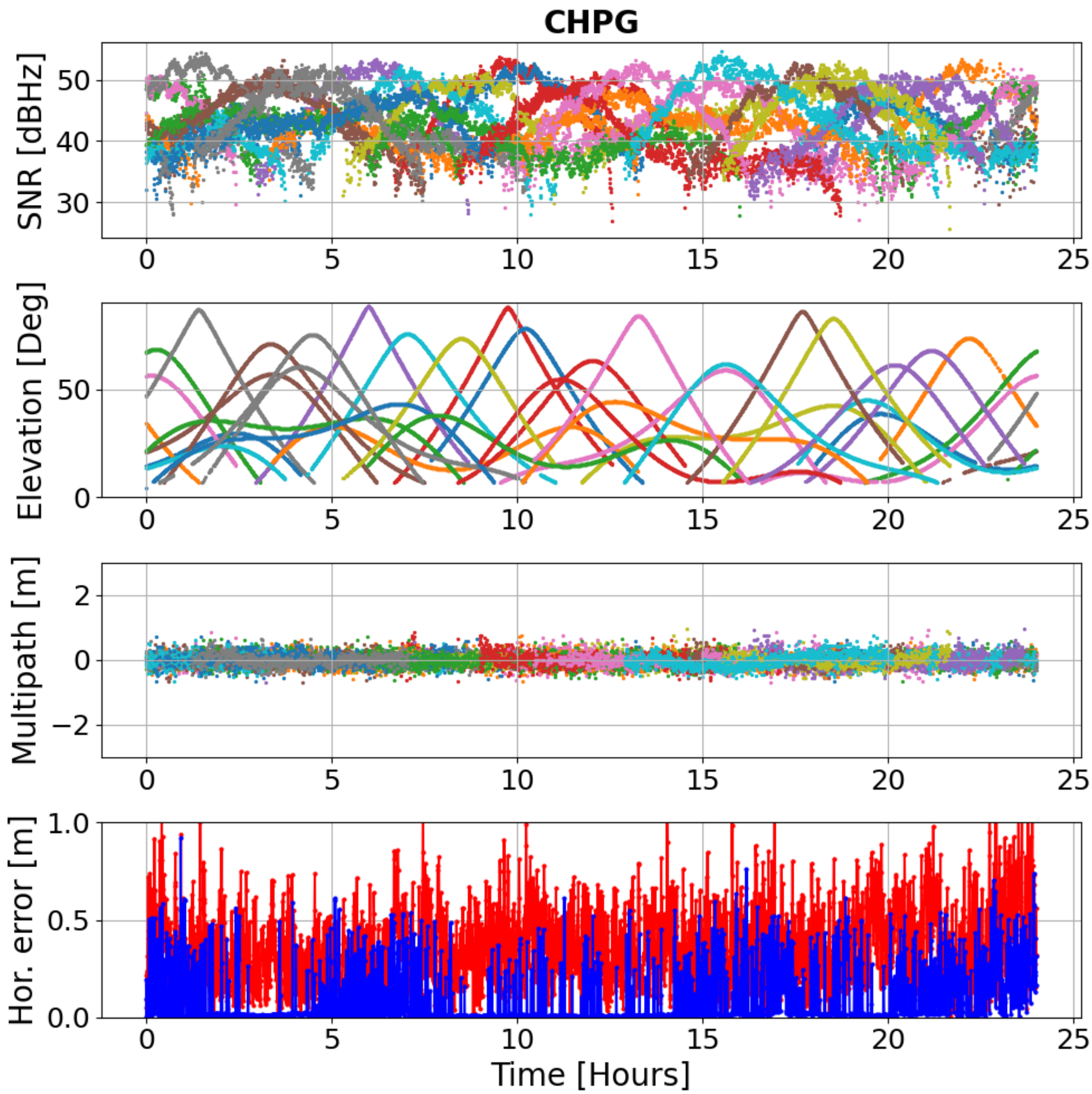

Figure 5.8: Top: Time series of SNR; Middle 1: Elevation; Middle 2: Pseudorange multipath; Bottom: Horizontal positional accuracy on first frequency for GPS satellites for CHPG on DOY 015, 2024.

For example, at some specific epochs, the ASCG's receiver can track satellites with high elevation and good SNR, while other satellites, which may be of low elevation and low SNR during that same epoch, will undermine the solution. This inconsistency is an indication that GNSS positioning is an inherently complex problem pointing to many influences on solution quality.

While high elevation and SNR of a satellite generally refer to more reliable solutions, multipath interference can seriously distort the measurement. For example, at ASCG, there are some occasions in which a high-elevation satellite suffers from a high multipath effect, which degrades the overall accuracy. In contrast, KIR8 has periods with several low elevation satellites, but because of the higher number of tracked satellites, enough redundancy is created which increases the reliability of the fixed solution.

Moreover, the interaction between SNR, elevation, and multipath is such that further complication to the analysis arises from interdependencies. Higher elevation angles usually increase the SNR and reduce multipath. However, as a combination of satellites with a mix of different and even opposing characteristics – one with favourable conditions and another with poor conditions - comes into view, the net effect on the positioning solution becomes ambiguous. In this respect, complexity arises in this form where metrics such as SNR and elevation are important, their contribution to positioning performance cannot be treated in isolation. Instead, it is the interaction between these factors that decides on the overall reliability of GNSS solutions at any given epoch.

Figure 5.9 shows scatter plots of average SNR values against float horizontal positioning errors at the stations KIR8, ASCG, and CHPG. The SNR value is calculated as the average over all frequencies (up to four) and constellations (GPS, GLONASS, Galileo, and BeiDou) at an epoch. The correlation coefficient that measures the strength of the relationship between SNR and horizontal error is provided in each individual subplot.

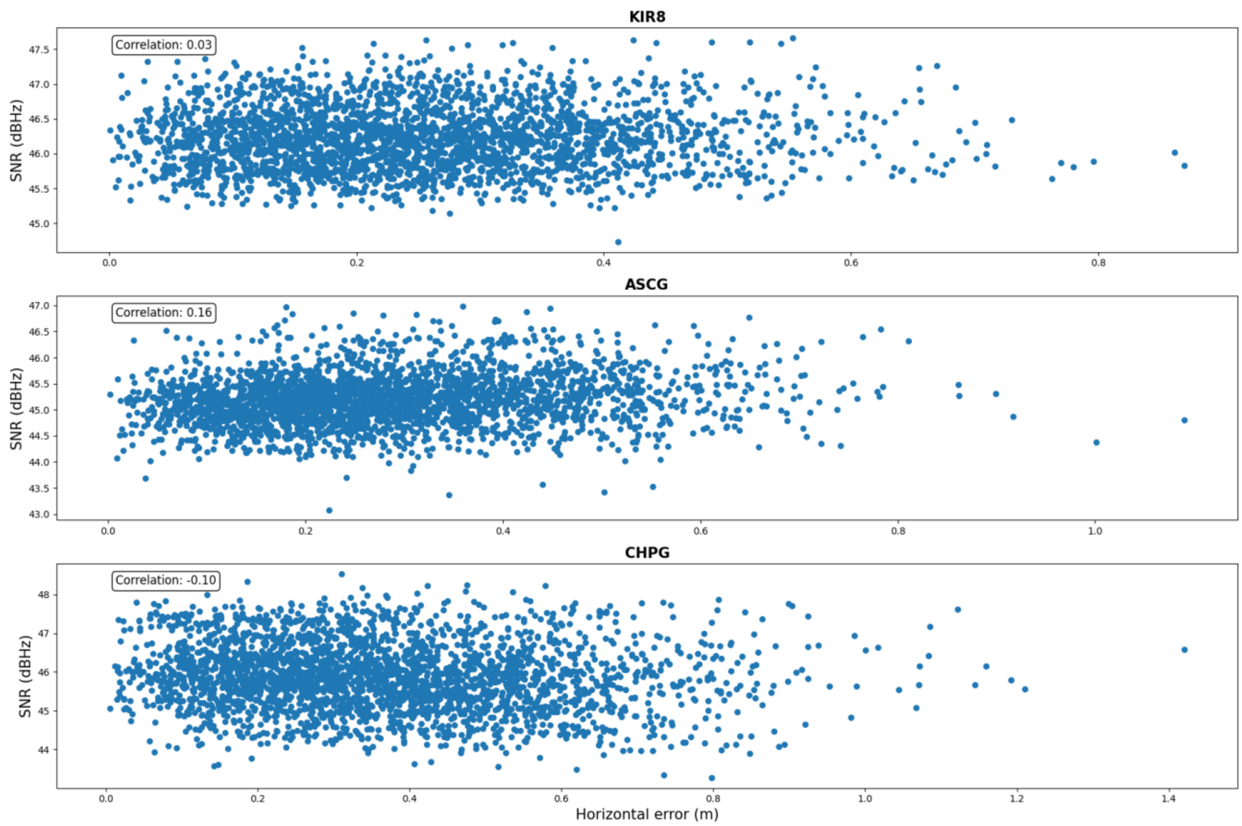

Figure 5.9: Scatter plots of average SNR values against float horizontal positioning errors for the stations KIR8, ASCG, and CHPG. Each SNR value is calculated as the average across all frequencies (up to four) and all constellations at an epoch

For KIR8, the coefficient of correlation is almost zero (0.03), which shows no clear relation between the average SNR and horizontal error. Data points are rather uniform in their spread, possibly meaning that the float horizontal error at this station is not much sensitive to variations of SNR, probably due to a favourable environment that does not generally cause degradation or blockage of the signal. Station ASCG yields a correlation coefficient of 0.16, which suggests a very weak positive relationship between average SNR and float horizontal error. The trend in the average SNR thus suggests that higher horizontal errors are associated with slightly higher SNR values. This counterintuitive trend may be because signal interference increases both the noise component of SNR and positioning errors in a more obstructed environment. For CHPG, the correlation coefficient is negative (-0.10), indicating a weak inverse relationship between SNR and float horizontal error. This weaker correlation value may suggest that lower horizontal errors are loosely associated with higher SNR values. While this trend follows expectations, the weak correlation reflects the complex interplay of factors affecting positioning accuracy at this station, including potential environmental obstructions or receiver characteristics.

Figure 5.10 shows scatter plots of average multipath values against horizontal positioning errors at the stations KIR8, ASCG, and CHPG. The multipath value is calculated as the average over all frequencies and constellations (GPS, GLONASS, Galileo, and BeiDou).

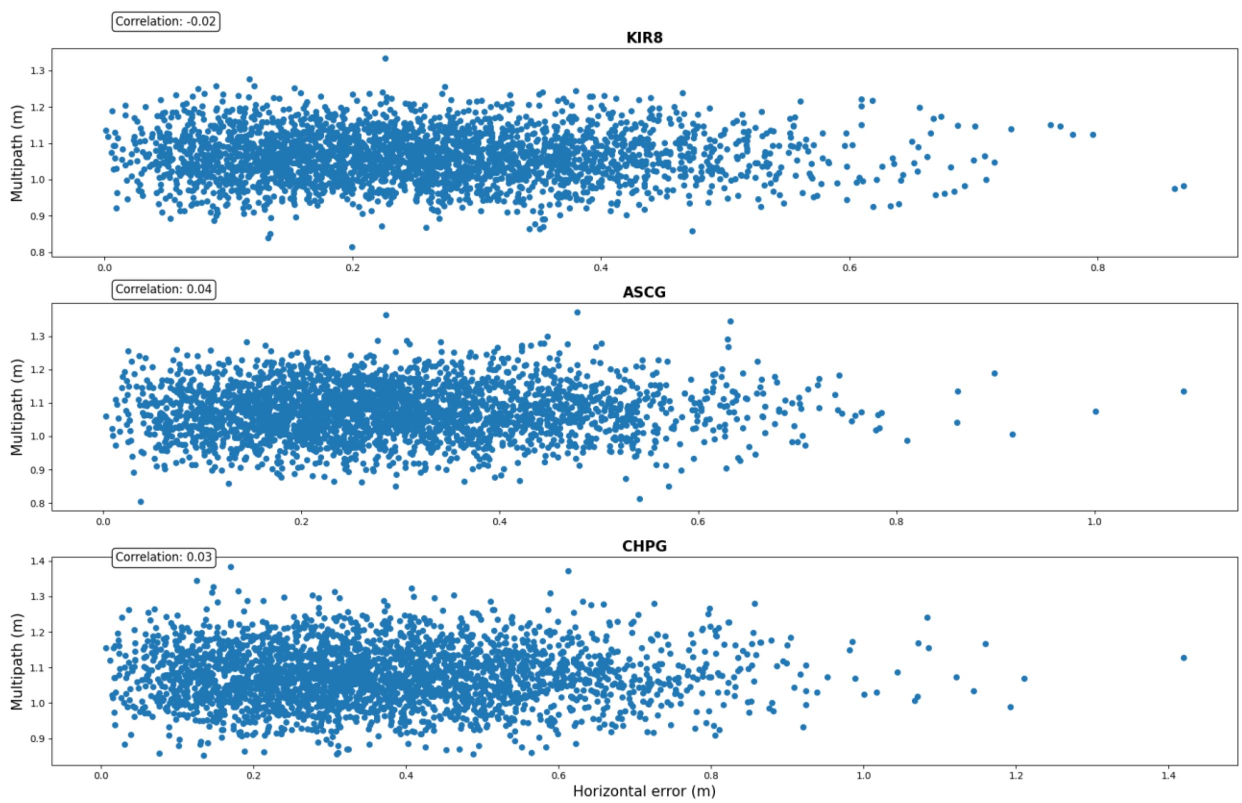

Figure 5.10: Scatter plots of average multipath values against float horizontal positioning errors for the stations KIR8, ASCG, and CHPG. Each SNR value is calculated as the average across all frequencies (up to four) and all constellations at an epoch

As in figure 5.9, there is no clear correlation between average multipath against float horizontal positioning errors as shown in figure 5.10. Stations KIR8, ASCG and CHPG have correlation coefficients of 0.04, 0.05 and -0.03 respectively showing approximately 0 correlation. In general, correlations at all three stations are weak, which may indicate that the influence of SNR and multipath on horizontal positioning accuracy is not well represented in these datasets. The specific environmental characteristics of each station do appear to play a defining role in modulating this relationship between SNR and multipath, and horizontal errors.

In summary, the combined analysis on SNR, elevation, and multipath showed that it is not easy to identify the cause of an outlier in PPP solutions. Because of the interplay of the different metrics involved, the result may be a good or bad solution at any epoch. This view highlights the complexity in PPP where many factors intersect. Such dynamics are important when improving the positioning accuracy of GNSS for practical applications, as rigorous analysis will need to take into consideration the complex relations that exist among these factors. Therefore, to better meet these challenges, rigorous statistical multivariate analysis, such as Principal Component Analysis, will be employed in the following section. This analysis would allow a better view of how the various factors that affect positioning performance interact and further refinement by analyzing the data.

5.3 Principal Component Analysis for Data Quality Indicators

Principal component analysis (PCA) is a statistical approach that reduces the dimensions of data while preserving the most amount of variance (Jolliffe & Cadima, 2016). PCA reduces the number of complex dataset dimensions by mapping linked variables into an uncorrelated small number of principal components. The main idea of this subsection is therefore to raise the factors that are most responsible for variations in positioning performance. This analysis becomes very useful in cases where several satellites are under observation at the same time as the combined effect due to SNR, elevation, and multipath for all satellites and epochs can be isolated using this approach. As concluded in the previous section, there is a difficulty in determining which of these factors alone is responsible for outliers or degraded positioning accuracy.

In the field of GNSS research, PCA has been applied in both the isolation of key error behaviours and enhancement of data interpretation. For instance, Dong et al. (2006) applied PCA with the purpose of extracting the common mode errors (CMEs) of GNSS time series to reduce noise and increase positioning accuracy. Similarly, Ji et al. (2023) developed an extended PCA approach for extracting CMEs from incomplete and heterogenous time series. Shen et al. (2014) also developed a modified PCA approach and extends the stacking approach for extracting CMEs from the incomplete position time series. Additionally, Li et al. (2020) implemented a variational bayesian PCA (VBPCA) for handling GNSS datasets with missing values. The effectiveness of the technique was showcased in proving the best representation, with incomplete or noisy data, by retaining significant statistical features. Zhu et al. (2023) applied PCA in interpolating missing data in GNSS-derived in precipitable water vapour. These studies illustrate how PCA can accommodate multivariate GNSS data and provide insights into isolating the main factors affecting positioning performance.

Building on the above, the current analysis applies PCA to the dataset from elevation, SNR, CMC (which captures various error sources including ionospheric delay, pseudorange multipath, and noise), and pre-fit residuals for pseudorange and carrier-phase measurements for the three stations KIR8, ASCG, and CHPG that have different performance levels. Measurements of the dataset for SNR, CMC, pre-fit residuals for both pseudorange and carrier-phase are over four frequencies. The four-frequency representation of data is useful in providing a comprehensive view of how errors and metrics of data quality change over different frequencies. Elevation remains the only variable that is independent of frequency, as it deals with how high the satellite is in the sky. PCA will contribute to the reduction of these metrics to a few principal components with the intention of understanding how each of these variables interacts with the others in their mutual influence on positioning performance. For instance, one may find that the first principal component indicates that a combination of low SNR and high pseudorange pre-fit residuals are responsible for most of the variability in the poorer performing station CHPG, while another component may indicate that high SNR along with low carrier-phase residuals contribute to the good performance at station KIR8.

Hotelling's T-squared which is a multivariate statistical measure used to determine whether the means of multiple groups differ significantly (Mason & Young, 2011), will be used in conjunction with the PCA to perform multivariate analysis of the principal components. The application of Hotelling's T-squared in this context is crucial for testing the principal components, derived from PCA, in identifying significant deviations in the principal component scores, thereby enhancing the robustness of multivariate analyses. The t-squared statistic for each observation is calculated to determine which combination of data quality metrics meaningfully deviates from the general mean and identifies which factors drive the variation in PPP solution.

5.3.1 Workflow of PCA

Figure 5.11 shows the flowchart methodology of the workflow of PCA performed on KIR8, ASCG and CHPG. The flowchart helps in visually demonstrating the sequential steps taken for effective processing and analysis of data quality metrics. Each step in this workflow is carefully designed to ensure that the data are preprocessed, analyzed, and interpreted to provide meaningful insight into the performance of GNSS measurements.

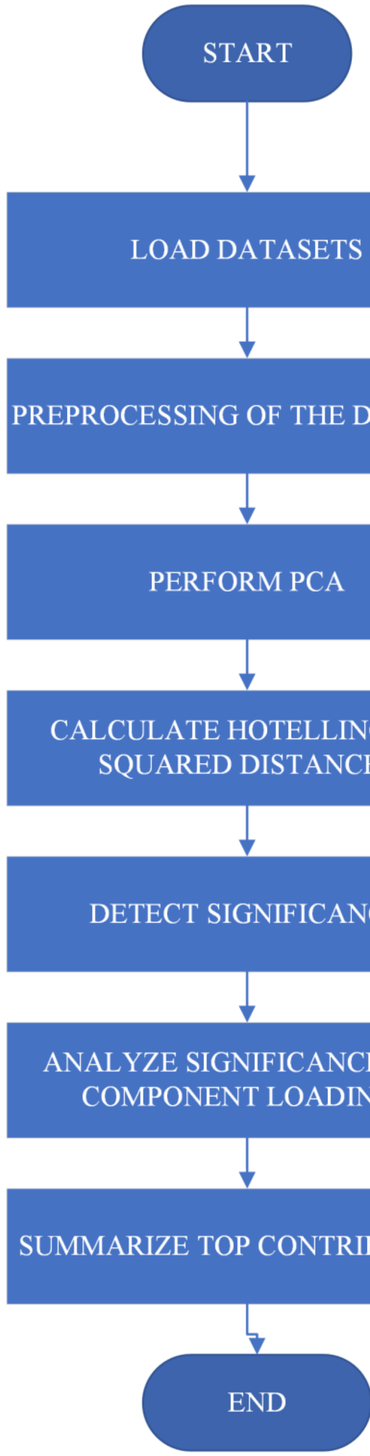

Figure 5.11: Flowchart methodology of the workflow of the PCA analysis for the stations KIR8, ASCG and CHPG

Loading of the datasets: The datasets from KIR8, ASCG and CHPG are loaded into the environment for processing. These contain 17 variables which include elevation, SNR values across four frequencies (SNR1, SNR2, SNR3, SNR4), Code minus carrier observables across four frequencies (CMC1, CMC2, CMC3, CMC4), and pre-fit residuals for both pseudorange and carrier-phase measurements across four frequencies (P1, P2, P3, P4 and L1, L2, L3, L4). Elevation is the satellite's angle above the horizon, affecting signal quality and vulnerability to atmospheric errors. SNR values reflect signal strength, with lower values implying weak reception. Code minus carrier observables used to evaluate signal reflections that can compromise positioning accuracy. Pre-fit residuals of pseudorange and carrier-phase measurements are indicators of measurement inconsistencies, with larger residuals implying larger potential unmodeled errors or even outliers in the data. In the analysis, elevation and SNR are used to assess good data quality indicators, CMC as a bad data quality indicator and pre-fit residuals of pseudorange and carrier-phase measurements identify measurement inconsistencies.

For CMC, it is mathematically defined as:

$$\text{CMC} = \text{Code (pseudorange measurement)} - \text{Carrier (carrier-phase measurement)} \tag{5.3}$$

$$\text{CMC} = 2I + M + m + e \tag{5.4}$$

where:

- I = Ionospheric delay
- M = Code multipath
- m = Phase multipath
- e = noise

Preprocessing of the dataset: Before the application of PCA, data are usually standardized or normalized. Standardization of data involves bringing the mean for every variable to 0 and the standard deviation to 1. This step ensures that all variables have an equal contribution to the analysis. In PCA, if not scaled, variables with larger magnitudes may dominate the analysis. Standardization of variables in this respect is important since PCA relies on variance. Even though two variables are not more important, the variables with larger scales will show more variance, thus biasing the results. Standardization makes sure all variables have an equal weight in the PCA model. This standardization was achieved by calculating the z-scores:

$$z = \frac{(x - \mu)}{\sigma} \tag{5.1}$$

where:

- z: z-score.
- x: value of the data point.
- μ: mean of the dataset.
- σ: standard deviation of the dataset.

The z-score indicates how many standard deviations an element is from the mean.

Performing PCA: Principal Component Analysis was then applied to these standardized datasets for the purposes of pattern identification and dimensionality reduction. PCA assists in the summarization of data through the transformation of initial variables into a new set of uncorrelated variables, known as principal components, that capture most of the variance within the data.

Calculate Hotelling's T-squared distances: After PCA, Hotelling's T-squared distances were calculated to assess the multivariate significance of datasets. The reason behind employing Hotelling’s T-squared approach to compliment the PCA is to detect multivariate outliers by accounting for correlations in the datasets, and test whether datasets have significant deviations from the mean. This approach is deemed statistically robust as it provides a more reliable measure of distance by scaling with variability unlike simple Euclidean distance. It is mathematically defined as:

$$T^2 = (x - \bar{x})^T S^{-1} (x - \bar{x}) \tag{5.2}$$

where:

- x: PCA score
- $\bar{x}$: mean of the PCA scores
- S: covariance matrix of the PCA scores
- T^2: squared distance scaled by the covariance. (It quantifies how unusual a data point is compared to the multivariate mean.)

Detecting Significance: At this stage, the computed distances falling outside of the expected distance range were checked for their significance. Detection of significance is important in understanding the reliability of data and may point out anomalies. Here, a critical threshold based on an F-distribution was used to detect which of the T-squared values are significant. A confidence level of 99% with the notation of 1% level of uncertainty was employed. The 99% confidence level helps in significantly reducing the likelihood of false positives thereby ensuring the reliability and robustness of the results with 1% probability of making a Type I error (rejecting a true null hypothesis).

Analyzing Significance and Component Loadings: In this step, the significant T-squared distances are traced back to the original dataset with their component loadings to determine which individual factors contribute to the combined quality of the Principal Components and further classify those measurements as low quality. This process enables a detailed examination of every measurement and pinpoint specific variables that negatively impact data quality.

Summarizing Top Contributors: Finally, the results were summarized to emphasize the most contributing variables, and this helps to understand which variables among all are more influential in determining the data quality metrics. Here, the frequency of appearance, average magnitude of contribution, and cumulative contribution are used to summarize the top contributors. Tracking how many times each variable appears among the top contributors allows for the identification of significant factors that repeatedly contribute to the analysis. Also, the average magnitude of contribution provides information on the principal contributors to the significant values, while the cumulative contribution outlines which variables have the highest overall impact. In all, these metrics together will enable in determining which variables are responsible for the outlier behavior throughout the dataset.

5.3.2 PCA Results and Discussions

The results are divided into explained variance analysis, component loading and variable contributions, detection of significant values and summary of top contributors.

5.3.2.1 Explained Variance Analysis

The explained variance ratio of the principal components for every station is plotted in Figure 5.12. It can be seen that the first two principal components of all the stations bear a high percentage of the total variance. Specifically, PC1 explains the highest percentage of variance in this dataset, with the bad station, CHPG, at approximately 25%, followed by the average, ASCG, at about 24% and good KIR8, at about 20%. This highest percentage of the explained variance in CHPG is because the first component captures more of the fundamental patterns in this dataset, with more marked variations present in the data reflected in its overall poorer performance.

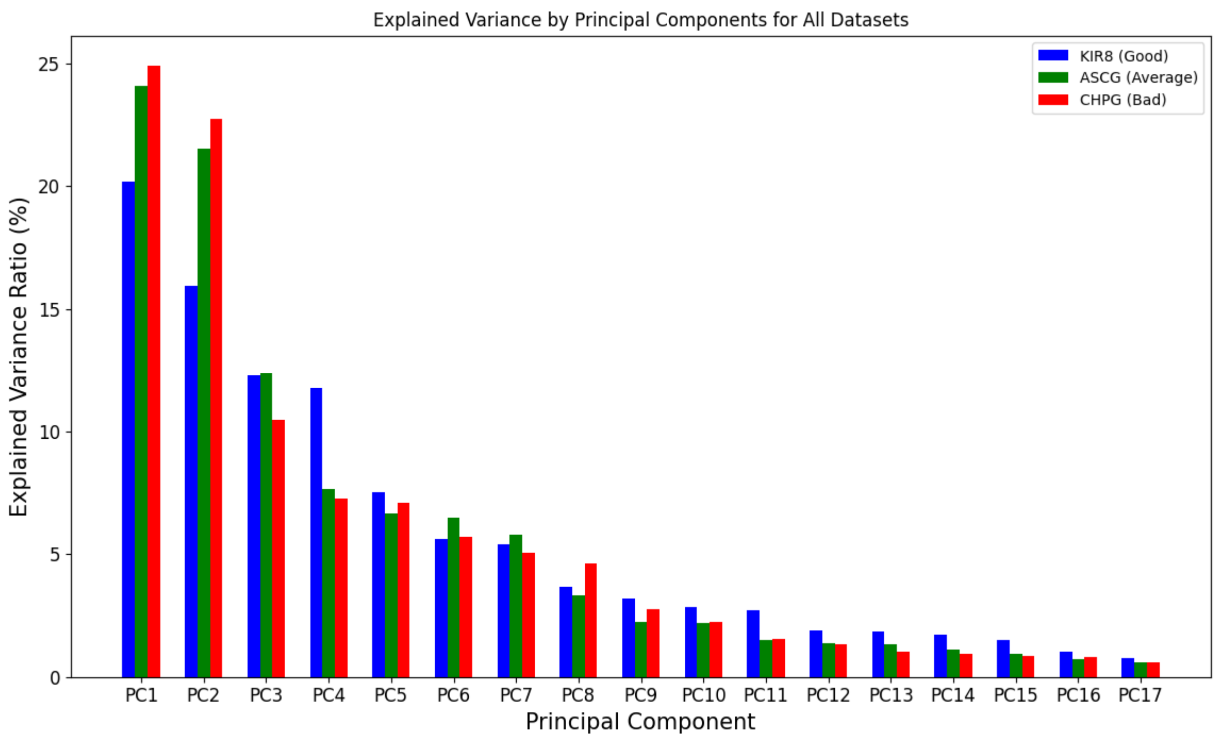

Figure 5.12: Explained variance ratio of the principal components for the three datasets in DOY 015, 2024

Similarly, for PC2, the explained variance ratio is highest at the bad station, as before, followed by the average and then good stations. This trend across the first two PCs suggest that while the data from a bad station is more variable, the lower variance of good station data implies that there is more consistency in the measurements. For the subsequent principal components, the explained variance declines rapidly, showing that the later components contribute little to the data's variability and, therefore, are not of much use when reconstructing the dataset.

The Figure 5.13 shows the PCA results station KIR8 (Good), ASCG (Average) and CHPG (Bad). For each station, there is a scree plot (left), a 2D scatter plot of PCA and a 3D scatter plot of PCA. A scree plot, shown on the left, visualizes the proportion of variance explained by each PC and the cumulative variance. The blue bars show the percentage of explained variance by the individual PCs, and the red line gives the cumulative variance. The green dashed line indicates 95% of the cumulative variance to identify the number of PCs that explains most of the variability in the data. This threshold was achieved by retaining 14 principal components for the good station and 12 for both the average and bad stations as shown the left side in Figure 5.13. This threshold for retention ensures that the greater part of information will remain while a tiny variance of 5% is rejected, with very minimal reconstruction error. The middle panel shows two-dimensional PCA scatter plots, where the data is projected onto the first two principal components (PC1 and PC2). Normal points are those observations closer to the mean value, while the significant points are those far away from the mean value, and potentially pointing out anomalies. The station KIR8 is represented by a cluster of close points with few significant jumps; that means stable and high-quality data. In the case of station ASCG, a wider scatter of significant points at average value indicating moderate variability. Large departures characterize the instability of CHPG and low quality in general. Shown on the right are the three-dimensional PCA scatter plots, which extend the analysis by projecting the data onto the first three principal components, PC1, PC2, and PC3. These types of plots allow for a better view of how the data are spread out in a higher dimensional space. KIR8 again shows a tight cluster of normal points with few significant outliers, consistent with its strong performance. ASCG has a more spread-out pattern showing significant divergence. CHPG has a high spread of significance in the three-dimensional space; this further emphasizes its low performance level and prevalence of anomalies.

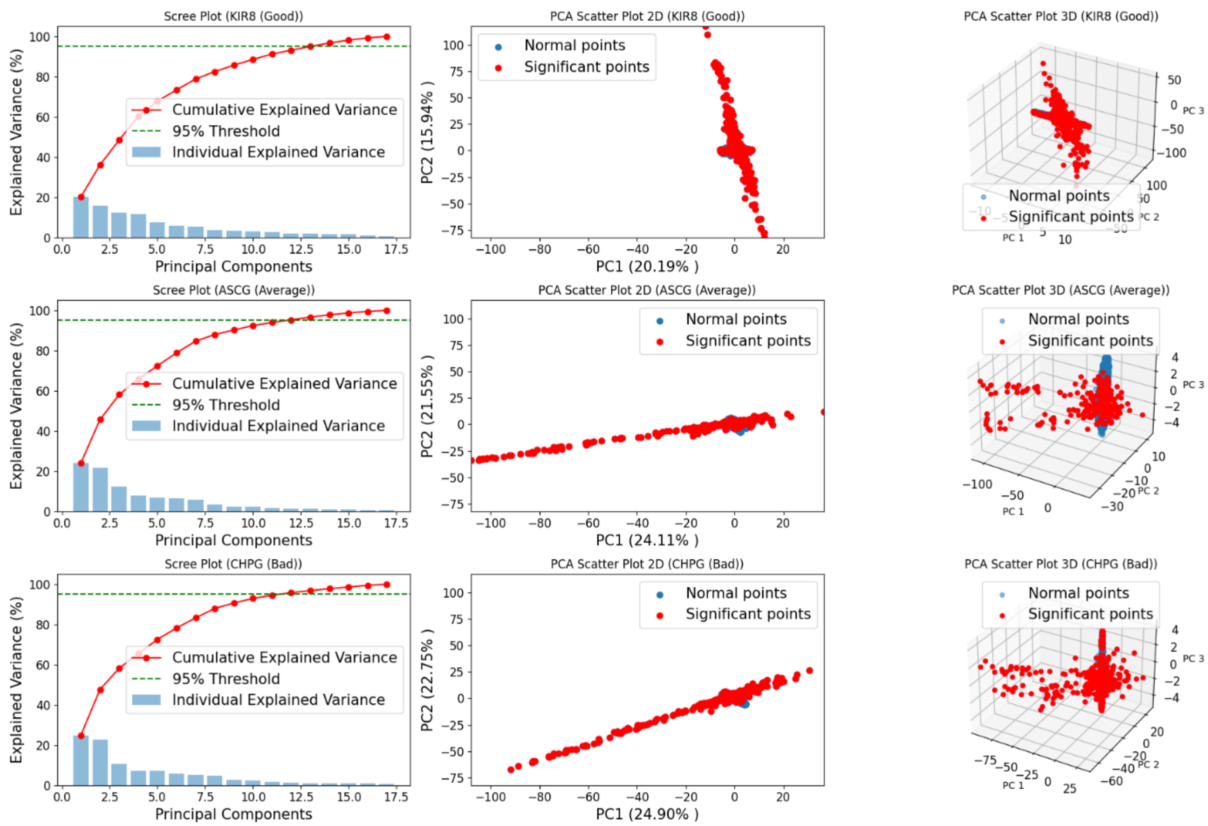

Figure 5.13: PCA results for KIR8, ASCG and CHPG on DOY 015, 2024. Left: Scree plot; Middle: 2D plots; Right: 3D plots of good, average and bad datasets with their significant value.

5.3.2.2 Component Loadings and Variable Contributions

Figure 5.14 below shows the principal component loadings for PC1 (left panel) and PC2 (right panel) for stations KIR8, ASCG and CHPG. Loadings are a measure of the extent to which each variable - elevation, SNR (for four frequencies), CMC (for four frequencies), and prefit residuals for pseudorange and carrier-phase (for four frequencies) - contributes to the total variance described by the first two principal components.

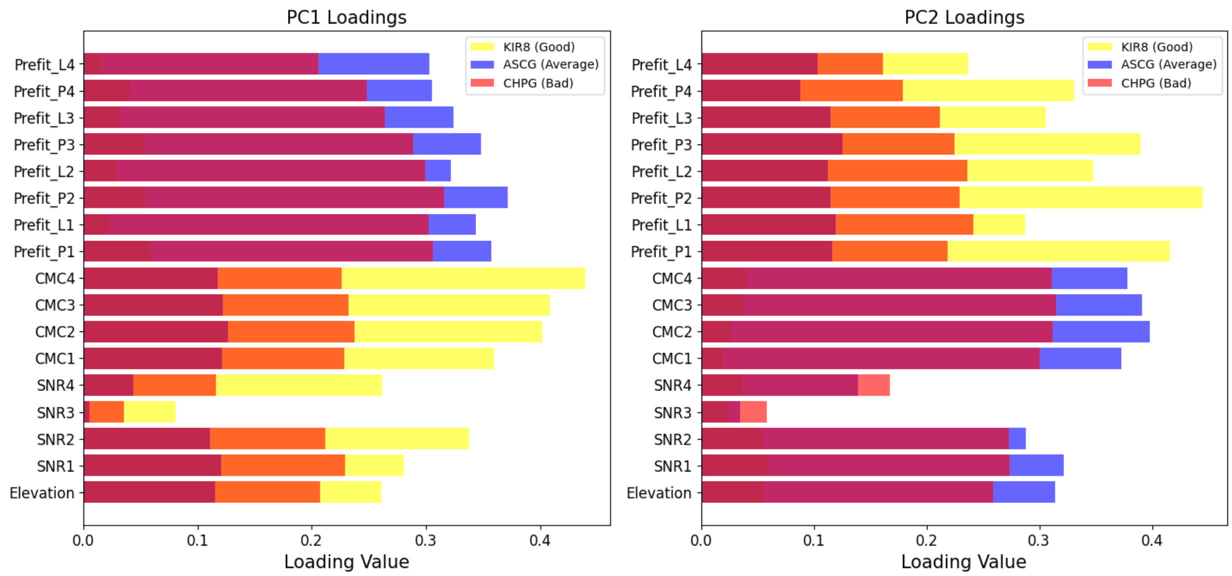

Figure 5.14: Component loadings of variables of the first and second principal components for the three datasets

For PC1, the loadings show that at KIR8, both elevation and SNR values over a range of frequencies contribute significantly. These high loadings mean that these factors are very important in determining the principal variance for the station with good performance. For CHPG, represented by red bars, prefit residuals over a range of frequencies have higher contributions, indicating that the observed poor performance is likely influenced by significant modelling inaccuracies or residual biases. ASCG represented by blue bars, shows a mix of contributions where some prefit residuals and CMC values have moderate effects, indicating its performance to be intermediate. PC2 shows a much wider amplitude of variation among loadings from the stations. At KIR8, its various contributions are more even between the prefit residuals and the SNR values, hence they are moderately influential in its definition, which indicates good overall quality of data. The contribution for CMC values dominates at the poor-performing station, CHPG. ASCG shows multi-variate contribution, including prefit residual and CMC, therefore these two components influence its second order variance.

The difference in loadings of PC1 and PC2 indicates different characteristics and performance measures of the three stations. At KIR8, the significant contributions from SNR and elevation suggest a very good performance under optimal conditions. High contribution from prefit residuals and CMC at CHPG suggests problems in reducing errors, leading to poor performance. ASCG represents a mix of factors corresponding to its moderate performance.

5.3.2.3 Detection of Significance Values

Figure 5.13 presents the 2D and 3D distributions of normal points and significant values identified using Hotelling's T-squared method. The total sample sizes for the good, average, and bad datasets were 100,487, 86,339, and 79,992, respectively, representing 24-hour data from DOY 015, 2024, for IGS stations KIR8, ASCG, and CHPG.

The analysis detected 1,486 potential outliers (1.5%) in the good dataset, 390 potential outliers (0.5%) in the average dataset, and 692 potential outliers (0.9%) in the bad dataset. Despite the bad dataset having fewer total observations, it exhibited a higher proportion of outliers than the average dataset. This suggests that the lower quality of observations in the bad dataset is more prone to significant deviations, likely due to factors such as signal obstruction, poor satellite geometry, or increased multipath effects. The relatively higher percentage of outliers in the good dataset, despite its high sample size, may indicate that even well-performing stations experience occasional anomalies, reinforcing the need for robust error detection techniques in PPP solutions.

5.3.2.4 Summary of Top Contributors

Variables with high frequencies and contributions in a cumulative manner were tagged as significant contributors towards degradation in data quality. For each significant value, the top 3 variables with the largest absolute loadings on the principal components associated with the significance are identified. These variables are considered the most likely contributors to the significance. A threshold of 10% is defined to help distinguish between variables that sporadically contribute to the significance and those that consistently do so. The frequency of each variable appearing as a top contributor across all outliers is summarized. Variables that consistently appear as top contributors across multiple significance are flagged as primary causes of the anomalies.

Figures 5.15 and 5.16 depict the frequency percentages of variables as the top contributors causing the significant values in KIR8, ASCG and CHPG on DOY 015, 2024 and DOY 016, 2024 respectively. In Figure 5.15, KIR8 as the good dataset has the highest percentage elevation of 39.6%. This shows that it is an important factor in the quality of the observations. It is normally true as high elevation angle signal produce are more accurate measurement for GNSS due to smaller disturbances from atmospheric delays, antenna sensitivity and multipath effects at that condition. For the average, which accounts for 10%, and bad datasets, which account for 6.5%, elevation becomes less important. This result suggests that the satellites with low elevation are responsible for the poorer quality within the average and bad datasets, making elevation a good data quality metric for good PPP solution.

In the good dataset, the values of SNR are relatively high, e.g., SNR1 is 99% and SNR2 is 72%, showing a strong signal with less noise. In the average dataset, SNR percentages are slightly lower: SNR1 (31.0%), SNR2 (34%), which indicate that this dataset still has a moderate signal strength but may have more noise creeping in than in the good dataset. In the bad dataset, the percentages in SNR1 are significantly lower than for the average datasets (18.2%), and SNR2 is similarly high (34%). This indicates increased signal degradation or interference. This result makes SNR a good data quality metric for good PPP solution.

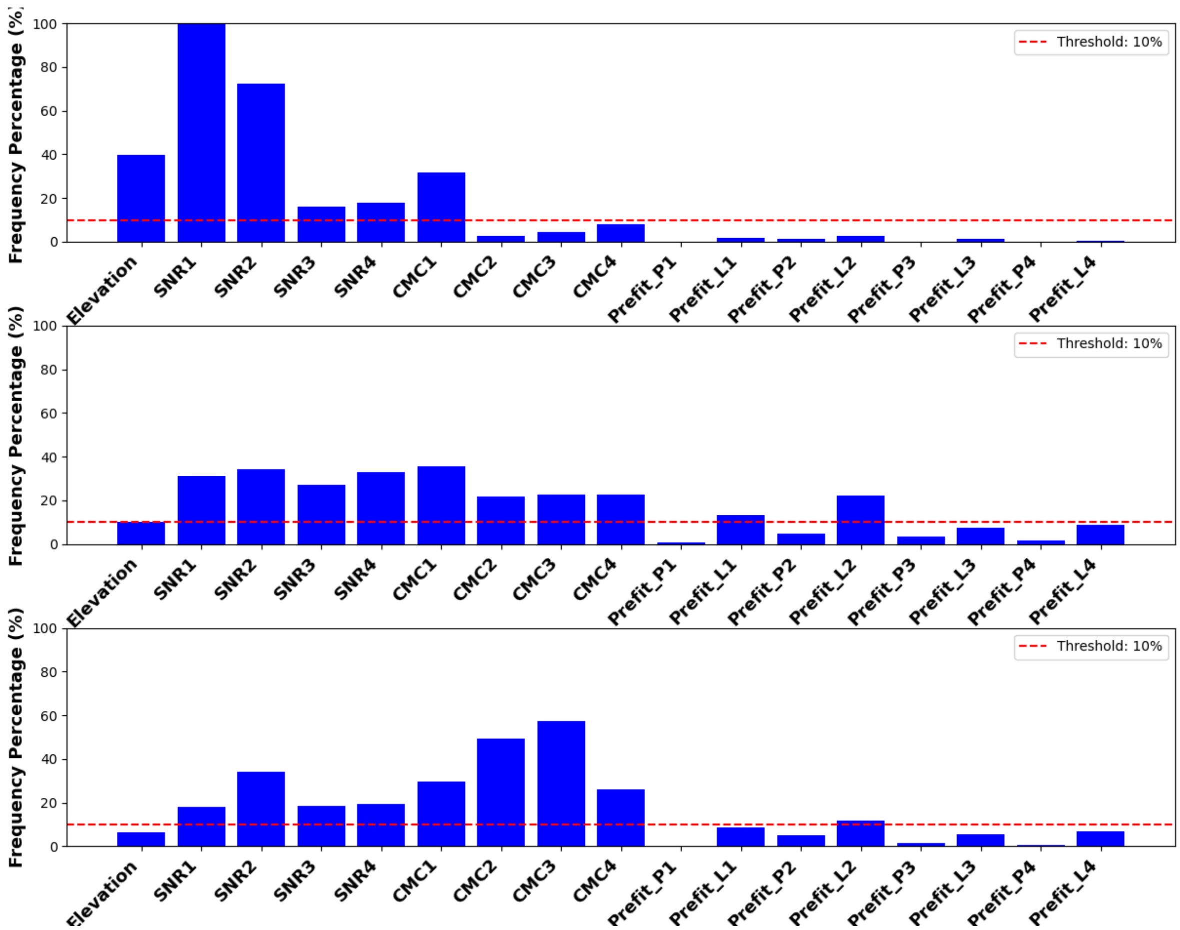

Figure 5.15: Frequency percentage of variables as top contributors across all significant values detected. Top: Good station (KIR8); Middle: Average station (ASCG); Bottom: Bad station (CHPG) on DOY 015, 2024.

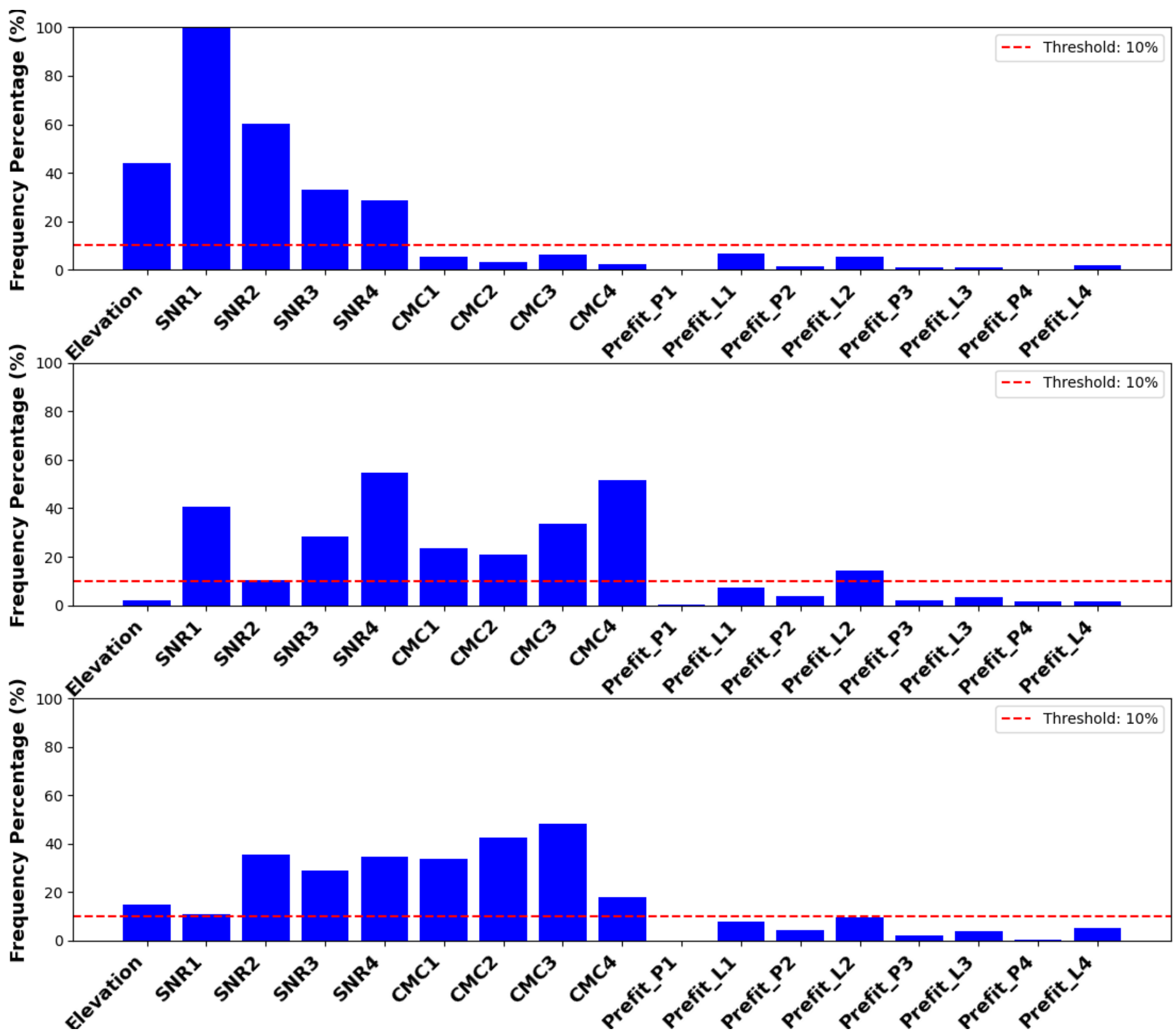

Figure 5.16: Frequency percentage of variables as top contributors across all significant values detected. Top: Good station (KIR8); Middle: Average station (ASCG); Bottom: Bad station (CHPG) on DOY 016, 2024.

CMC (code-minus-carrier) appears to behave in the opposite way. Its percentage is relatively low in the good dataset (e.g., CMC2: 5.3%) but increases in the average (23.2%) and significantly in the bad dataset (49.13% for CMC2 and even higher for CMC3 and CMC4). High CMC values in the bad dataset indicate increased divergence between the pseudorange and carrier-phase measurements, which is often a sign of errors such as multipath or signal degradation. As the CMC increases, it suggests the presence of more noise and greater discrepancies between the code and phase observations, leading to reduced positioning accuracy and making it a bad quality metric for good PPP solution. Similar conclusions drawn from Figure 5.15 can be seen in Figure 5.16 as elevation, SNR and CMC are the primary contributors to the outlier behaviour.

From the Equation 5.4, twice the ionospheric delay is left behind with code and phase multipaths. The phase multipath is considered very small in a millimetre-level so it can be neglected as sub-centimetre-level is required for now. The ionospheric delay is still estimated as part of the states in the PPP-AR uncombined processing. Several approaches have been adopted to reduce the delay. One of which is to use nearby base stations to correct for this phenomenon. On the global scale, the use of Global Ionospheric Map (GIM) has been employed but found out not to help improve the solution (Aggrey, 2018), so it can also be left unattended and estimated as a state. The only term left would be code multipath which needs to be mitigated to reduce the outliers and improve the overall solution.

Following from the PCA, even though elevation contributes to the overall reliability of the GNSS signals by being factored into the weighting scheme, SNR and code multipath are the major drivers for the outlier behaviour present in the geodetic MCMF PPP AR solutions. This finding aligns with previous studies highlighting the substantial impact of multipath and SNR variations on GNSS positioning accuracy. For example, Iliev et al. (2020) concluded that influence of multipath propagation of transmitted signal, causes additional peaks in the correlation function of the received signal and hence hinders the position accuracy. The author also saw that multipath propagation reduces the SNR of the received signal, leading to an increase in the synchronization error. Additionally, Park et al. (2024) applied a pseudorange acceleration as a weight to reduce multipath effect which has been as a major source of error in GNSS positioning, particularly in urban environments where reflected signals are prevalent. As a result of their application, they saw positioning accuracy improved by 75% and 79% horizontally and vertically, respectively. These conclusions infer that mitigating multipath and ensuring high SNR are crucial steps toward reducing outliers and improving the positioning accuracy, especially under poor satellite geometry or in interference-prone environments.

6 Conclusions and Recommendations

Conclusions are drawn on the work described in previous chapters of the thesis. Further, recommendations are made for future research that can be conducted as a continuation of the work.

6.1 Conclusions

This thesis explores different approaches and challenges toward achieving better performance in multi-constellation, multi-frequency Precise Point Positioning with ambiguity resolution and addressing the issues of previous studies in terms of solution improvement.

Chapter 3 presented key improvements to the previous work, underlining the extension of the DCM to four frequencies for BDS-3. The chapter also reviewed how limitations in previous work were addressed and how especially the separation of BDS-2 and BDS-3 clock terms in the design matrix was done. The previous results were seeing fluctuations in both horizontal and vertical positioning, but after the separation of the BDS-2 and BDS-3 clock terms in the design matrix, they both converge successfully. *The inclusion of the fourth frequency for the BDS-3-only solution saw the overall positioning accuracy of the horizontal errors reduced by 77% and 88% for float and fixed solutions, respectively*. Such enhancements were validated through comparative results, showing better performance in the current model compared to previous approaches. Processing was shifted from BDS-3-only to MCMF processing, which did show improvements in both horizontal and vertical positioning. *The 95th percentile RMSE in the previous work reduced from 1.2 cm to 1.1 cm in the current work, while the 67th and 100th percentile saw no improvements for the horizontal positioning*. *The vertical positioning saw improvements from 5.6 cm to 5.4 cm in the 100th percentile whilst the 67th and 95th percentiles remained the same*. The major improvement to the previous work was at the initial convergence time where the current work converged instantaneously at the 100th percentile. Previously, the solution took a minute to converge 100th percentile. This result leads to the assertion that increase of frequencies in the processing aids in converging the solution faster. The convergence time of the individual stations were compared at 95th percentile. *The previous and current work saw 63% and 81% of the stations converge instantaneously, respectively. This result shows a significant 18% improvement to the previous work.* An epoch-by-epoch solution performance was also compared with the aim of determining the percentage of epochs which are below 2.5 cm threshold horizontal error. The average of all stations in the percentage of epochs where the horizontal error was below 2.5 cm increased from 62%, within the previous work, to 72% in the current study, which marks an overall improvement of 10%. 21 out of the 27 stations used saw improvements, station ARHT saw no improvements with 5 stations with degrade average solutions. This degradation could be because of the BDS-2 and BDS-3 clock terms in the same column of the design matrix in the previous work making them to perform better.

The major novelty of the thesis is presented in Chapter 4, which investigated the causes and characteristics of position outliers in MCMF PPP-AR solutions. This chapter, through the processing of datasets on an epoch-by-epoch basis, circumvents error filtering and brings forth station performance variations. Detailed investigations into the causes of position outliers pointed at SNR, pseudorange multipath and noise, satellite visibility, geometry, and measurement redundancy were noted. The conclusions of this chapter were important in the understanding of how these factors contribute to position outliers in PPP solutions.

Chapter 5 extended the outlier analysis with correlation and PCA, which is explicitly part of the core novelty of the thesis. Correlation analysis attempted to determine how each error source identified in Chapter 4 affects the outliers, including both their individual and combined contributions to positioning performance. It was concluded in the correlation analysis that there is a combination of factors causing the outliers in the solution. Due to some inconclusive correlation results, PCA was next applied to identify the most significant metrics related to data quality that would have the largest impact on outliers. Elevation, SNR and CMC which combines ionospheric delay, pseudorange multipath and noise, were the most significant factors to the outliers. The good station, KIR8, had high frequency percentage for both elevation and SNR, with the bad station, CHPG, being the lowest. CMC was greater in the bad station than the good and the average. Since elevation is limited in this case, *it was concluded that SNR, ionospheric delay, pseudorange multipath and pseudorange noise are the primary causes of the outliers and needs to be mitigated*. These combined analyses had important implications for the relationships among various error sources and their impact on the PPP solution, developing a deeper understanding of outlier behavior. Dealing with the factors that affect performances as observed through the PCA are meant as future work.

6.2 Recommendations

In this thesis, the following recommendations for future work are provided based on the work that has been presented.

6.2.1 Improve Weighting Scheme

To enhance the accuracy of the York-PPP engine, it is recommended to change the current elevation-based weighting scheme to incorporate signal-to-noise ratio (SNR) and pseudorange multipath effects. The analysis from principal component analysis (PCA) indicates that these factors significantly contribute to outliers in the positioning results. A more comprehensive weighting model would be developed to account for individual measurements from each GNSS constellation, as well as the varying quality of pseudorange and carrier-phase observations across different frequencies. The weighting scheme could be adjusted to assign lower weights on the affected measurements during high multipath and low SNR. It would potentially improve the general robustness of the positioning solution by mitigating the adverse impacts of noise and multipath interference to achieve the positioning results more reliably and accurately.

6.2.2 Expansion of DCM to Five-Frequency PPP-AR

Further improvement in the DCM performance at PPP-AR will be obtained by expanding the model to accommodate five frequencies. The existing uncombined DCM is already capable of processing up to four frequencies, but with the improvements of the constellations Galileo and BeiDou-3 that offer up to five frequencies, the improvement is expected. The expansion should elaborate on the same logical structure developed to three and four frequencies already extended with ensuring that use of that additional frequency information allows robust and more precise positioning solutions to be available.

6.2.3 Integration of Artificial Intelligence/ Machine Learning for Outlier Detection

To further improve the outlier detection and outlier correction in PPP-AR, Artificial Intelligence (AI) and Machine Learning (ML) techniques should be utilized. These advanced methods can identify outliers through large dataset analysis in relation to patterns which traditional approaches may overlook. AI/ML can maybe greatly improve the positioning solution robustness and accuracy through the effective identification and mitigation of noise and multipath interference effects. These techniques will further bring out robust performance in GNSS applications.

References

Abdelazeem, M., Çelik, R. N., & El-Rabbany, A. (2016). MGR-DCB: A Precise Model for Multi-Constellation GNSS Receiver Differential Code Bias. *Journal of Navigation*, *69*(4), 698–708. https://doi.org/10.1017/S0373463315000922

Aggrey, J. (2018). Assessment of Global and Regional Ionospheric Corrections in Multi-GNSS PPP. *31st International Technical Meeting of The Satellite Division of the Institute of Navigation (ION GNSS+ 2018)*, 3967–3981. https://doi.org/10.33012/2018.16079

Ashby, N. (2003). Relativity in the Global Positioning System. *Living Reviews in Relativity*, *6*(1). http://www.livingreviews.org/lrr-2003-1

Banville, S., Collins, P., Zhang, W., & Langley, R. B. (2014). Global and Regional Ionospheric Corrections for Faster PPP Convergence. *Navigation*, *61*(2), 10.

Bertiger, W., Desai, S. D., Haines, B., Harvey, N., Moore, A. W., Owen, S., & Weiss, J. P. (2010). Single receiver phase ambiguity resolution with GPS data. *Journal of Geodesy*, *84*(5), 327–337. https://doi.org/10.1007/s00190-010-0371-9

Bisnath, S. (2020). Relative Positioning and Real-Time Kinematic (RTK). In *Position, Navigation, and Timing Technologies in the 21st Century* (pp. 481–502). John Wiley & Sons, Ltd. https://doi.org/10.1002/9781119458449.ch19

Bisnath, S., & Gao, Y. (2009). Current state of precise point positioning and future prospects and limitations. In *In Observing our changing earth* (pp. 615–623). Springer. http://link.springer.com/chapter/10.1007/978-3-540-85426-5_71

Bisnath, S., Saeidi, A., WANG, J.-G., & Seepersad, G. (2013). Evaluation of Network RTK Performance and Elements of Certification—A Southern Ontario Case Study. *Geomatica*, *67*(4), 243–251. https://doi.org/10.5623/cig2013-050

Blewitt, G. (1990). An Automatic Editing Algorithm for GPS data. *Geophysical Research Letters*, *17*(3), 199–202. https://doi.org/10.1029/GL017i003p00199

Cai, L., & Gao, Y. (2013). Impact of Multi-Constellation Integration on PPP Convergence Time. *Journal of Navigation*, *66*(3), 495–510.

Chang, X., Yang, X., & Zhou, T. (2005). MLAMBDA: A Modified LAMBDA Method for Integer Ambiguity Determination. *St Annual Meeting*, 12.

Ciraolo, L., Azpilicueta, F., Brunini, C., Meza, A., & Radicella, S. M. (2007). Calibration errors on experimental slant total electron content (TEC) determined with GPS. *Journal of Geodesy*, *81*(2), 111–120. https://doi.org/10.1007/s00190-006-0093-1

Collins, P., Lahaye, F., & Bisnath, S. (2012). *External Ionospheric Constraints for Improved PPP-AR Initialisation and a Generalised Local Augmentation Concept*. 3055–3065. http://www.ion.org/publications/abstract.cfm?jp=p&articleID=10485

Collins, P., Lahaye, F., Heroux, P., & Bisnath, S. (2008). Precise Point Positioning with Ambiguity Resolution using the Decoupled Clock Model. *Proceedings of the 21st International Technical Meeting of the Satellite Division of The Institute of Navigation (ION GNSS 2008)*, 1315–1322. http://www.ion.org/publications/abstract.cfm?jp=p&articleID=8043

Deng, Z., Nischan, T., & Bradke, M. (2017). Multi-GNSS Rapid Orbit-, Clock- & EOP-Product Series. *GFZ Data Services*. https://doi.org/10.5880/GFZ.1.1.2017.002

Dong, D., Fang, P., Bock, Y., Webb, F., Prawirodirdjo, L., Kedar, S., & Jamason, P. (2006). Spatiotemporal filtering using principal component analysis and Karhunen-Loeve expansion approaches for regional GPS network analysis. *Journal of Geophysical Research: Solid Earth*, *111*(B3), 2005JB003806. https://doi.org/10.1029/2005JB003806

Dow, J. M., Neilan, R. E., & Rizos, C. (2009). The International GNSS Service in a changing landscape of Global Navigation Satellite Systems. *Journal of Geodesy*, *83*(3–4), 191–198. https://doi.org/10.1007/s00190-008-0300-3

Enge, P. K. (1994). The Global Positioning System: Signals, measurements, and performance. *International Journal of Wireless Information Networks*, *1*(2), 83–105.

Gao, W., Zhao, Q., Meng, X., & Pan, S. (2021). Performance of Single-Epoch EWL/WL/NL Ambiguity-Fixed Precise Point Positioning with Regional Atmosphere Modelling. *Remote Sensing*, *13*(18), Article 18. https://doi.org/10.3390/rs13183758

Gao, Y., & Chen, K. (2004). Performance analysis of precise point positioning using real-time orbit and clock products. *Journal of Global Positioning System*, *1*(08), 95–100.

Gao, Y., Li, Z., & McLellan, J. F. (1997). Carrier Phase Based Regional Area Differential GPS for Decimeter-Level Positioning and Navigation. *Proceedings of the 10th International Technical Meeting of the Satellite Division of The Institute of Navigation (ION GPS 1997)*, 1305–1313. http://www.ion.org/publications/abstract.cfm?jp=p&articleID=2916

Gao, Y., & Shen, X. (2002). A New Method for Carrier-Phase-Based Precise Point Positioning. *Navigation*, *49*(2), 109–116.

Ge, M., Gendt, G., Rothacher, M., Shi, C., & Liu, J. (2008). Resolution of GPS carrier-phase ambiguities in Precise Point Positioning (PPP) with daily observations. *Journal of Geodesy*, *82*(7), 389–399. https://doi.org/10.1007/s00190-007-0187-4

Geng, J., Guo, J., Chang, H., & Li, X. (2019). Toward global instantaneous decimeter-level positioning using tightly coupled multi-constellation and multi-frequency GNSS. *Journal of Geodesy*, *93*(7), 977–991.

Geng, J., Shi, C., Ge, M., & Dodson, A. H. (2018). Enhancing PPP Accuracy with Multi-Constellation GNSS Integration. *Navigation*, *65*(4), 367–384.

Geng, J., Shi, C., Ge, M., Dodson, A. H., Lou, Y., Zhao, Q., & Liu, J. (2012). Improving the estimation of fractional-cycle biases for ambiguity resolution in precise point positioning. *Journal of Geodesy*, *86*(8), 579–589. https://doi.org/10.1007/s00190-011-0537-0

Giménez, E., Crespi, M., Garrido, M. S., & Gil, A. J. (2012). Multivariate outlier detection based on robust computation of Mahalanobis distances. Application to positioning assisted by RTK GNSS Networks. *International Journal of Applied Earth Observation and Geoinformation*, *16*, 94–100. https://doi.org/10.1016/j.jag.2011.11.011

Groves, P. D. (2013). *Principles of GNSS, Inertial, and Multisensor Integrated Navigation Systems, Second Edition*. Artech House.

Guo, J., Zhang, Q., Li, G., & Zhang, K. (2021). Assessment of Multi-Frequency PPP Ambiguity Resolution Using Galileo and BeiDou-3 Signals. *Remote Sensing*, *13*(23), 4746. https://doi.org/10.3390/rs13234746

He Chengyan, Guo Ji, Lu Xiaochun, & Lu Jun. (2014). Multipath performance analysis of GNSS navigation signals. *2014 IEEE Workshop on Electronics, Computer and Applications*, 379–382. https://doi.org/10.1109/IWECA.2014.6845636

Hofmann-Wellenhof, B., Lichtenegger, H., & Wasle, E. (2008). *GNSS--global navigation satellite systems: GPS, GLONASS, Galileo, and more*. Springer.

Hopfield, H. S. (1969). Two-quartic tropospheric refractivity profile for correcting satellite data. *Journal of Geophysical Research*, *74*(18), 4487–4499.

Iliev, T. B., Ivanova, E. P., Stoyanov, I. S., Beloev, I. H., & Mihaylov, G. Y. (2020). GNSS for Accuracy Positioning in Mobile Communications with Multipath Propagation of the Signal. *2020 7th International Conference on Energy Efficiency and Agricultural Engineering (EE&AE)*, 1–4. https://doi.org/10.1109/EEAE49144.2020.9279057

Iliev, T. B., Stoyanov, I. S., Sokolov, S. A., & Beloev, I. H. (2020). The Influence of Multipath Propagation of the Signal on the Accuracy of the GNSS Receiver. *2020 43rd International Convention on Information, Communication and Electronic Technology (MIPRO)*, 508–511. https://doi.org/10.23919/MIPRO48935.2020.9245409

Jensen, A. B. O., & Cannon, M. E. (2000). *Performance of Network RTK Using Fixed and Float Ambiguities*. 797–805. http://www.ion.org/publications/abstract.cfm?jp=p&articleID=95

Ji, K., Shen, Y., Chen, Q., & Feng, T. (2023). Extended Principal Component Analysis for Spatiotemporal Filtering of Incomplete Heterogeneous GNSS Position Time Series. *IEEE Transactions on Geoscience and Remote Sensing*, *61*, 1–19. https://doi.org/10.1109/TGRS.2023.3277460

Jolliffe, I. T., & Cadima, J. (2016). Principal component analysis: A review and recent developments. *Philosophical Transactions of the Royal Society A: Mathematical, Physical and Engineering Sciences*, *374*(2065), 20150202. https://doi.org/10.1098/rsta.2015.0202

Kaplan, E. D., & Hegarty, C. (Eds.). (2006). *Understanding GPS: Principles and applications* (2nd ed). Artech House.

Karaim, M., Elsheikh, M., & Noureldin, A. (2018). GNSS Error Sources. In R. B. Rustamov & A. M. Hashimov (Eds.), *Multifunctional Operation and Application of GPS*. InTech. https://doi.org/10.5772/intechopen.75493

Klobuchar, J. A. (1987). Ionospheric time-delay algorithm for single-frequency GPS users. *IEEE Transactions on Aerospace and Electronic Systems*, *3*, 325–331.

Kos, T., Botinčan, M., & Dlesk, A. (2009). Mitigating GNSS Positioning Errors Due To Atmospheric Signal Delays. *Pomorstvo*, *23*(2), 495–513.

Kouba, J. (2009). Testing of global pressure temperature (GPT) model and global mapping function (GMF) in GPS analyses. *Journal of Geodesy*, *83*(3–4), 199–208.

Kouba, J., & Héroux, P. (2001). Precise point positioning using IGS orbit and clock products. *GPS Solutions*, *5*(2), 12–28.

Kremer, G., Kalafus, R., Loomis, P., & Reynolds, J. (1990). The Effect of Selective Availability on Differential GPS Corrections. In *Navigation* (Vol. 37, pp. 39–52). Wiley Online Library. https://doi.org/10.1002/j.2161-4296.1990.tb01533.x

Laurichesse, D., & Banville, S. (2018). Instantaneous centimeter-level multi-frequency precise point positioning. *GPS World*. https://www.gpsworld.com/innovation-instantaneous-centimeter-level-multi-frequency-precise-point-positioning/

Laurichesse, D., & Blot, A. (2016). Fast PPP Convergence Using Multi-Constellation and Triple-Frequency Ambiguity Resolution. *Proceedings of the 29th International Technical Meeting of The Satellite Division of the Institute of Navigation (ION GNSS+ 2016)*, 2082–2088.

Laurichesse, D., Mercier, F., Berthias, J.-P., Broca, P., & Cerri, L. (2009). Integer ambiguity resolution on undifferenced GPS phase measurements and its application to PPP and satellite precise orbit determination. *Navigation*, *56*(2), 135–149.

Laurichesse, D., & Privat, A. (2015). An Open-source PPP Client Implementation for the CNES PPP-WIZARD Demonstrator. *Proceedings of the 28th International Technical Meeting of the Satellite Division of The Institute of Navigation (ION GNSS+ 2015)*, 2780–2789.

Leick, A., Rapoport, L., & Tatarnikov, D. (2015). *GPS satellite surveying* (4th ed). John Wiley & Sons.

Li, M., Qu, L., Zhao, Q., Guo, J., Su, X., & Li, X. (2014). Precise Point Positioning with the BeiDou Navigation Satellite System. *Sensors*, *14*(1), 927–943.

Li, P., Zhang, X., Ge, M., Wang, R., Shen, Y., & Schuh, H. (2017). Real-time precise point positioning regional augmentation using a recursive estimation method. *GPS Solutions*, *21*(4), 1565–1576.

Li, W., Jiang, W., Li, Z., Chen, H., Chen, Q., Wang, J., & Zhu, G. (2020). Extracting Common Mode Errors of Regional GNSS Position Time Series in the Presence of Missing Data by Variational Bayesian Principal Component Analysis. *Sensors*, *20*(8), 2298.

Li, X., Li, X., Liu, G., Feng, G., Yuan, Y., Zhang, K., & Ren, X. (2019). Triple-frequency PPP ambiguity resolution with multi-constellation GNSS: BDS and Galileo. *Journal of Geodesy*, *93*(8), 1105–1122. https://doi.org/10.1007/s00190-019-01229-x

Li, X., Liu, G., Li, X., Zhou, F., Feng, G., Yuan, Y., & Zhang, K. (2020). Galileo PPP rapid ambiguity resolution with five-frequency observations. *GPS Solutions*, *24*(1), 24. https://doi.org/10.1007/s10291-019-0930-3

Li, X., Wang, B., Li, X., Huang, J., Lyu, H., & Han, X. (2022). Principle and performance of multi-frequency and multi-GNSS PPP-RTK. *Satellite Navigation*, *3*(1), 7. https://doi.org/10.1186/s43020-022-00068-0

Magyar, B., Kenyeres, A., Tóth, S., Hajdu, I., & Horváth, R. (2022). Spatial outlier detection on discrete GNSS velocity fields using robust Mahalanobis-distance-based unsupervised classification. *GPS Solutions*, *26*(4), 145. https://doi.org/10.1007/s10291-022-01323-2

Mannucci, A. J., Wilson, B. D., & Edwards, C. D. (1993). A New Method for Monitoring the Earth's Ionospheric Total Electron Content Using the GPS Global Network. *Proceedings of the 6th International Technical Meeting of the Satellite Division of The Institute of Navigation (ION GPS 1993)*, 1323–1332.

Mason, R. L., & Young, J. C. (2011). Hotelling's T2Statistic. In M. Lovric (Ed.), *International Encyclopedia of Statistical Science* (pp. 638–640). Springer Berlin Heidelberg. https://doi.org/10.1007/978-3-642-04898-2_292

Misra, P., & Enge, P. (2006). *Global Positioning System: Signals, measurements and performance second edition* (2nd ed.). Ganga-Jamuna Press.

Misra, P., & Enge, P. (2011). *Global Positioning System: Signals, Measurements and Performance Revised Second Edition* (2nd ed.). Ganga-Jamuna Press.

Montenbruck, O., Steigenberger, P., & Hauschild, A. (2018a). Multi-GNSS signal-in-space range error assessment – Methodology and results. *Advances in Space Research*, *61*(12), 3020–3038. https://doi.org/10.1016/j.asr.2018.03.041

Montenbruck, O., Steigenberger, P., & Hauschild, A. (2018b). Multi-GNSS signal-in-space range error assessment – Methodology and results. *Advances in Space Research*, *61*(12), 3020–3038. https://doi.org/10.1016/j.asr.2018.03.041

Montenbruck, O., Steigenberger, P., Prange, L., Deng, Z., Zhao, Q., Perosanz, F., Romero, I., Noll, C., Stürze, A., Weber, G., Schmid, R., MacLeod, K., & Schaer, S. (2017). The Multi-GNSS Experiment (MGEX) of the International GNSS Service (IGS) – Achievements, prospects and challenges. *Advances in Space Research*, *59*(7), 1671–1697. https://doi.org/10.1016/j.asr.2017.01.011

Naciri, N. (2023). *Global, instantaneous, centimetre, satellite-based positioning with Precise Point Positioning* [PhD Thesis]. York University.

Naciri, N., & Bisnath, S. (2020, October 15). Multi-GNSS Ambiguity Resolution For Signal Obstruction in PPP. *Inside GNSS*. https://insidegnss.com/multi-gnss-ambiguity-resolution-for-signal-obstruction-in-ppp/

Naciri, N., & Bisnath, S. (2021). An uncombined triple-frequency user implementation of the decoupled clock model for PPP-AR. *Journal of Geodesy*, *95*(5), 1–17. https://doi.org/10.1007/s00190-021-01510-y

Odijk, D., Zhang, B., & Khodabandeh, A. (2016). *Multi-GNSS PPP-RTK: From large- to small-scale networks*. Proceedings of the 29th International Technical Meeting of the Satellite Division of the Institute of Navigation (ION GNSS+).

Park, K.-D., Yoon, W.-J., & Lee, J.-S. (2024). Reduction of Multipath Effect in GNSS Positioning by Applying Pseudorange Acceleration as Weight. *Sensors*, *24*(21), 6880. https://doi.org/10.3390/s24216880

Parkinson, B. W., & Spilker, J. J. (1996). *The global positioning system: Theory and applications: Vol. vol.1*. American Institute of Aeronautics and Astronautics.

Pengfei, C., Wei, L., Jinzhong, B., Hanjiang, W., Yanhui, C., & Hua, W. (2011). Performance of Precise Point Positioning (PPP) Based on Uncombined Dual-Frequency GPS Observables. *Survey Review*, *43*(322), 343–350. https://doi.org/10.1179/003962611X13055561708588

Petit, G., & Luzum, B. (2010). IERS conventions (2010). *Tech. Rep. DTIC Document*, *36*, 180.

Qu, L., Jiang, W., Li, J., Du, Y., Wang, H., Wang, L., & Wang, J. (2024). Mitigation of multipath effects in multi-GNSS and multi-frequency precise point positioning with multipath hemispherical maps. *GPS Solutions*, *28*(3), 104. https://doi.org/10.1007/s10291-024-01647-1

Qu, L., Wang, L., Acharya, T. D., Du, Y., Wang, H., & Jiang, W. (2023). Global single-epoch narrow-lane ambiguity resolution with multi-constellation and multi-frequency precise point positioning. *GPS Solutions*, *27*(1), 29. https://doi.org/10.1007/s10291-022-01368-3

Revnivykh, S., Bolkunov, A., Serdyukov, A., & Montenbruck, O. (2017). GLONASS. In *Springer Handbook of Global Navigation Satellite Systems* (pp. 219–245). Springer.

Rizos, C. (2002). Network RTK Research and Implementation: A Geodetic Perspective. *Journal of Global Positioning Systems*, *1*(2), 144–150. https://doi.org/10.5081/jgps.1.2.144

Rizos, C., Janssen, V., Roberts, C., & Grinter, T. (2012). *Precise Point Positioning: Is the era of differential GNSS positioning drawing to an end?* Proceedings of FIG Working Week 2012, Rome, Italy. http://www.fig.net/pub/fig2012/techprog.htm

Saastamoinen, J. (1973). Contributions to the theory of atmospheric refraction. *Bulletin Géodésique*, *107*(1), 13–34.

Sardón, E., Rius, A., & Zarraoa, N. (1994). Estimation of the transmitter and receiver differential biases and the ionospheric total electron content from Global Positioning System observations. *Radio Science*, *29*(3), 577–586. https://doi.org/10.1029/94RS00449

Scherneck, H. G. (1991). A parametrized solid earth tide model and ocean tide loading effects for global geodetic baseline measurements. *Geophysical Journal International*, *106*(3), 677–694.

Schmid, R., Dach, R., Collilieux, X., Jäggi, A., Schmitz, M., & Dilssner, F. (2016a). Absolute IGS antenna phase center model igs08.atx: Status and potential improvements. *Journal of Geodesy*, *90*(4), 343–364. https://doi.org/10.1007/s00190-015-0876-3

Schmid, R., Dach, R., Collilieux, X., Jäggi, A., Schmitz, M., & Dilssner, F. (2016b). Absolute IGS antenna phase center model igs08.atx: Status and potential improvements. *Journal of Geodesy*, *90*(4), 343–364. https://doi.org/10.1007/s00190-015-0876-3

Seeber, G. (2003). *Satellite Geodesy*. De Gruyter. https://doi.org/doi:10.1515/9783110200089

Seepersad, G. G. (2018). *Improving Reliability and Assessing Performance of Global Navigation Satellite System Precise Point Positioning Ambiguity Resolution*.

Shen, Y., Li, W., Xu, G., & Li, B. (2014). Spatiotemporal filtering of regional GNSS network's position time series with missing data using principle component analysis. *Journal of Geodesy*, *88*(1), 1–12. https://doi.org/10.1007/s00190-013-0663-y

Shi, J., & Gao, Y. (2010). Analysis of the integer property of ambiguity and characteristics of code and phase clocks in PPP using a decoupled clock model. *Proc. ION GNSS*, 2553–2564. http://www.researchgate.net/profile/Junbo_Shi/publication/271842983_Analysis_of_the_integer_property_of_ambiguity_and_characteristics_of_code_and_phase_clocks_in_PPP_using_a_decoupled_clock_model/links/54d41e690cf246475805746c.pdf

Shi, J., & Gao, Y. (2013). A comparison of three PPP integer ambiguity resolution methods. *GPS Solutions*, *18*(4), 519–528. https://doi.org/10.1007/s10291-013-0348-2

Teunissen, P. J. G. (1995). The least-squares ambiguity decorrelation adjustment: A method for fast GPS integer ambiguity estimation. *Journal of Geodesy*, *70*(1–2), 65–82. https://doi.org/10.1007/BF00863419

Teunissen, P. J. G., & Khodabandeh, A. (2015). Review and principles of PPP-RTK methods. *Journal of Geodesy*, *89*(3), 217–240. https://doi.org/10.1007/s00190-014-0771-3

Teunissen, P. J. G., & Montenbruck, O. (Eds.). (2017). *Springer Handbook of Global Navigation Satellite Systems*. Springer International Publishing. https://doi.org/10.1007/978-3-319-42928-1

Townsend, B., Lachapelle, G., Fortes, L. P., Melgård, T. E., Nørbech, T., & Raquet, J. (1999). *New Concepts for a Carrier Phase Based GPS Positioning Using a National Reference Station Network*. 319–326. http://www.ion.org/publications/abstract.cfm?jp=p&articleID=681

van Bree, R. J. P., & Tiberius, C. C. J. M. (2012). Real-time single-frequency precise point positioning: Accuracy assessment. *GPS Solutions*, *16*(2), 259–266.

Van Diggelen, F. (2009). *A-GPS: Assisted GPS, GNSS, and SBAS*. Artech House.

Wabbena, G., Schmitz, M., & Bagge, A. (2005). *PPP-RTK: Precise Point Positioning Using State-Space Representation in RTK Networks*.

Wang, J., Huang, G., Yang, Y., Zhang, Q., Gao, Y., & Zhou, P. (2020). Mitigation of Short-Term Temporal Variations of Receiver Code Bias to Achieve Increased Success Rate of Ambiguity Resolution in PPP. *Remote Sensing*, *12*(5), 796. https://doi.org/10.3390/rs12050796

Wanninger, L., & Wallstab-Freitag, S. (2007). Combined Processing of GPS, GLONASS, and SBAS Code Phase and Carrier Phase Measurements. *ION GNSS 20th International Technical Meeting of Satellite Division*, 866–875.

Wu, J., Wu, S., Hajj, G., Bertiger, W., & Lichten, S. (1992). Effects of antenna orientation on GPS carrier phase. *Astrodynamics 1991*, *1*, 1647–1660.

Xiao, G., Li, P., Gao, Y., & Heck, B. (2019). A Unified Model for Multi-Frequency PPP Ambiguity Resolution and Test Results with Galileo and BeiDou Triple-Frequency Observations. *Remote Sensing*, *11*(2), 116. https://doi.org/10.3390/rs11020116

Xu, B., Zhang, S., Kuang, K., & Li, X. (2023). A unified cycle-slip, multipath estimation, detection and mitigation method for VIO-aided PPP in urban environments. *GPS Solutions*, *27*(2), 59. https://doi.org/10.1007/s10291-023-01396-7

Yang, L., Pan, G., Zuo, X., Zhang, J., & Yu, Z. (2024). BDS-3/GNSS Multi-frequency PPP Rapid Ambiguity Resolution. In C. Yang & J. Xie (Eds.), *China Satellite Navigation Conference (CSNC 2024) Proceedings* (pp. 59–72). Springer Nature Singapore.

Zaminpardaz, S., & Teunissen, P. J. G. (2017). Analysis of Galileo IOV + FOC signals and E5 RTK performance. *GPS Solutions*, *21*(4), 1855–1870. https://doi.org/10.1007/s10291-017-0659-9

Zhang, W., & Lachapelle, G. (2001). Precise point positioning using GPS/GLONASS/Galileo with intersystem biases. *Journal of Geodesy*, *75*(10), 653–660.

Zhao, L., Sun, Z., Yang, F., Liu, X., & Zhang, J. (2023). Improved Multi-GNSS PPP Partial Ambiguity Resolution Method Based on Two-Step Sorting Criterion. *Remote Sensing*, *15*(13), 3319. https://doi.org/10.3390/rs15133319

Zhu, C., Zhang, J., & Li, S. (2019). Advancements in Multi-Constellation GNSS for Enhanced PPP Performance. *Advances in Space Research*, *63*(12), 3672–3683.

Zhu, D., Zhong, Z., Zhang, M., Wu, S., Zhang, K., Li, Z., Hu, Q., Liu, X., & Liu, J. (2023). An Improved Principal Component Analysis Method for the Interpolation of Missing Data in GNSS-Derived PWV Time Series. *Remote Sensing*, *15*(21), 5153. https://doi.org/10.3390/rs15215153

Zumberge, J. F., Heflin, M. B., Jefferson, D. C., Watkins, M. M., & Webb, F. H. (1997). Precise point positioning for the efficient and robust analysis of GPS data from large networks. *Journal of Geophysical Research: Solid Earth (1978–2012)*, *102*(B3), 5005–5017. https://doi.org/10.1029/96JB03860